

Structural framework of the unstable mountain slope by Stampa, Aurland, Western Norway



Tonje Karin Rio

Master Thesis in Climate Change Management

Department of Environmental Sciences, Faculty of Engineering and Science

WESTERN NORWAY UNIVERSITY OF APPLIED SCIENCES

Sogndal
June, 2019

I confirm that the work is self-prepared and that references/source references to all sources used in the work are provided, cf. Regulation relating to academic studies and examinations at the Western Norway University of Applied Sciences (HVL), § 10.



Western Norway
University of
Applied Sciences

Structural framework of the unstable mountain slope by Stampa, Aurland, Western Norway

Master thesis in Climate Change Management

Author: Tonje Karin Rio	Author sign. <i>Tonje K. Rio</i>
Thesis submitted: Spring 2019	Open thesis
Main Supervisor: Thomas Scheiber Co-supervisors: Deta Gasser, Helge Henriksen	
Keywords: Geohazards Climate change Rock slope instabilities Structural mapping ArcGIS Kinematic indicators Failure mechanisms Deep-seated gravitational slope deformations Rockslides Rock falls Rock topples	Number of pages: 66 + Appendix: 7 Sogndal, 02.06.2019
This thesis is a part of the master's program in Climate Change Management (Planlegging for klimaendringer) at the Department of Environmental Sciences, Faculty of Engineering and Science at the Western Norway University of Applied Sciences. The author(s) is responsible for the methods used, the results that are presented and the conclusions in the thesis.	

Preface

This study was conducted in completion with a master's degree in Climate Change Management at the Western Norway University of Applied Sciences, and was sponsored by the Geological Survey of Norway (NGU). Fieldwork was carried out in Aurland the summer of 2018, and the thesis was written throughout the following spring semester of 2019. Photographs and figures are produced by the author, unless stated otherwise.

Firstly, I would like to thank all teachers and fellow students at the Department of Environmental Sciences for making these two years educational and fun. A special thanks goes to my supervisors Thomas Scheiber, Deta Gasser and Helge Henriksen for valuable help during fieldwork, data analyses and the following writing process. Even with a busy schedule, you have always been happy to set aside time for a good discussion. A big THANK YOU for providing great guidance and investing a lot of time and effort into my work!

Further on, I would like to thank Sigurd Vikesland for letting me stay at your beautiful, little summer farm at Joasete, Aurland when I was doing my fieldwork. I would also like to thank Benita Putlitz at the isotope laboratory at the University of Lausanne for conducting the $\delta^{18}\text{O}$ analyses.

Lastly, I would like to thank my friends and family for great support and encouragement, you are the best! A special thanks goes to my dad who kept me company during fieldwork, and my flatmates for coping with my "rollercoaster-mood" the last couple of months.

Sogndal, 1st of June 2019

Tonje Karin Rio

Abstract

Downscaled climate projections point towards a warmer and wetter climate in Norway, which is likely to trigger increased rockslide activity. With many rock slope instabilities and a large record of historical rockslides, Sogn og Fjordane County is especially vulnerable to climate change. The unstable mountain slope by Stampa above Aurlandsfjorden is a structurally complex rock slope instability, which is located predominantly within phyllitic rocks of the Fortun-Vang nappe complex. The aim of this study is (1) to better understand the Caledonian and post-Caledonian deformation history of the area, and (2) to investigate ductile, semi-brittle and brittle structures that may affect the stability of the mountain slope. Fieldwork and associated kinematic, structural and $\delta^{18}\text{O}$ analyses were conducted. Results indicate that most ductile and semi-brittle structures can be related to top-to-the-NW extensional deformation of the Caledonian collapse. However, some structures can be related to top-to-the-SE contractional deformation of the Caledonian nappe-emplacment. $\delta^{18}\text{O}$ analyses indicate that various generations of quartz veins were precipitated by locally derived fluids in a lithostatic regime. The abundance and orientation of pre-existing structures seem to have a large control on the overall stability of the mountain slope. Several lithological and structural features are believed to promote rock slope failures at Stampa: (1) Fjord-dipping ductile and semi-brittle structures, (2) folds and interference folds, (3) regional brittle faults and joint sets and (4) lithological discontinuities within the Fortun-Vang nappe complex. The unstable part of the mountain slope can be classified as a cataclinal slope with three active deformation mechanisms. Toppling of unstable blocks occurs on underdip slopes at the edge of the frontal cliff, whereas planar sliding along the foliation occurs on overdip slopes at the toe of the mountain slope. Rotational sliding generally dominates deep-seated gravitational slope deformations (DGSDs) across the full extent of the unstable area(s). Structural mapping of rock slope instabilities and characterisation of active deformation mechanisms may lead to the installation of early warning systems at susceptible sites and thereby decrease the risk of damage on human lives, properties and infrastructure.

Sammendrag på norsk

Nedskalerte klimaprojeksjoner viser at klimaet i Norge vil bli varmere og våtere, noe som sannsynligvis vil føre til økt (fjell)skred-aktivitet. Med mange ustabile fjellsider samt historiske skredhendelser er Sogn og Fjordane spesielt sårbar for klimaendringer. Den ustabile fjellsiden ved Stampa over Aurlandsfjorden er en strukturell kompleks fjellside, som hovedsakelig består av fyllittiske bergarter tilhørende Fortun-Vang dekkekomplekset. Målet med dette studiet er (1) å bedre forstå den Kaledonske og post-Kaledonske deformasjonshistorien i området, og (2) å undersøke duktile, semi-sprø og sprø strukturer som kan påvirke stabiliteten av fjellsiden. Feltarbeid og tilknyttede kinematiske, strukturelle og $\delta^{18}\text{O}$ analyser ble utført. Resultater fra disse analysene indikerer at de fleste duktile og semi-sprø strukturene kan relateres til topp-mot-NV ekstensjonell deformasjon under kollaps av den Kaledonske fjellkjeden. Noen strukturer kan imidlertid relateres til topp-mot-SØ kontraksjonell deformasjon under innskyvning av de Kaledonske skyvedekkene. $\delta^{18}\text{O}$ analyser tyder på at forskjellige generasjoner av kvartsårer ble utfelt av lokale fluider i et litostatisk regime. Utbredelse og orientering av pre-eksisterende geologiske strukturer ser ut til å ha en stor kontroll over den overordnede stabiliteten av fjellsiden. Flere litologiske og strukturelle egenskaper antas å fremme utglidning av bergmasser ved Stampa: (1) Fjord-hellende duktile og semi-sprø strukturer, (2) folder og kryssende foldegenerasjoner, (3) regionale sprø forkastninger og sprekkesett samt (4) litologiske diskontinuiteter innenfor Fortun-Vang dekkekomplekset. Den ustabile delen av fjellsiden kan bli klassifisert som en fjord-hellende *cataclinal* skråning med tre aktive deformasjonsmekanismer. Utveltning av ustabile blokker forekommer på underhellende *underdip* skråninger på kanten av den frontale klippen, mens planar utglidning langs foliasjonen er mer sannsynlig på overhellende *overdip* skråninger ved foten av fjellsiden. En rotasjonsmekanisme vil generelt dominere deformasjonen og bevegelsen av dyptliggende bergmasser langs hele den ustabile fjellsiden. Strukturell kartlegging av ustabile fjellsider og karakterisering av aktive deformasjonsmekanismer kan føre til installasjon av varslingsystem på utsatte lokaliteter, og dermed redusere risikoen for skade på menneskeliv, eiendommer og infrastruktur.

Table of contents

Preface	I
Abstract	III
Sammendrag på norsk	V
Table of contents.....	VII
1 Introduction	9
2 Background	10
2.1 Regional geological setting	10
2.1.1 The Scandinavian Caledonides	10
2.1.2 The Hardangerfjord Shear Zone	12
2.2 Geological setting of the study area	14
2.2.1 Bedrock geology	14
2.2.2 Quaternary geology and post-glacial gravitational deformation.....	16
2.2.3 Active gravitational deformation and rock slope monitoring.....	17
2.3 Rock slope failures	20
2.3.1 Classification	20
2.3.2 Destabilising factors.....	21
2.4 Climate change	23
2.4.1 Downscaled projections for Sogn og Fjordane	23
2.4.2 Increased rockslide activity?	23
3 Methods	25
3.1 Fieldwork	25
3.1.1 Equipment	26
3.2 Software	26
3.2.1 ArcGIS 10.2	26
3.2.2 Stereonet 10	26
3.2.3 Inkscape	26
3.3 Petrographic and kinematic analyses of thin sections.....	26
3.4 Oxygen stable isotope ($\delta^{18}\text{O}$) analyses	27
4 Results	27
4.1 Fieldwork	27

4.1.1	General lithological and structural descriptions of mapped units.....	28
4.1.2	Detailed structural and kinematic analyses of field data.....	32
4.1.3	Geological profiles	42
4.2	Petrographic and kinematic analyses of thin sections.....	44
4.3	Oxygen stable isotope ($\delta^{18}\text{O}$) analyses	50
5	Discussion	53
5.1	Structural evolution and relation to the Caledonian orogeny.....	53
5.2	Implications for rock slope stability.....	55
5.3	Uncertainty in structural geology and geological modelling	61
6	Conclusion	63
7	References	64
8	Appendix.....	67

1 Introduction

Climate change represents one of the major environmental challenges of our times, and is considered one of the top priorities on the global policy agenda. Downscaled climate projections point towards a warmer and wetter climate in Norway, which is likely to trigger increased rockslide activity (Norsk klimaservicesenter, 2016). With many rock slope instabilities and a large record of historical rockslides (Saintot et al., 2011), Sogn og Fjordane County is especially vulnerable to climate change. The unstable mountain slope by Stampa above Aurlandsfjorden is a structurally complex rock slope instability, which shows signs of active gravitational deformation over an area of approx. 11 km² (Böhme et al., 2013). The instability is located predominantly within phyllitic rocks of the Fortun-Vang nappe complex, which lies tectonically sandwiched between the Proterozoic basement and gneissic rocks of the Jotun nappe complex (Bryhni, 1977). Stampa is located between the villages of Flåm and Aurland, with the main east-west road (E16) connecting Oslo and Bergen running along the fjord. The village of Flåm is a popular tourist destination, receiving about 250 000 tourists in the summer months (Guddal & Løset, 2017). In addition, the village houses about 400 permanent residents. Unstable blocks at the frontal cliff by Joasetbergi have been continuously monitored since 2016, with an average movement of 10 mm/year (Kristensen & Bergeng, 2018). Future rockslides may have large societal consequences, especially if rock masses reach the fjord and create a tsunami (Domaas & Glimsdal, 2009). Böhme et al. (2013) suggests a strong structural control on the overall stability of the mountain slope. However, the regional structural geological framework in terms of past and present deformation mechanisms needs further investigation, and is the focus of this master project. The aim is to investigate ductile, semi-brittle and brittle structures that possibly control the size and extent of future rockslides, and to answer following research questions:

- (1) What sense of movement is shown by the different ductile and semi-brittle structures, and how do they fit into the Caledonian and post-Caledonian deformation history of the area?
- (2) What is the ductile, semi-brittle and brittle structural style within the phyllitic rocks, and what role could it play for the location of future sliding planes?

In addition to these two research questions, a $\delta^{18}\text{O}$ pilot study on various generations of quartz veins within the Fortun-Vang nappe complex is presented. These analyses contribute to further understanding of the deformation history of the Stampa-area, and help identify paleo-fluid-circulation patterns and fluid sources within the phyllitic rocks.

2 Background

2.1 Regional geological setting

2.1.1 The Scandinavian Caledonides

The onshore bedrock geology of Norway can be divided into three main units: (1) Proterozoic basement, (2) Caledonian nappes and (3) post-Caledonian sedimentary and igneous rocks of the Devonian basins and the Permian Oslo rift (Ramberg et al., 2008). The bedrock is variably deformed by the Caledonian orogeny, and remnants of the ancient orogen can be found across most parts of Norway (Fig. 2.1).

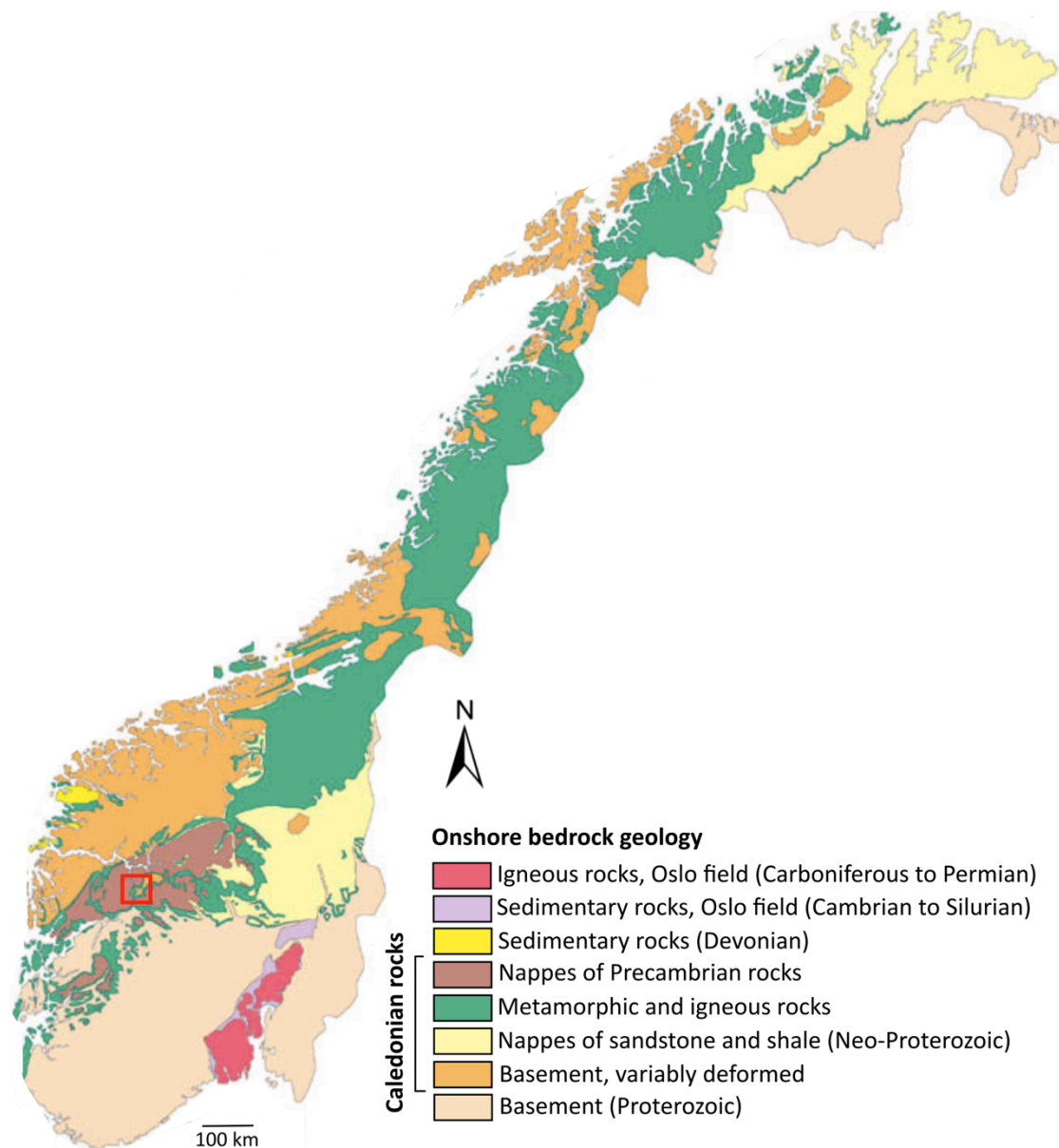


Fig. 2.1 – Onshore bedrock geology map of Norway. Modified after Ramberg et al. (2008). Study area is indicated by a red rectangle.

The Scandinavian Caledonides are the result of tectonic plate movements leading to the opening and subsequent closing of the Iapetus Ocean in the late Neoproterozoic and early Palaeozoic (Torsvik et al., 1996). The supercontinent Rodinia started rifting at about 700 Ma, forming the two continents Laurentia (today's North America and Greenland) and Baltica (today's Scandinavia) separated by the Iapetus Ocean (Gee et al., 2008). Accretion of the Scandinavian Caledonides happened through several stages related to the closing of the Iapetus Ocean and subduction of the Baltoscandian margin beneath the Laurentian plate, before the main collisional event during the Ordovician and Silurian (Fig. 2.2). Complete merge of the two continents happened in the Early Devonian, followed by post-Caledonian extensional deformation related to the collapse of the, by then, over-thickened orogenic wedge (Roberts, 2003).

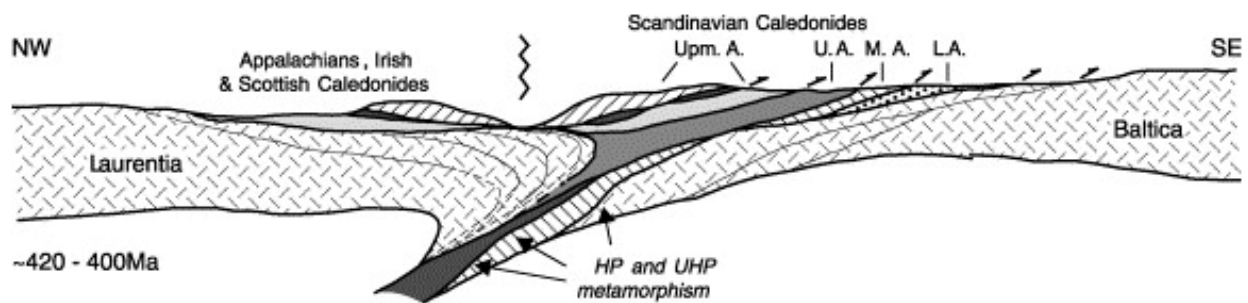


Fig. 2.2 – Section across the central part of the Caledonian orogen showing the main collisional event in Middle Silurian to Early Devonian time (420-400 Ma), referred to as the Scandian phase. L.A., M.A., U.A. and Upm. A. represent the Lower-, Middle-, Upper- and Uppermost Allochthon respectively (Roberts, 2003).

The Scandinavian Caledonides are exposed in Norway and Sweden, stretching 1500 km from the Barents Sea in the north to Rogaland in the south (Gee, 1975). The orogen is characterised by a low-angle fold-and-thrust belt dipping towards the NW. The Caledonian nappes were stacked and thrust SE-ward upon the Proterozoic basement, forming the Lower-, Middle-, Upper- and Uppermost Allochthon (Fig. 2.2).

The Lower and Middle Allochthon are mainly dominated by original metasedimentary and igneous rocks of the Baltoscandian margin (Gee, 1975). Grade of metamorphism is increasing upwards and throughout the tectonostratigraphy – from greenschist facies to amphibolite, granulite and eclogite facies at the base of the Upper Allochthon. The Upper Allochthon consists of Iapetus-derived terranes including island-arc assemblages and ophiolites, with associated sedimentary successions (Roberts, 2003). The Uppermost Allochthon represents the most exotic terranes of the Scandinavian Caledonides, and is characterised by granitic batholiths and sedimentary rocks of the Laurentian margin (Gee et al., 2008).

2.1.2 The Hardangerfjord Shear Zone

The structural framework of the southwestern Scandinavian Caledonides is characterised by the low-angle Hardangerfjord Shear Zone, which is generally dipping towards the NW (Fossen & Hurich, 2005). This 600 km long ductile shear zone can be traced from the coastal areas south of Bergen to the eastern part of Jotunheimen (Fig. 2.3), with a maximum NW-side-down displacement of 10 to 15 km. The Hardangerfjord Shear Zone can also be traced offshore, and is believed to have had significant implications for the structural evolution of the North Sea rift system (Fossen & Hurich, 2005).

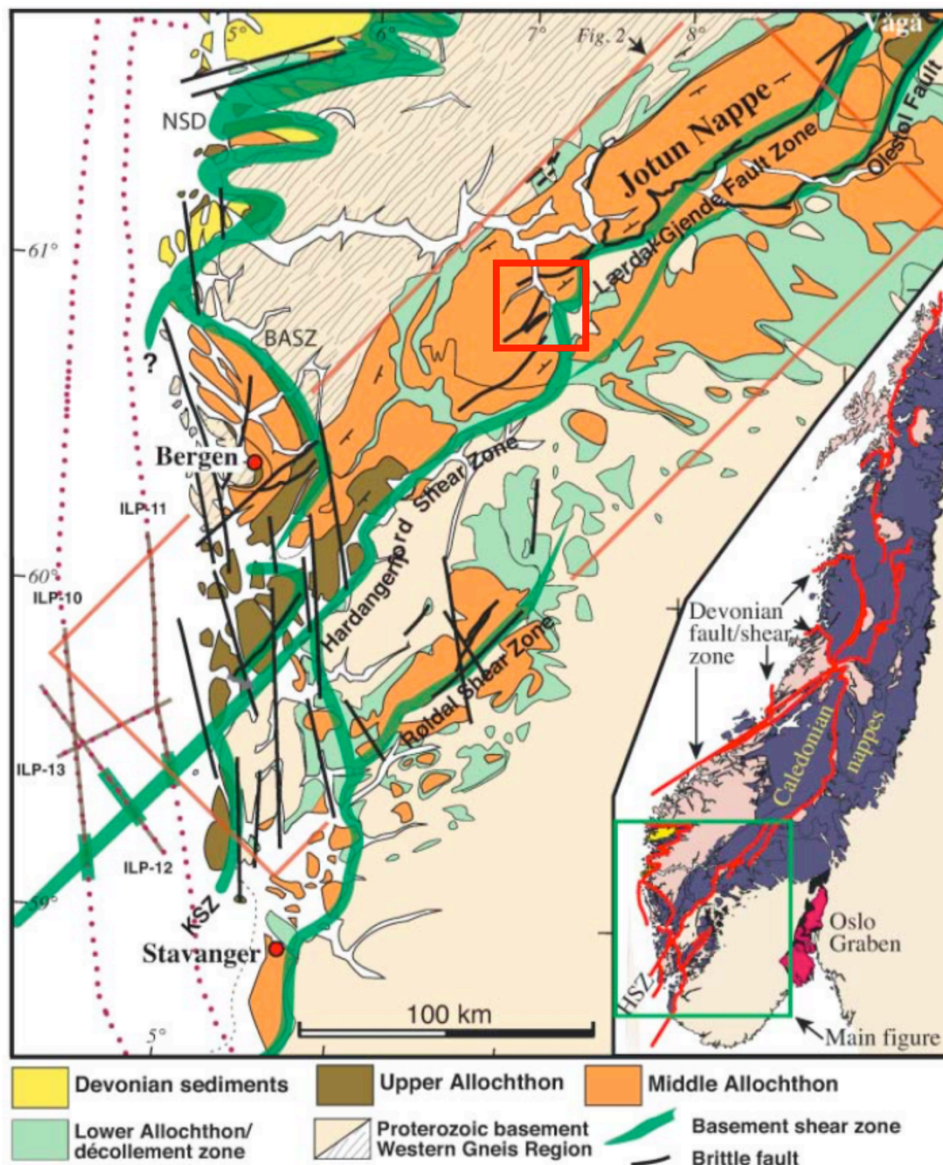


Fig. 2.3 - Tectonic map of Western Norway showing the Hardangerfjord Shear Zone (HSZ) and associated macro-scale structures in the region (Fossen & Hurich, 2005). Note the distinction between the relatively undeformed basement SE of the HSZ, and the highly deformed Western Gneiss Region NW of the HSZ. Study area is indicated by a red rectangle.

Several studies suggest that Caledonian contractional deformation at some point was replaced by extensional deformation (Fig. 2.4). According to Fossen and Dunlap (1998) this happened ca. 408-402 Ma, and can be explained by a shift from convergent to divergent plate movement connected to early orogenic collapse and backsliding of the orogenic wedge. This shift involved a reversal of shear sense in the décollement zone, and the development of NW-verging folds and top-to-the-NW mylonitic fabrics.

Continued footwall exhumation to the brittle regime formed the Lærdal-Gjende fault system (Fig. 2.4), which is regarded the brittle counterpart to the deep crustal, ductile Hardangerfjord Shear Zone. The Lærdal-Gjende fault system was reactivated during Permo-Triassic and late Jurassic extensional events, and is characterised by the abundance of splay faults (Andersen et al., 1999).

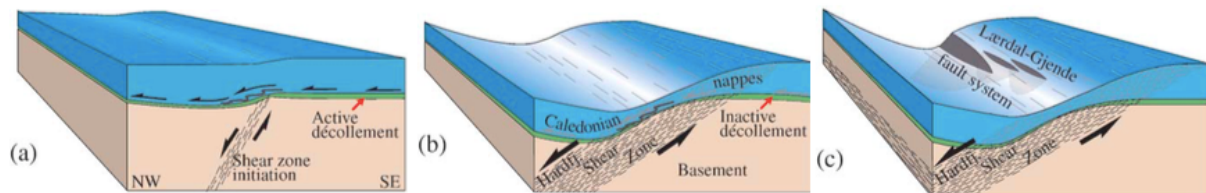


Fig. 2.4 – Evolution of the Hardangerfjord Shear Zone and the Lærdal-Gjende fault system (Fossen & Hurich, 2005).

Limited exposure of the basement makes it difficult to interpret and interpolate the geometry of the Hardangerfjord Shear Zone at depth. Seismic data indicates a 5-10 km thick mylonite zone, but the magnitude of this zone does not match the observed displacement of the shear zone (Milnes et al., 1997). In order to form a mylonite zone of such magnitude, total displacement should have been considerable larger than 10 to 15 km. An explanation for this incoherency may be that (1) the Hardangerfjord Shear Zone was formed on a pre-existing Proterozoic mylonite zone or (2) Caledonian contractional thrusting contributed the formation of the mylonite zone (Fossen et al., 2014).

2.2 Geological setting of the study area

2.2.1 Bedrock geology

The unstable mountain slope by Stampa is mainly composed of Cambro-Silurian phyllite belonging to the Fortun-Vang nappe complex. The phyllite is described as a basal thrust or décollement zone that lies tectonically sandwiched between migmatitic gneiss of the Proterozoic basement and mangeritic gneiss of the Jotun nappe complex (Fig. 2.5; Bryhni, 1977; Fossen & Hurich, 2005). Thus, two major Caledonian ductile thrust faults separate these three units (Fig. 2.5). Fossen and Hurich (2005) describe three main deformation stages in the area connected to the Caledonian orogeny: (1) Ductile top-to-the-SE contractional deformation of the Caledonian nappe emplacement, (2) ductile to semi-brittle top-to-the-NW extensional deformation of the Caledonian collapse and (3) post-Caledonian brittle deformation concentrated along N-S striking faults.

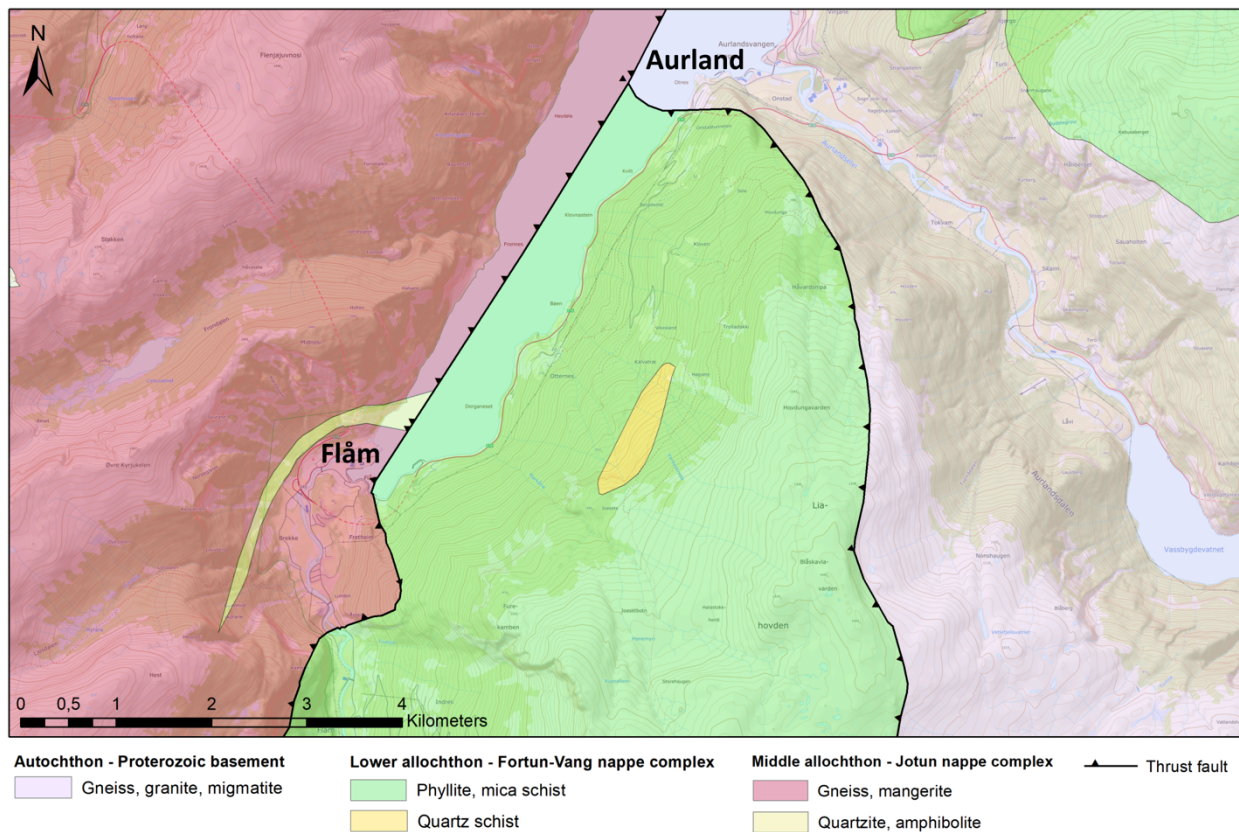


Fig. 2.5 – Bedrock geology map of the inner Aurlandsfjord. Modified after 1:50 000 map sheet, Aurland by Bryhni (1977). Note the three main geological units separated by two highlighted thrust faults. This map does not include new findings from this study. For own observations see the results-chapter (Ch. 4.1; Fig. 4.1).

The Proterozoic basement

The basement is mainly autochthonous, and is dominated by crystalline rocks of Proterozoic age (Gee et al., 2008). The basement SE of the Hardangerfjord Shear Zone is generally unaffected by Caledonian deformation (Fig. 2.3). The basement NW of the Hardangerfjord Shear Zone is commonly referred to as the Western Gneiss Region (Fig. 2.3), which is characterised by granitic and migmatitic gneiss variably overprinted by Caledonian deformation (Fossen & Hurich, 2005). Deformation intensity generally increases towards the NW and towards the overlying Caledonian nappes.

The Hardangerfjord Shear Zone is traced directly through the inner Aurlandsfjord (Fig. 2.3; Fossen & Hurich, 2005), which suggests a highly deformed basement within the study area. This notion has to be confirmed by field observations and associated thin section analyses, as detailed descriptions of the local basement rocks by Stampa are limited in existing literature.

The Fortun-Vang nappe complex

The Fortun-Vang nappe complex belongs to the Lower Allochthon and is composed of Cambro-Silurian metasedimentary rocks (Gee et al., 2008). The study area lies within a unit mainly consisting of phyllite and mica schist with two inliers of mylonitic rocks (Henriksen & Dale, 2018). These mylonitic inliers are not included in the published 1:50 000 bedrock geology map (Bryhni, 1977), but a lens of quartz schist is delineated close to Joasete (Fig. 2.5). The foliation has a variable orientation connected to several Caledonian deformation stages, but on average the foliation is dipping towards the WSW. The foliation is heavily folded, ranging from cm-scale closed folds to m-scale open folds (Böhme et al., 2013).

The Jotun nappe complex

The Jotun nappe complex belongs to the Middle Allochthon, and can be subdivided into a lower unit of mangeritic gneiss (the Flåm unit) and an upper unit of gabbroic to anorthostic rocks (the Stiganosi unit) (Bryhni et al., 1983). The study area is located within the Flåm unit, which is characterised by gneiss formed by high-grade metamorphism of original mangeritic rocks. Some regionally distributed layers of quartzite and amphibolite can be found within the unit. Blasto- and ultramylonites have been identified close to the basal thrust zone, with a foliation parallel to the underlying contact (Bryhni et al., 1983).

2.2.2 Quaternary geology and post-glacial gravitational deformation

The unstable mountain slope by Stampa is located on the eastern side of the inner Aurlandsfjord, which is a southerly branch of the Sognefjord in Western Norway. The topography of the area is heavily affected by Quaternary glaciations. Deep fjords and u-shaped valleys have been formed by glacial erosion until the local glacial retreat about 10 800 years BP (Mangerud et al., 2011). Being located at the 'inner bend' where the Flåmsdalen valley meets the Aurlandsfjord has made the Stampa-area especially exposed to stress during glaciation (Böhme et al., 2013). Sudden deglaciation left the steep walls prone to further gravitational deformation, as well as post-glacial tectonic activity including isostatic rebound and regional earthquakes (Blikra et al., 2006). Quaternary deposits in the area are dominated by block fields of weathered material and scree deposits, in addition to patches of exposed bedrock. Areas of fluvial and glaciofluvial deposits can be found in the valleys close to Flåm and Aurland (Fig. 2.6).

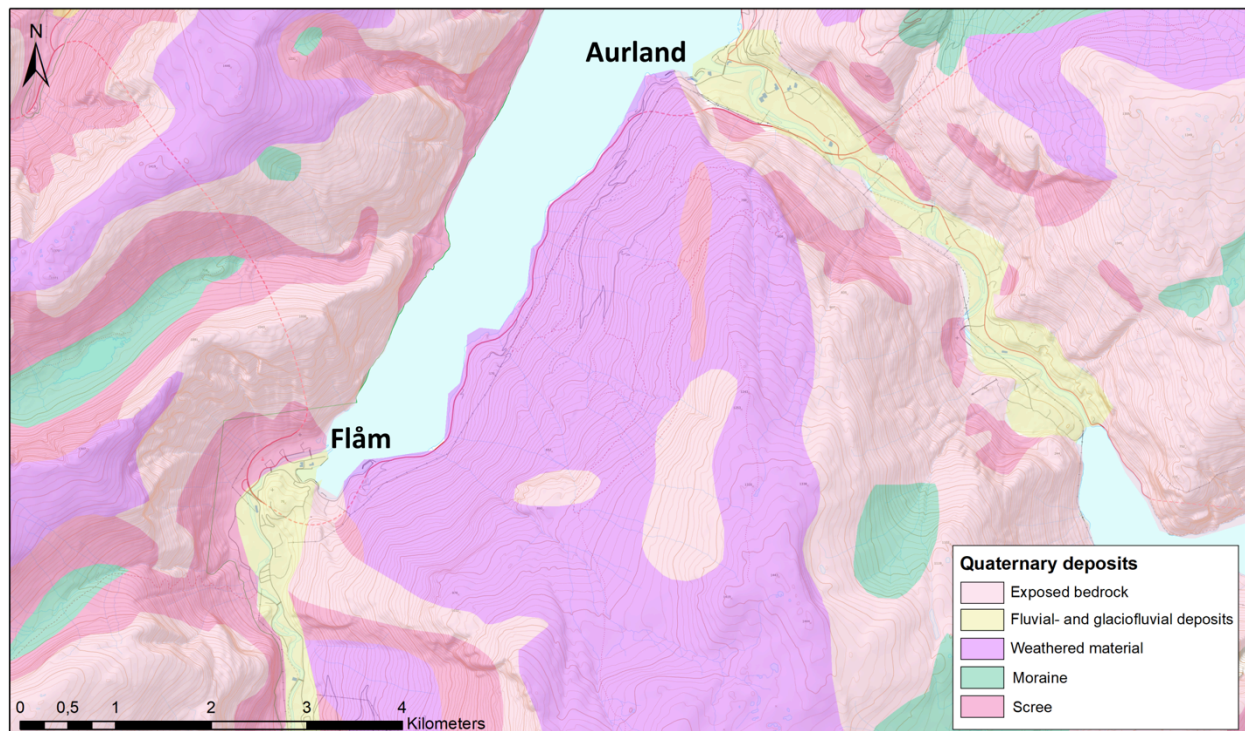


Fig. 2.6 – Quaternary geology map of the inner Aurlandsfjord. The eastern slope by Stampa is mainly dominated by weathered material, scree deposits and exposed bedrock. Modified after 1:50 000 quaternary map (NGU, 2019).

The area shows signs of post-glacial gravitational deformation, through surface exposure dating of two distinct lobes that cover the mountain slope (Böhme et al., 2013). The two lobes were dated to ca. 2400, 4300 and 12 000 years BP, which represent multiple post-glacial rockslide events. Additionally, seismic surveys and analyses of marine sediment cores indicate that at least two large rockslides have reached the fjord, dated to ca. 3000 and 11 000 years BP (Blikra et al., 2006).

2.2.3 Active gravitational deformation and rock slope monitoring

The mountain slope shows signs of active gravitational deformation over an area of approx. 11 km² (Fig. 2.7). There is a high activity of small rock falls, in addition to more deep-seated gravitational slope deformations (DGSDs). Blikra and Berg (2013) present eight potential failure-scenarios (Fig. 2.8a) with variable movement rates (Fig. 2.8b). Unstable blocks at the frontal cliff between Joasete and Furekamben make up the least stable part of the mountain slope, with an average movement rate of 10 mm/year (Scenario 3a – Joasetbergi). This area has been sporadically monitored since 2005, and continuously monitored since 2016 (Kristensen & Bergeng, 2018). Multiple surveillance systems have been installed in this area to measure real-time movement within the mountain slope. These systems include extensometers, total stations, terrestrial and satellite-based radar (InSAR).



Fig. 2.7 – Photograph showing the extent (white stippled line) of the area (11 km²) affected by active gravitational deformation. The frontal cliff between Joasete and Furekamben has the highest movement rates, with eight potential failure-scenarios (Fig. 2.8a). Modified after Böhme et al. (2013).

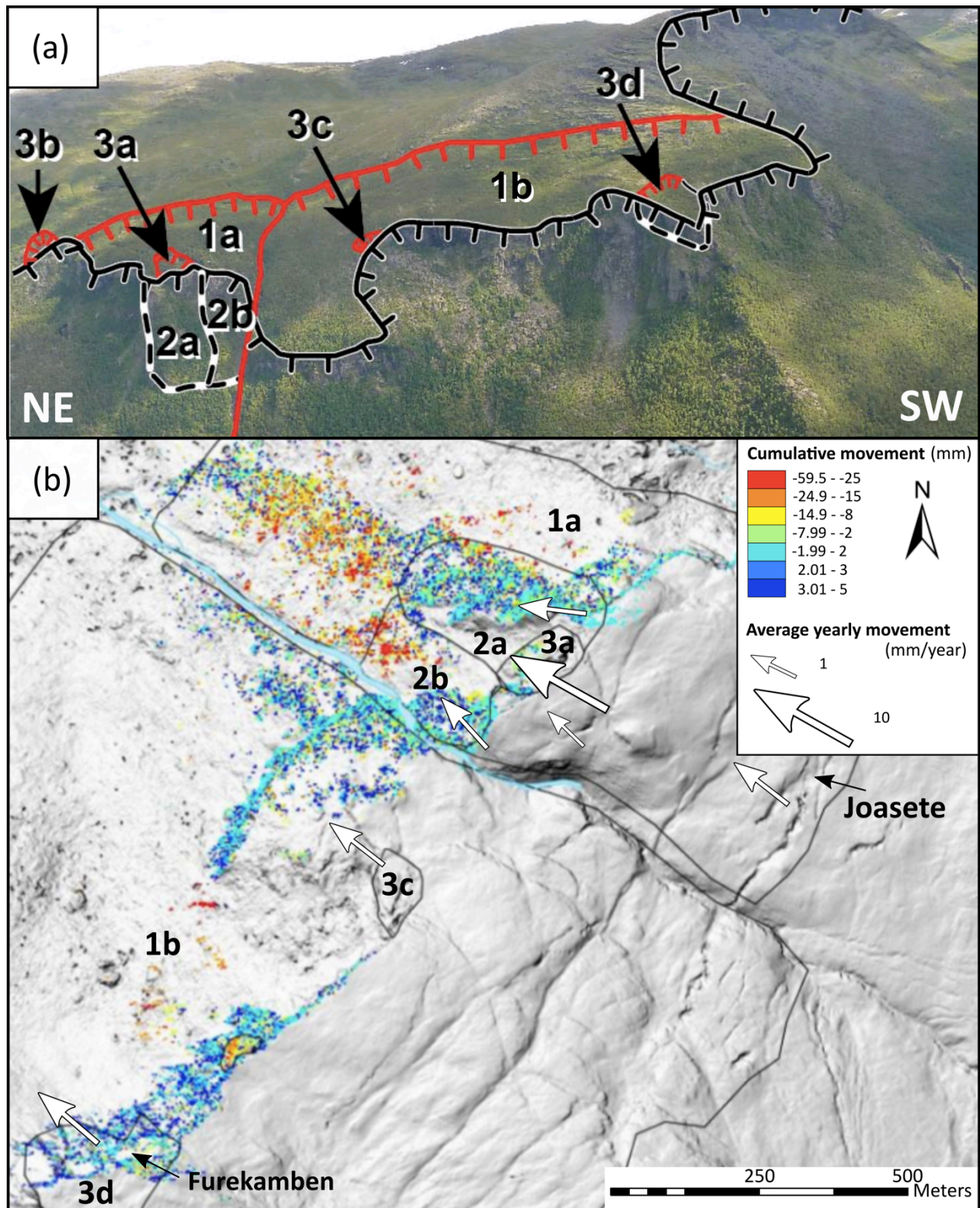


Fig. 2.8 – Photograph showing (a) eight potential failure-scenarios and (b) associated movement rates. Coloured dots represent cumulative movement (mm) during a period of terrestrial radar measurements from March to November 2015, while white arrows represent average yearly movement (mm/year) based on continuous GPS-measurements. Modified after Kristensen and Anda (2016) and Kristensen and Bergeng (2018).

Böhme et al. (2013) suggest three main failure mechanisms connected to large-scale deformation of the mountain slope: (1) Toppling, (2) subsiding bilinear wedge and (3) planar sliding along the foliation (Fig 2.9). Three vertical to sub-vertical joint sets have been observed in the area, striking (1) NNW-SSE, (2) WNW-ESE and (3) NNE-SSW. Most open gravitational structures have developed along these joint sets, and unstable area(s) seem to be delimited by these discontinuities. Surface depressions, graben structures and large open fractures striking NE-SW can be observed in the back-bounding area of the unstable mountain slope (Böhme et al. 2013). Discharging groundwater from the mountain slope has a high electrical conductivity, which indicates ongoing dissolution of minerals (Henriksen & Dale, 2018). As chemical weathering processes and high groundwater pressures will lower the shear strength along potential sliding planes, hydrological conditions may have large implications for the overall stability of the mountain slope (Blikra & Berg, 2013).

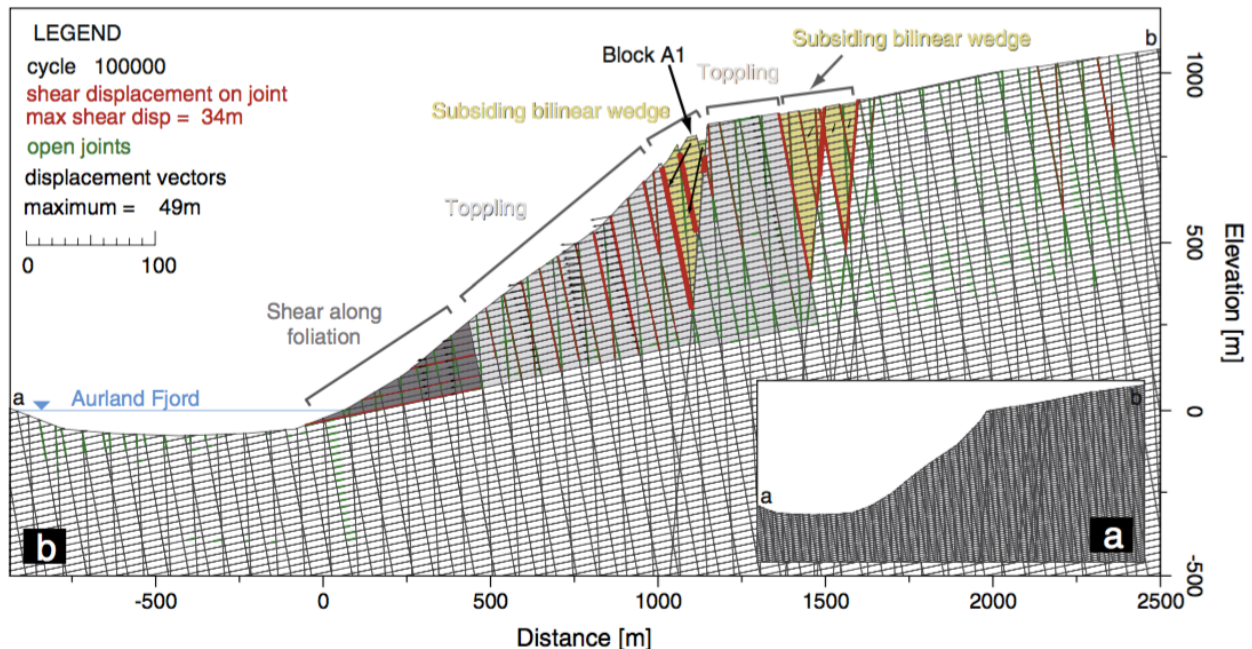


Fig. 2.9 – Model of the unstable mountain slope including topography, foliation, joint sets and failure mechanisms. Block A1 represents scenario 3a – Joasetbergi, which is classified as a high-risk scenario (Böhme et al., 2013).

NGI has estimated tsunami run-up height for three different scenarios as a secondary effect of potential large rockslides (Domaas & Glimsdal, 2009). These scenarios include rockslide volumes of approx. 40 million m³, 5 million m³ and 0,2 million m³. The latter represents block-failure (scenario 3a) at the frontal cliff between Joasete and Furekamben, and associated maximum tsunami run-up heights of less than 5 m. Rockslides of several million m³ cannot be ruled out and may involve run-up heights of up to 80 m.

2.3 Rock slope failures

2.3.1 Classification

Based on terminology from Cruden and Varnes (1996) rock slope failures can be divided into three main types: (1) Deep-seated gravitational slope deformations (DGSDs), which are slow to extremely slow flows or creep within the bedrock, (2) rockslides, which are rapid to extremely rapid translational or rotational failures of coherent rock masses and (3) rock falls or rock topples, which are rapid to extremely rapid failures of detached and free-falling blocks (Fig. 2.10).

Deep-seated gravitational slope deformations (DGSDs) are closely linked to the structural framework of a rock slope, and may evolve into sudden displacement of large rock volumes (Stead & Wolter, 2015). Rockslides and rock falls are both rapid slope failures, but differ according to the type of movement. While rockslides result from shear failures of coherent rock masses and initial movement along a planar or cylindrical surface, rock falls refer to free-falling blocks from vertical to sub vertical cliffs with little interaction between the moving units. Both types may evolve into a rock avalanche by taking on the character of a flow (Glade & Crozier, 2005). Rock slope failures of large volumes can trap huge amounts of air through internal interaction between the moving units. This process creates a high-density flow of great velocity, including up to several million cubic metres of rock masses ($> 10^5 \text{ m}^3$) (Cruden & Varnes, 1996).

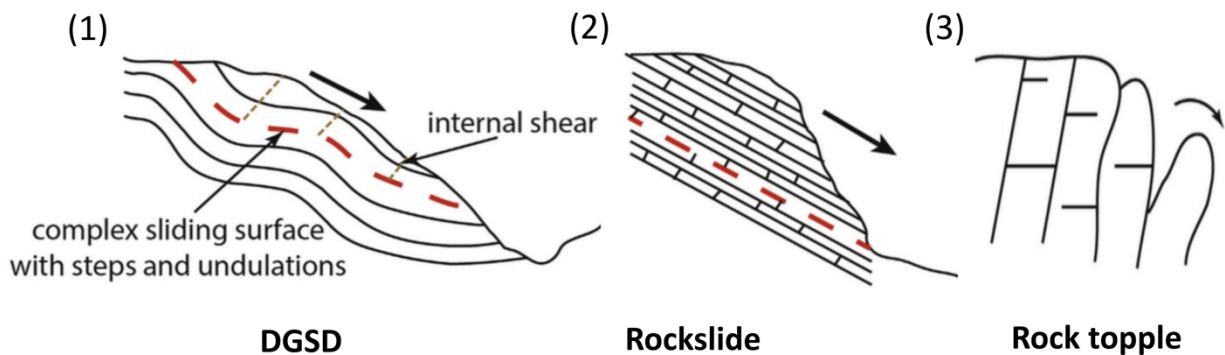


Fig. 2.10 – Schematic illustration showing the three main types of rock slope failures classified by Cruden and Varnes (1996): (1) Deep-seated gravitational slope deformations (DGSDs), (2) rockslides and (3) rock falls or rock topples. Modified after Stead and Wolter (2015).

2.3.2 Destabilising factors

Rock slope failures are a natural geological process in which gravity together with other destabilising factors lead to the downslope movement of slope-forming materials. A study by Glade and Crozier (2005) found it useful to subdivide factors that promote rock slope failures into three main groups: (1) Preconditioning factors, (2) preparatory factors and (3) triggering factors.

Preconditioning factors

Preconditioning factors are static and include rock properties such as lithology and structural framework (Stead & Wolter, 2015). These properties control the inherent rock strength and equilibrium slope angle. Preconditioning factors are believed to control the size and extent of rock slope failures (Saintot et al., 2011). Another crucial factor for slope stability is the inherent porosity and permeability of the rock, as high pore water pressures reduce friction along potential sliding planes (Glade & Crozier, 2005).

Preparatory factors

The stability of the slope may be weakened over time due to different preparatory factors, including weathering and slope-steepening processes such as fluvial and glacial erosion (Cruden & Varnes, 1996). Glacial debuttrressing or 'stress-release' acts as a preparatory factor through exfoliation and formation of non-tectonic joint sets (McColl, 2012). These joint sets directly weaken the rock, provide new pathways for water and increase the surface area exposed to various weathering processes. Debuttrressing can also act as a triggering factor if the slope stability has reached a critical point before removal of the glacial support (Glade & Crozier, 2005).

Triggering factors

Triggering factors are directly connected to the final initiation of failure, and often regarded the main 'cause' of rockslides. Such factors may include seismic activity or climatic triggers that initiate a sudden increase in pore water pressure (Cruden & Varnes, 1996). Rainfall events are a recognised triggering factor of rock slope failures, but relates mainly to small rockslides (McColl, 2012). Prolonged wet periods are more likely a trigger for deep-seated gravitational slope deformations (DGSDs). Snowmelt, freeze-thaw processes and degradation of permafrost promote joint expansion through increased pore water pressure or ice wedging (Glade & Crozier, 2005). These processes are mainly connected to subsequent small-scale failures, except for thawing of permafrost that can affect extensive and deep-seated areas. The susceptibility of a rock slope to hydrological triggers is determined by the flow regime within the rock. Rock slope failures are seldom a result of only one factor, but a result of stress-accumulation over time (Table 1).

Table 1 – Overview of factors that promote rock slope failures. Table modified after McColl (2012).

Factors	Preconditioning	Preparatory	Triggering
Lithology	X		
Structural framework	X		
Porosity and permeability	X		
Pre-existing stress factors	X		
Hydrostatic pressure		X	
Freeze-thaw processes		X	X
Weathering		X	
Erosion		X	
Glacial debuttressing		X	X
Exfoliation and sheet jointing		X	
Seismic activity			X
Climatic changes:			
High precipitation levels			X
Melting of snow and ice			X
Degradation of permafrost		X	X

2.4 Climate change

2.4.1 Downscaled projections for Sogn og Fjordane

The IPCC fifth assessment report (2014) point towards further warming of the atmosphere and associated changes in the global water cycle. For Sogn og Fjordane County, and Western Norway in general, this implies an increase in temperature and precipitation (Norsk klimaservicesenter, 2016). Downscaled projections estimate an increase in mean temperature of 4°C as well as an increase in precipitation of 15% towards the end of this century (Fig. 2.11). Together with an increase of average annual precipitation, extreme rainfall events are expected to increase by 15% in terms of intensity and frequency. These projections are based on continued high greenhouse gas emissions (RCP 8.5).

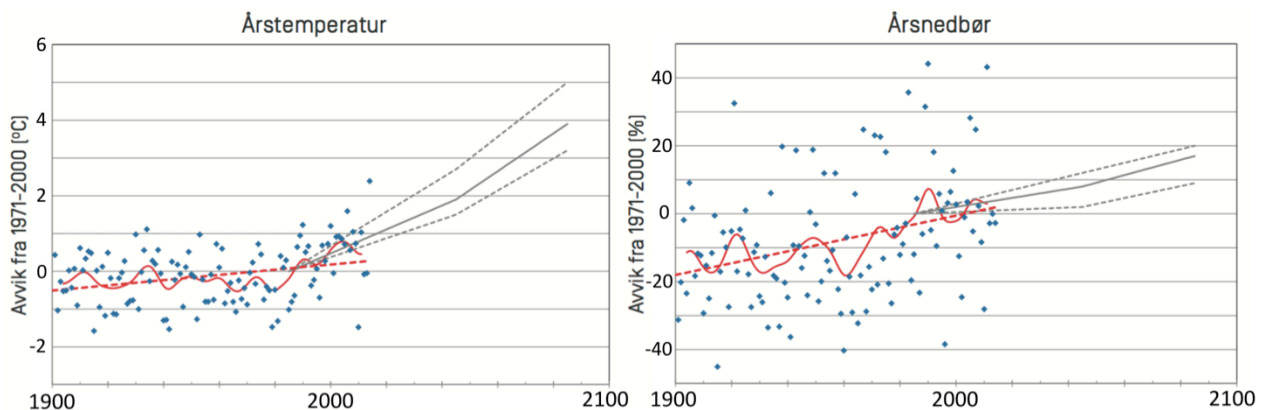


Fig. 2.11 – Historical and projected deviations from average annual values of temperature and precipitation (1971-2000) in Sogn og Fjordane County. Grey stippled lines illustrate uncertainties associated with these projections (Norsk klimaservicesenter, 2016).

2.4.2 Increased rockslide activity?

Glacial cycles, and associated climatic and non-climatic processes influence rock slope stability. A review by McColl (2012) summarises the spatial and temporal patterns of post-glacial failures, and assesses factors that promote such failures. Radiometric dating of large-scale rockslides throughout Europe, Asia, Canada and New Zealand reveals a general pattern of increased activity in clusters around 10-8 ka and 3-2 ka. These clusters are correlated to periods of enhanced seismic activity as a result of isostatic rebound combined with climatic changes. Other studies (Hermanns et al., 2017; Ivy-Ochs et al., 2009) connect rockslide activity to the mid-Holocene climate optimum, a period of significantly warmer and wetter climatic conditions (9-5 ka). Several other studies have correlated the occurrence of rockslides to climatic events or climatic transitions throughout the Holocene, which suggest an overall increase in rockslide activity following deglaciation (Borgatti & Soldati, 2010; Le Roux et al., 2009; Sanchez et al., 2010; Soldati et al., 2004).

Empirical evidence of increased rockslide activity as a response to deglaciation and connected climatic and non-climatic processes are clear. However, there is a lack of statistical evidence on significant factors affecting rock slope stability. As discussed earlier several factors promote rock slope failures from geological preconditioning factors that operate regardless of glacial processes, to further stress during glaciations and final triggering by seismic or climatic changes as a response to deglaciation (Glade & Crozier, 2005). It is also important to notice that slopes have a varying sensitivity to different triggering factors. A study conducted by Jaedicke et al. (2008) identified the most important triggering factors for different types of rock slope failures in Norway. Results show a wide spatial variation in significant triggering factors, which highlight the need for individual assessments of rock slopes.

Research into the relationship between ongoing climate change and rockslide activity over the past decades is still limited. There is no unambiguous evidence that rockslide activity has increased due to climate change over this period (Huggel et al., 2012). Switzerland has a relatively complete database of rockslide events, but no statistical significant relationship between meteorological triggers and slope failures is evident. However, a general increase in frequency of large slope failures ($> 10^5 \text{ m}^3$) can be observed in the Swiss Alps over the past decades (Fischer et al., 2010). The same trend applies to small to medium rock falls in the same area (Raveland & Deline, 2011).

It is widely recognised in high-altitude and high-latitude regions that climatic factors triggered large rock slope failures throughout the Holocene. Main climatic factors include increased pore water pressure due to extreme rainfall events or melt water drainage (Sanchez et al., 2010). Empirical evidence from studies on climate change and post-glacial failures suggest that ongoing climate change will have a similar effect (Stoffel & Huggel, 2012). Further work on finding statistical significant relationships between climatic triggers and rockslide activity is necessary, and may be used to confirm the common theoretical understanding of increased rockslide activity as a result of ongoing changes in temperature and precipitation.

3 Methods

3.1 Fieldwork

About three weeks of fieldwork were conducted in August 2018 and throughout the following autumn. The study area stretches from Aurlandsfjorden at sea level and up to 1400 m a.s.l. (Fig. 3.1). The lower part of the study area was easily accessible, while investigation of the upper part involved long hikes in mountainous terrain. Doing fieldwork at such elevations is dependent on good weather conditions, and must be planned according to season and meteorological forecasts. The weather during these three weeks varied from dry and sunny to wet and cloudy. Bad weather conditions made some constraints on navigability, and the quality of rock outcrop interpretations.

A total of 73 GPS points representing observations and structural measurements were collected during fieldwork. The field data was supplemented by another 44 GPS-points collected by Helge Henriksen during a previous project (Fig. 3.1; Appendix). Route tracks were chosen to get a good representation of all geological units, and to cover a large area. Steep terrain, scree deposits and numerous bogs made some constraints on the spatial distribution of field data. Additionally, 10 rock samples were collected and further prepared for thin section analyses and oxygen stable isotope ($\delta^{18}\text{O}$) analyses (Fig. 3.1).

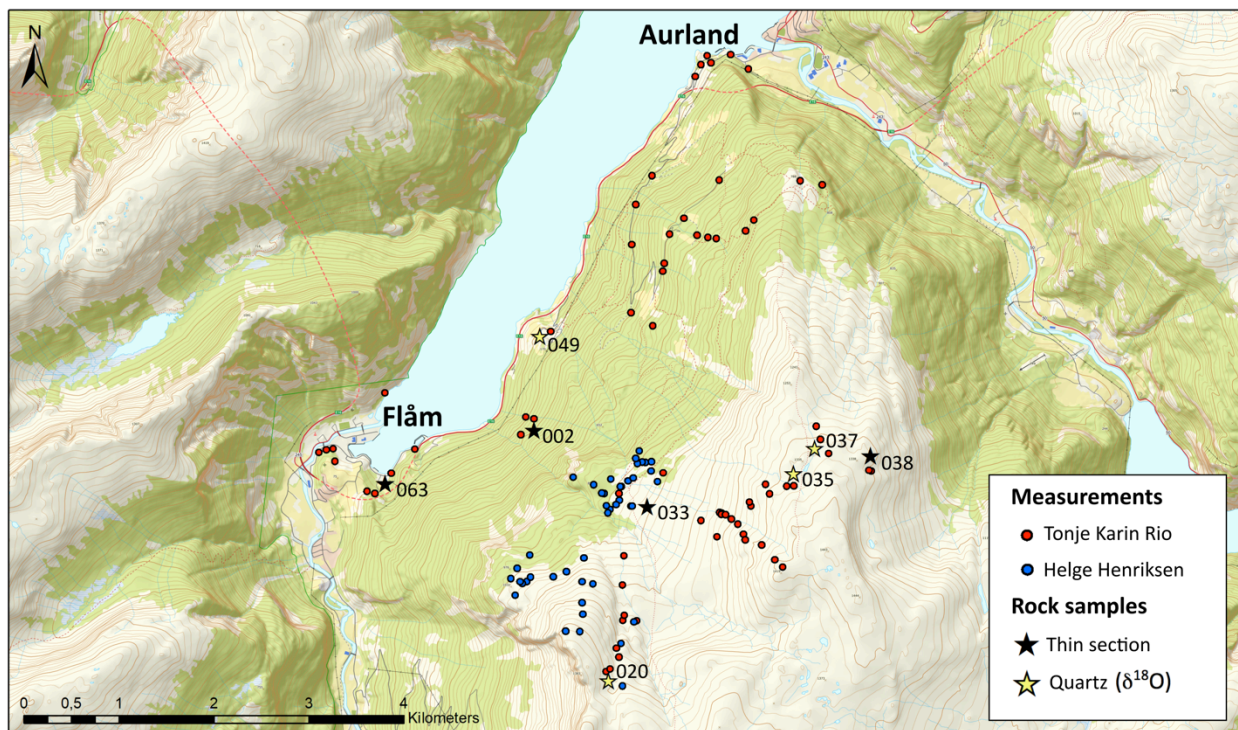


Fig. 3.1 – Overview of the study area, including the location of structural measurements (coloured dots), and the location of rock samples for thin section analyses and $\delta^{18}\text{O}$ analyses (stars).

3.1.1 Equipment

During the three weeks of fieldwork GPS points were collected using a Garmin handheld GPS, and structural measurements made using a geological compass. Structural data was recorded by measuring the dip-direction and dip, rather than strike and dip. This method was used consequently throughout the study. Observations were supplemented with photos, sketches and detailed field notes. To examine the rocks more closely, and to collect rock samples, a hand lens and geological hammer were used (Tab. 2).

Table 2 – Overview of equipment used during fieldwork.

Equipment	Type
GPS	Garmin GPSMAP 64s
Geological compass	Silva Expedition S with clinometer (modified)
Camera	Nikon D3100
Other tools	Hammer + Hand lens + Hydrochloric acid (HCl)

3.2 Software

3.2.1 ArcGIS 10.2

The software ArcGIS 10.2 was used for representation and processing of field data. Structural data collected during fieldwork was first sorted in Excel before ArcMap was used for spatial analyses and production of geological maps.

3.2.2 Stereonet 10

The software Stereonet 10 was used for plotting the orientation of linear and planar features, and to identify statistical significant structural trends for the study area.

3.2.3 Inkscape

The software Inkscape was used to edit photos and to produce figures.

3.3 Petrographic and kinematic analyses of thin sections

Four rock samples from the three main geological units (Tab. 6) were prepared and cut into hand specimen by a diamond saw at Western Norway University of Applied Sciences. The samples were further polished to 30µm thickness at a specialised thin-section laboratory in Warsaw, Poland. Petrographic and kinematic analyses were conducted using an optical microscope. Mineral assemblages of the different units and micro-scale kinematic indicators were identified, and used to supplement outcrop interpretations.

3.4 Oxygen stable isotope ($\delta^{18}\text{O}$) analyses

Six samples from various quartz veins in the phyllite (Tab. 8) were prepared for oxygen stable isotope ($\delta^{18}\text{O}$) analyses at the University of Lausanne. The samples were first cut by a diamond saw at Western Norway University of Applied Sciences, and further broken down into small 2 mg ‘chips’. The samples were then sent to the isotope laboratory, where $\delta^{18}\text{O}$ analyses were conducted using the laser fluorination method (Clayton & Mayeda, 1963) and a Finnigan MAT 253 mass spectrometer.

4 Results

The Stampa-area is characterised by three main geological units, which will be described in further detail below. Field observations provide general lithological and structural descriptions of the mapped units (Ch. 4.1). Structural and kinematic analyses make up a larger part of the fieldwork-chapter, as this is the main focus of the study. Supplementary thin section analyses provide more detailed descriptions of the mapped units with regards to mineralogy and micro-scale kinematic indicators (Ch. 4.2). $\delta^{18}\text{O}$ analyses contribute to further understanding of the regional deformation history with regards to paleo-circulation patterns of quartz rich fluids in the Fortun-Vang nappe complex (Ch. 4.3).

4.1 Fieldwork

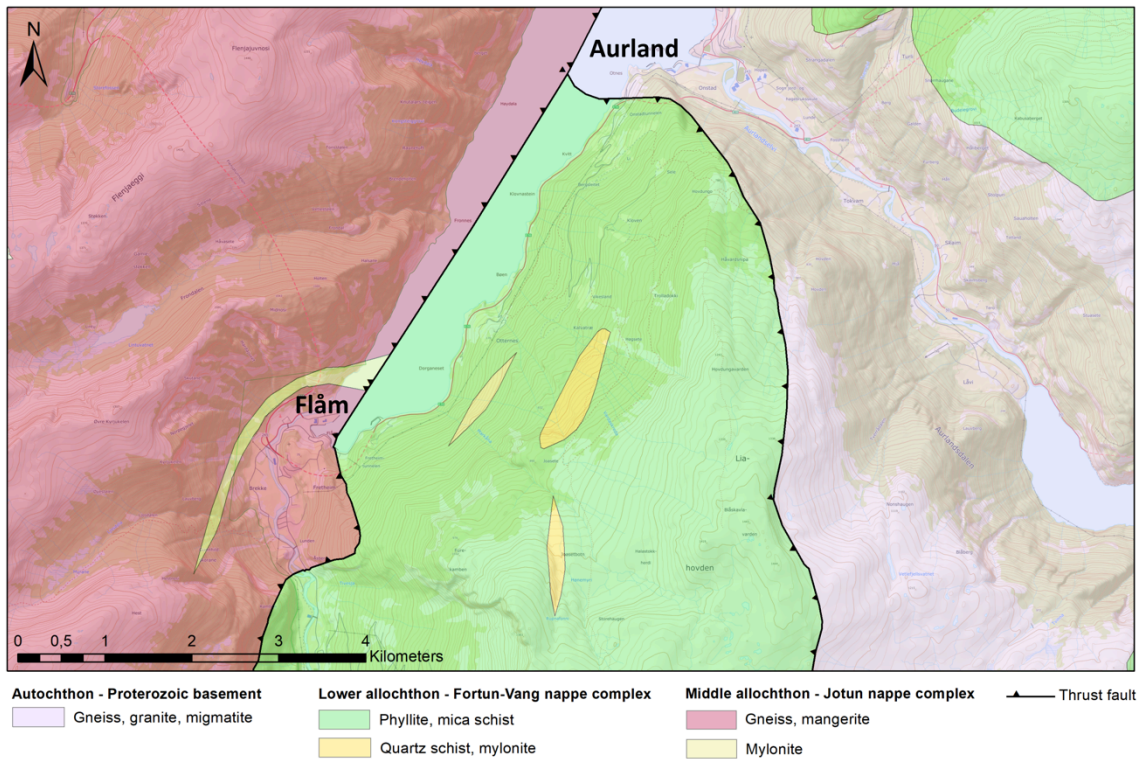


Fig. 4.1 – Updated bedrock geology map of the inner Aurlandsfjord including own observations. Note the two added mylonitic lenses within the phyllite. Modified after Bryhni (1977).

4.1.1 General lithological and structural descriptions of mapped units

The Proterozoic basement

A section across the Proterozoic basement shows a gradual increase in deformation intensity towards the overlying phyllite (Fig. 4.2). This transition is clearly identified at macro-scale looking at a vertical rock cliff exposing the uppermost 200 m of the basement. The lower part of the cliff is relatively massive compared to the upper, strongly foliated gneissic rock (Fig. 4.2a). The lower part of the cliff indicates a coarse-grained, little-deformed, crystalline texture with abundant K-feldspar minerals (Fig. 4.2b).



Fig. 4.2 – (a) Photograph showing a vertical cliff of Proterozoic basement rocks close to Aurlandsvangen. Note the increase in deformation intensity towards the overlying phyllite – from massive to strongly foliated gneissic rocks. S = main foliation. (b) Outcrop photograph showing little-deformed, granitic gneiss at the bottom of the cliff.

Towards the overlying phyllite, the crystalline basement rocks continuously grade into strongly foliated gneissic rocks characterised by a fine-grained matrix with alternating layers of augengneiss (Fig. 4.3a) and banded gneiss (Fig. 4.3b). Some layers close to the overlying contact have a mylonitic texture (Fig. 4.3c). The formation of mylonites is related to that of gneissic banding, but involves a higher degree of shear deformation (Fossen & Gabrielsen, 2005). Thus, mylonites have a more fine-grained texture with mm-thick layers.

Fracture-surfaces have developed parallel to the main foliation. Another sub-vertical joint set has developed perpendicular to the main foliation, which promotes cubic break-up of the rock mass and planar sliding of the cubes (Fig. 4.3d).

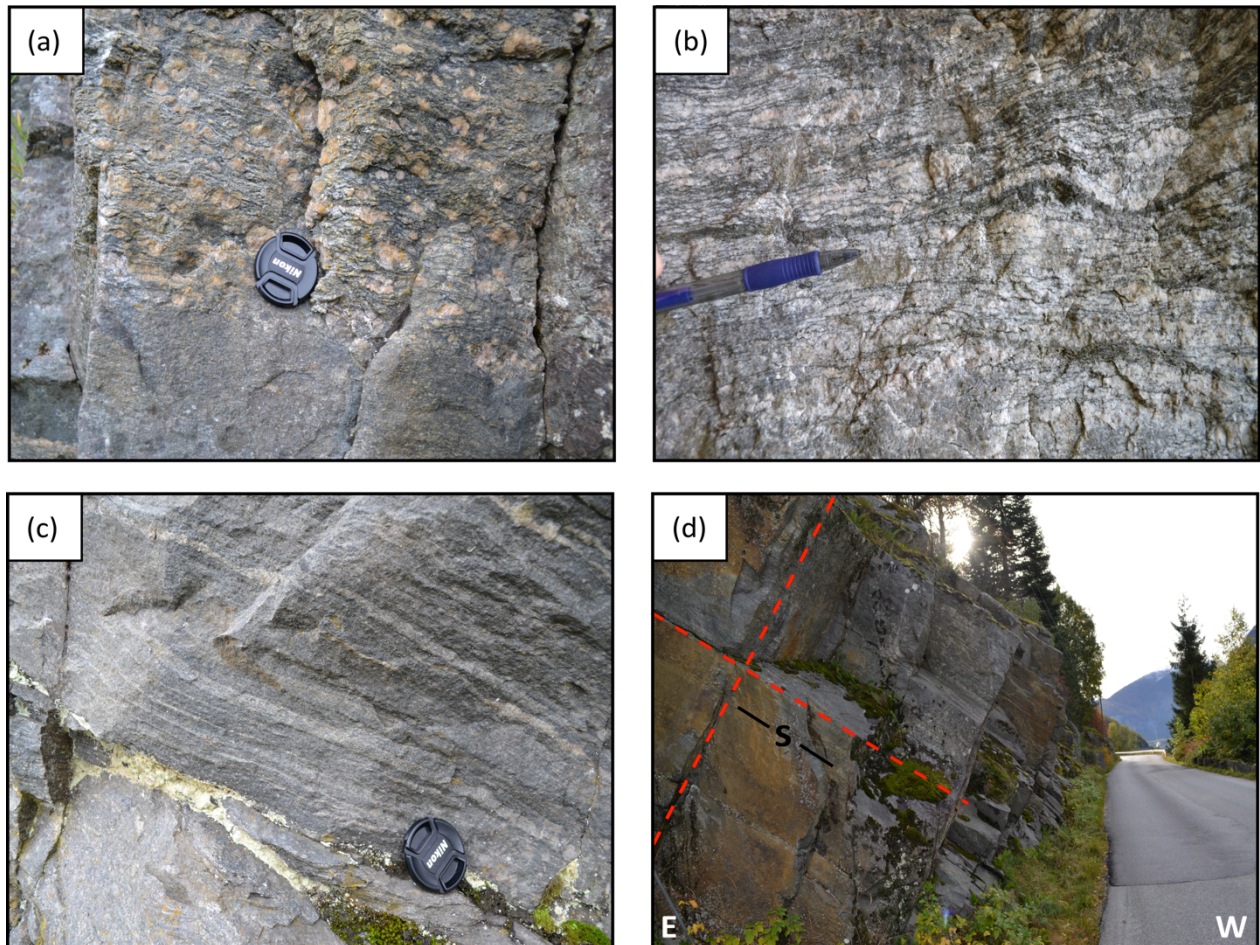


Fig. 4.3 – Field aspects of the Proterozoic basement. The rocks are dominated by alternating layers of (a) augengneiss and (b) banded gneiss. (c) Mylonites are found close to the overlying phyllite. (d) Fracture surfaces have developed parallel and perpendicular to the main foliation, which promote cubic break-up of the rock mass and planar sliding of the cubes. S = main foliation.

The Fortun-Vang nappe complex

The Fortun-Vang nappe complex is dominated by variably deformed phyllite and mica schist. The phyllite has a fine-grained texture with abundant mica and a silky lustre (Fig. 4.4a). Some layers of graphite are present within the unit (Fig. 4.4b), as well as more competent quartz-rich layers (Fig. 4.4c).

The foliation is penetrative with a relatively planar appearance in the competent quartz-rich layers. The less competent graphite- and mica-rich layers are folded at various scales. Isoclinal (F_1) folds have a fold axis parallel to the main stretching lineation in the area, and are overprinted by open (F_2) folds with associated crenulation lineations (Fig. 4.4d). This observation indicates a relative chronological order of formation with at least two main fold generations.

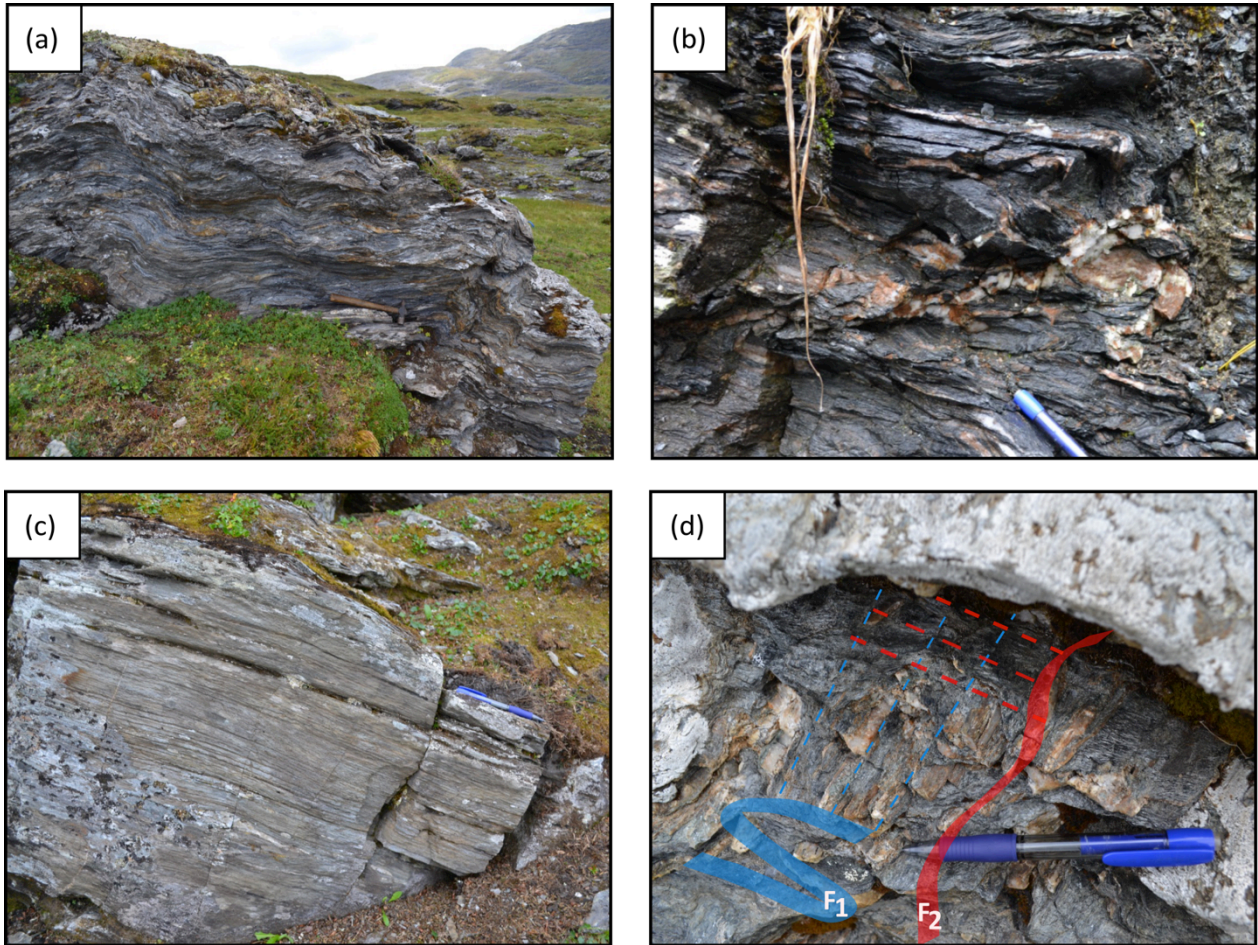


Fig. 4.4 – Representative photographs of (a) the phyllite with layers of (b) graphite and (c) more competent layers dominated by quartz. (d) Two main fold generations can be recognised within the phyllite, with fold axes (stippled lines) perpendicular to each other.

The competent quartz-rich layers correspond to three mylonitic lenses developed in quartzitic schist (Fig. 4.1). These lenses are variably deformed, with mm-thick layers of ultramylonitic texture developed in the lens at the lowest elevation (Fig. 4.5a). This ultramylonitic lens has a distinct foliation with penetrative stretching lineations (Fig. 4.5b) and local folds (Fig. 4.5c). The contact to the surrounding phyllite is relatively sharp (Fig. 4.5d).

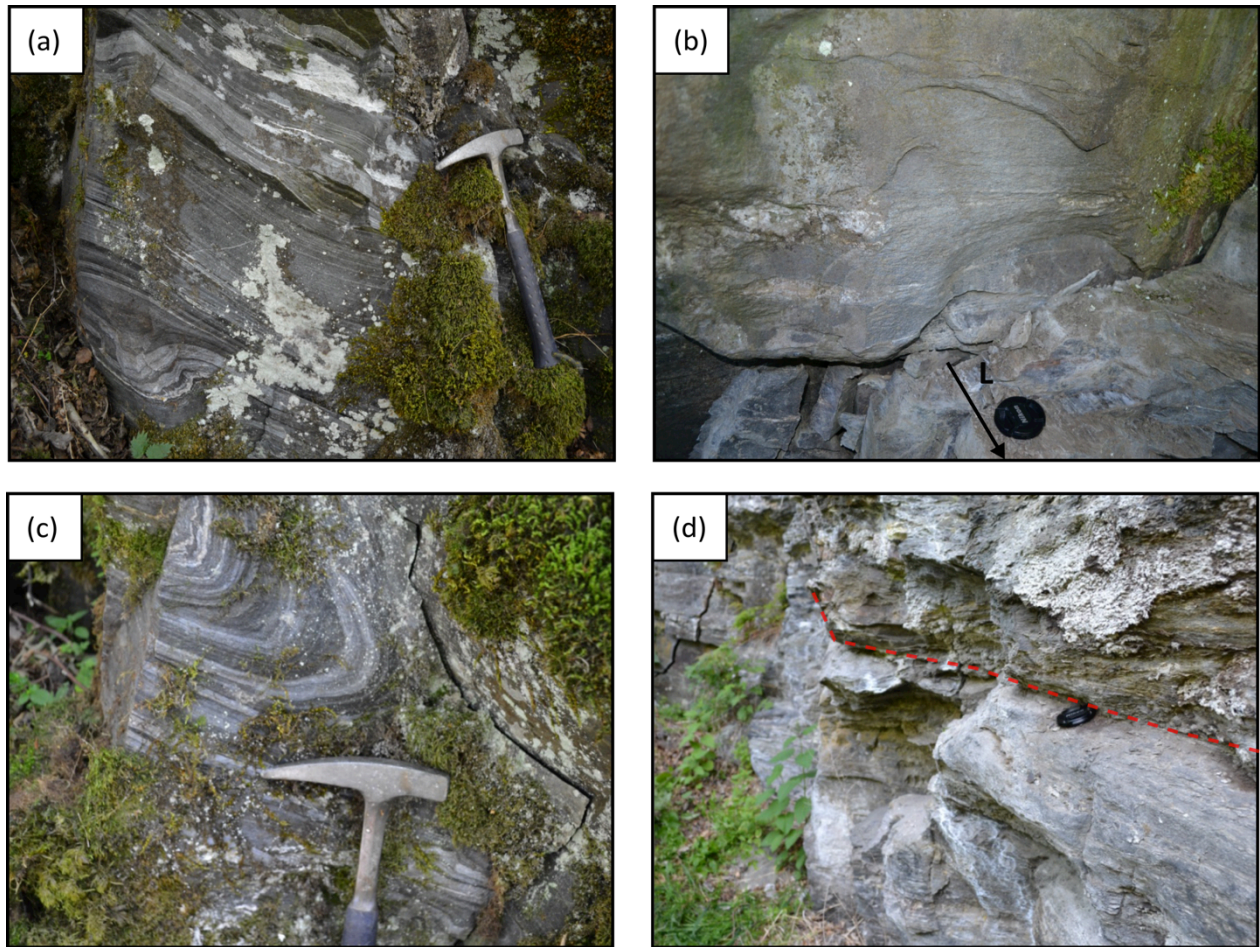


Fig. 4.5 – The ultramylonitic lens at the lowest elevation has (a) a penetrative foliation with (b) associated stretching lineations. The foliation is mainly planar, but some degree of (c) internal folding is present. (d) The contact to the overlying phyllite is relatively sharp.

The Jotun nappe complex

The Jotun nappe complex is dominated by variably deformed mangeritic gneiss. Field observations suggest a gradual increase in deformation intensity towards the underlying phyllite. The upper part of the unit is characterised by cm-thick alternating pink toned felsic and dark mafic layers, which are heavily folded (Fig. 4.6a). This part of the unit is relatively massive, with no distinct joint sets. Moving towards the underlying phyllite, the unit becomes mylonitic with a fine-grained texture and mm-thick layers. The foliation becomes more planar with no internal folding (Fig. 4.6b). Fracture-surfaces have developed parallel to the main foliation. The unit shows signs of both ductile and brittle deformation, through the presence of shear bands (Fig. 4.6c) and fault sets (Fig. 4.6d).

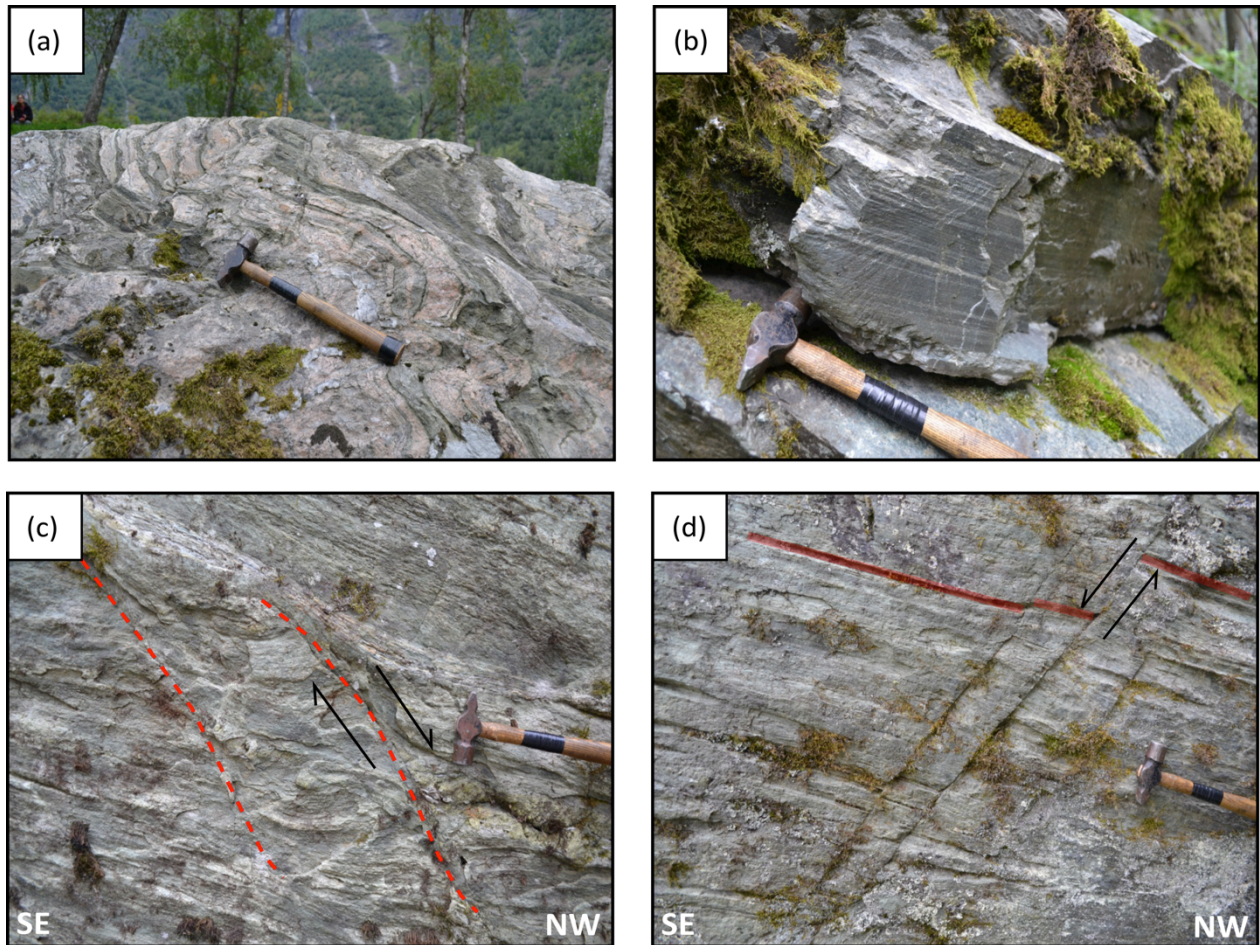


Fig. 4.6 – An increase in deformation intensity is observed within the Jotun nappe complex, from (a) coarse-grained banded gneiss to (b) mylonite towards the underlying phyllite. Note the presence of (c) ductile shear bands and (d) brittle fault sets within the unit.

4.1.2 Detailed structural and kinematic analyses of field data

The Stampa-area is characterised by the abundance of ductile, semi-brittle and brittle deformation features, which define the large-scale structural style of the area. Previous studies (Blikra & Berg, 2013; Böhme et al., 2013) have aimed solely towards mapping of foliation and joint sets within the phyllite. This study provides detailed and comprehensive structural and kinematic analyses of all structural features. Since these features show similar orientations within the mapped units, they will be discussed together in this chapter. Firstly, an overview of representative measurements (Fig. 4.7; Appendix) and the average orientation of ductile, semi-brittle and brittle deformation features (Fig. 4.8) is provided. Secondly, these features are discussed separately to identify statistical significant structural trends and kinematic indicators within the study area.

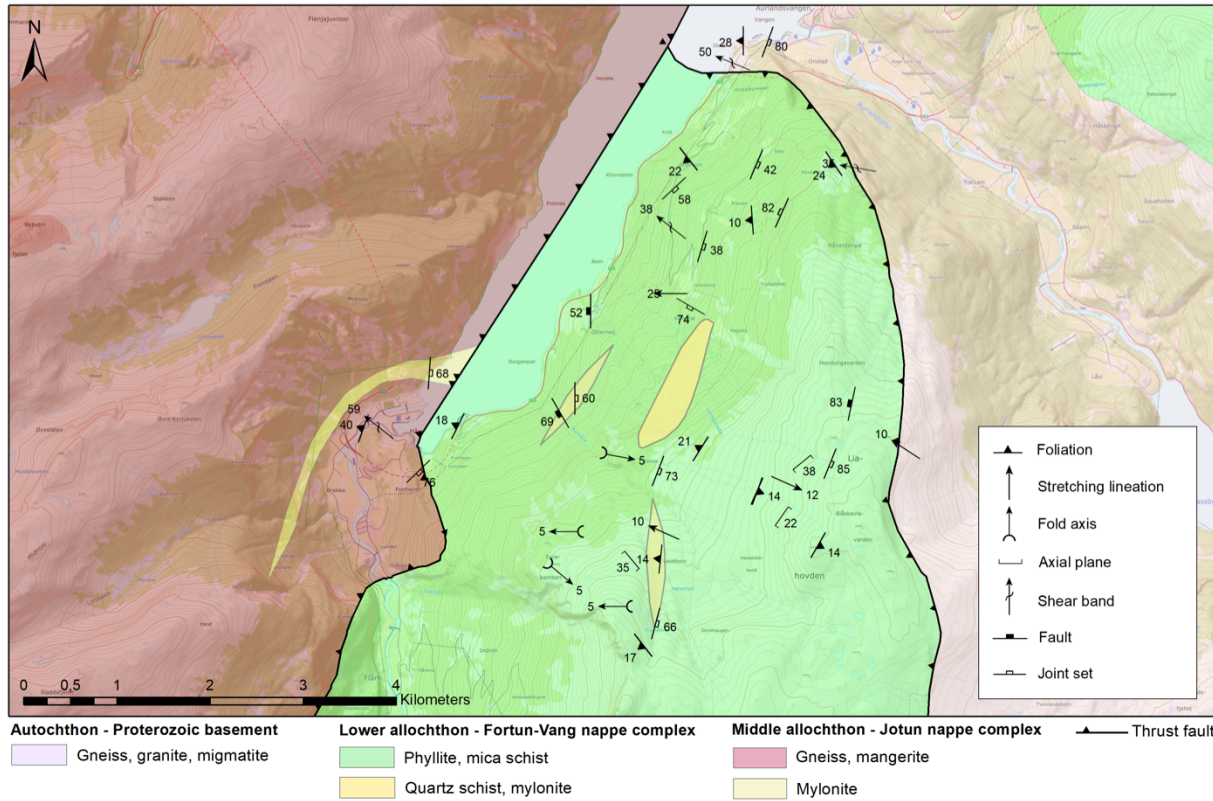


Fig. 4.7 – Bedrock geology map of the inner Aurlandsfjord with representative measurements of ductile, semi-brittle and brittle structures.

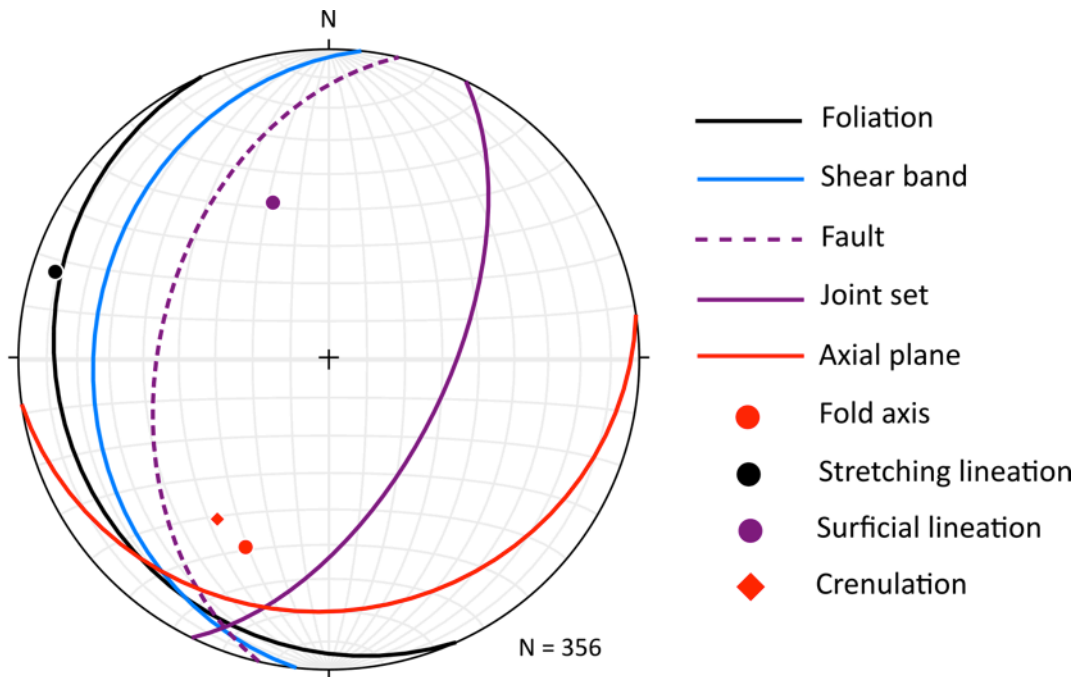


Fig. 4.8 – Stereoplot showing the average orientation of ductile, semi-brittle and brittle structures within the study area.

Ductile structures

Foliation

The foliation within the study area has an average dip towards the WSW (Fig. 4.9). There is minor variance between and within the different units (Tab. 3). The foliation within the Proterozoic basement and the Jotun nappe complex shows a similar trend, with a shallow to moderate dip towards the W. The foliation within the Fortun-Vang nappe complex has a more variable orientation due to large-scale folding of the phyllite, but on average the foliation is dipping shallowly towards the WSW.

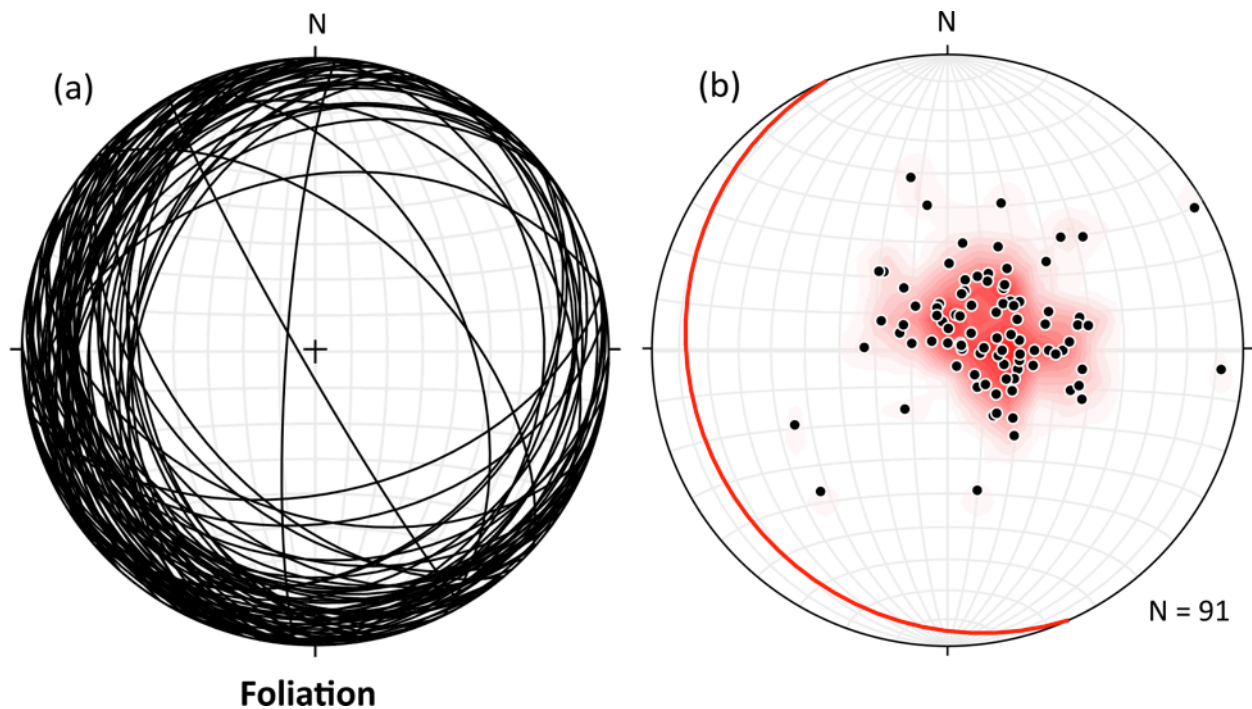


Fig. 4.9 – Stereoplot showing (a) all foliation measurements within the study area, and (b) average foliation calculated from associated poles.

Table 3 – Average foliation of different units within the study area.

Unit	Rock type	Foliation
Proterozoic basement	Migmatitic gneiss	256/31
Fortun-Vang nappe complex	Phyllite and mica schist	218/22
Fortun-Vang nappe complex	Mylonitic lens	229/31
Jotun nappe complex	Mangeritic gneiss	273/26

Stretching lineations

Stretching lineations are especially well developed in deformed quartz veins within phyllite (Fig. 4.10). These lineations are penetrative, meaning that they are pervasive throughout the rock mass rather than confined to a sliding plane. The orientation of stretching lineations within the study area shows the same trend within all units, with a consistent plunge towards the WNW. Some locations show a plunge in the opposite direction, towards the ESE (Fig. 4.10).

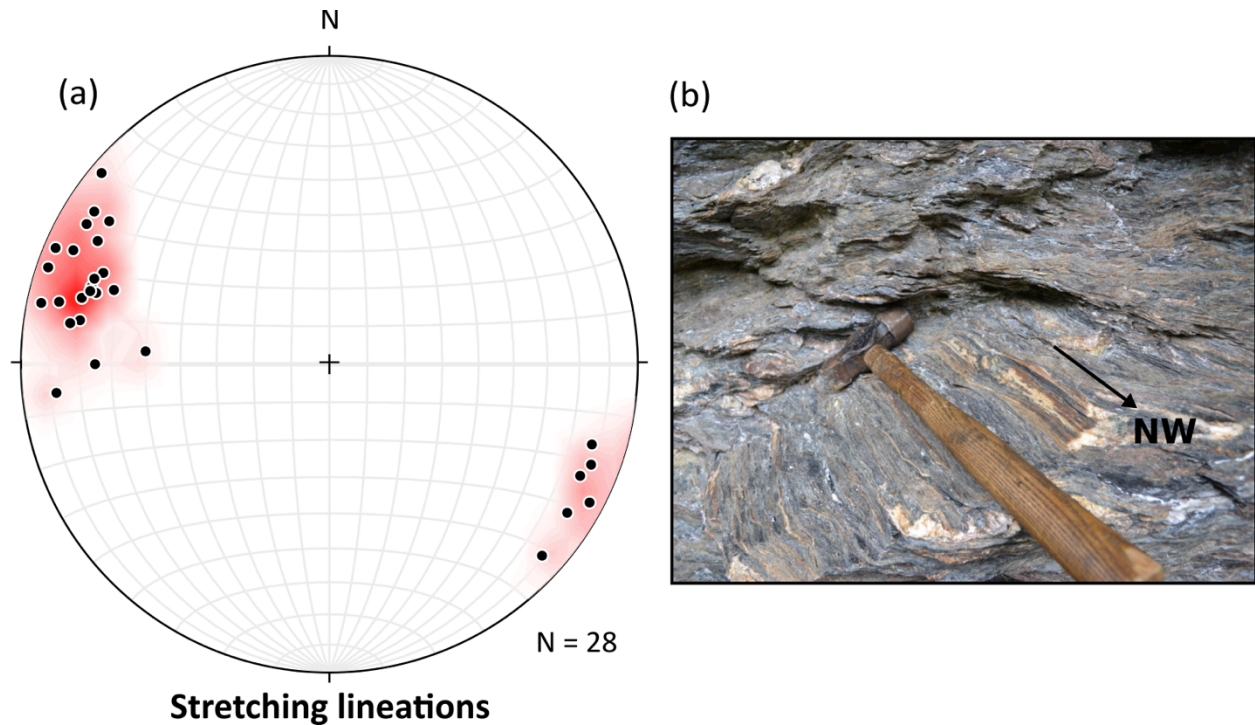


Fig. 4.10 – (a) Stereoplot and (b) photograph showing the orientation of stretching lineations within the study area.

Table 4 – Average stretching lineation of different units within the study area.

Unit	Rock type	Stretching lineation
Proterozoic basement	Migmatitic gneiss	290-30
Fortun-Vang nappe complex	Phyllite and mica schist	289-04
Fortun-Vang nappe complex	Mylonitic lens	280-19
Jotun nappe complex	Mangeritic gneiss	290-25

Folds

Folds are present in all units, but especially abundant within the less competent layers of the phyllite. The orientation of fold axes show indistinct and diverging patterns across the study area, which probably reflect local variations and multiple fold generations. On average the fold axes are plunging moderately towards the SSW (Fig. 4.11). Associated axial planes are dipping moderately towards the SSE (Fig. 4.11), which supports field observations of NNW-verging folds (Fig. 4.12).

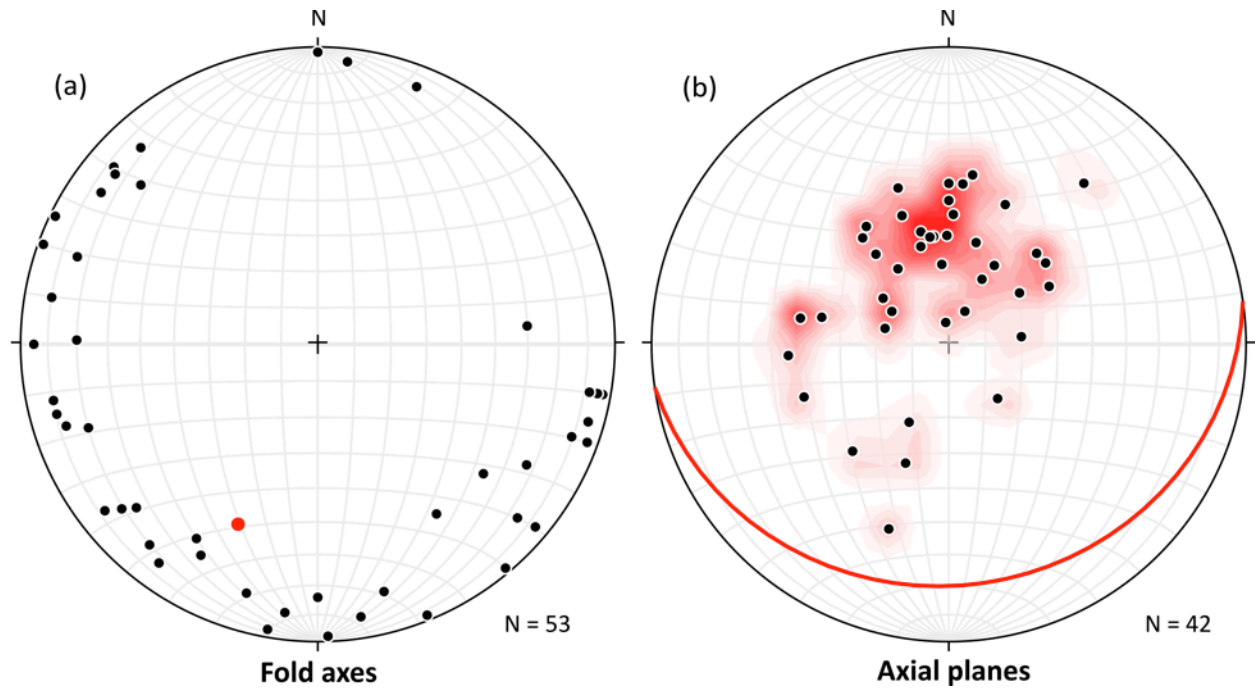


Fig. 4.11 – Stereoplot showing the orientation of (a) fold axes and (b) associated axial planes within the study area. Average orientation is marked in red.

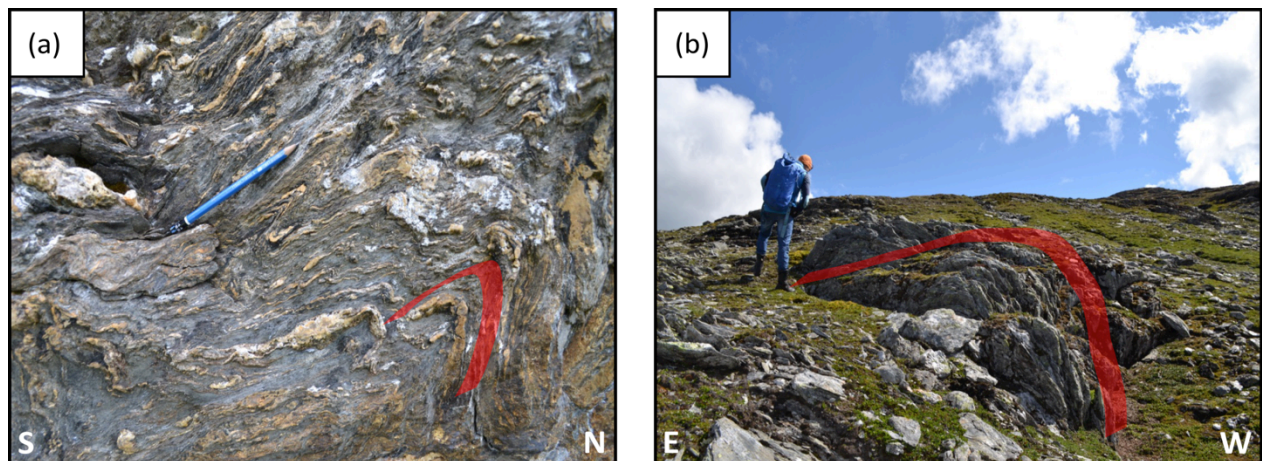


Fig. 4.12 – Photographs of NW-verging folds observed within the study area.

As mentioned earlier there are at least two main fold generations in the area, based on observations of overprinting structures. Isoclinal (F_1) folds with a fold axis parallel to the main stretching lineation in the area are overprinted by open (F_2) folds with associated crenulation lineations. This observation indicates that the isoclinal folds were formed prior to the open folds, and probably simultaneously to the penetrative stretching lineations. Stereoplot supports field observations of isoclinal (F_1) fold axes developed perpendicular to open (F_2) fold axes (Fig. 4.13).

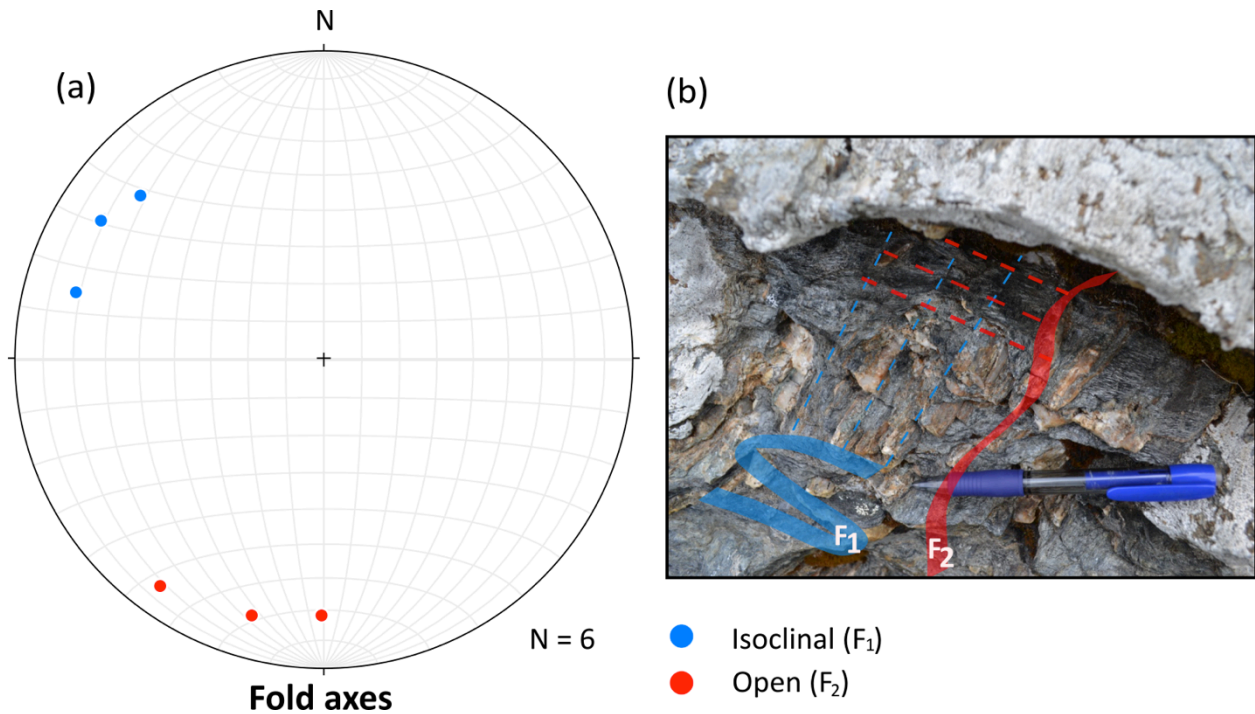


Fig. 4.13 – (a) Stereoplot and (b) photograph showing the orientation of isoclinal (F_1) and open (F_2) fold axes.

Shear bands

Most shear bands within the study area are dipping towards the WNW (Fig. 4.14), which is a consistent trend throughout the three main geological units. Shear bands are abundant in the phyllite, but can also be found in the surrounding units. Shear bands are especially visible in the less competent layers of the phyllite with intercalated quartz veins as marker horizons (Fig. 4.15).

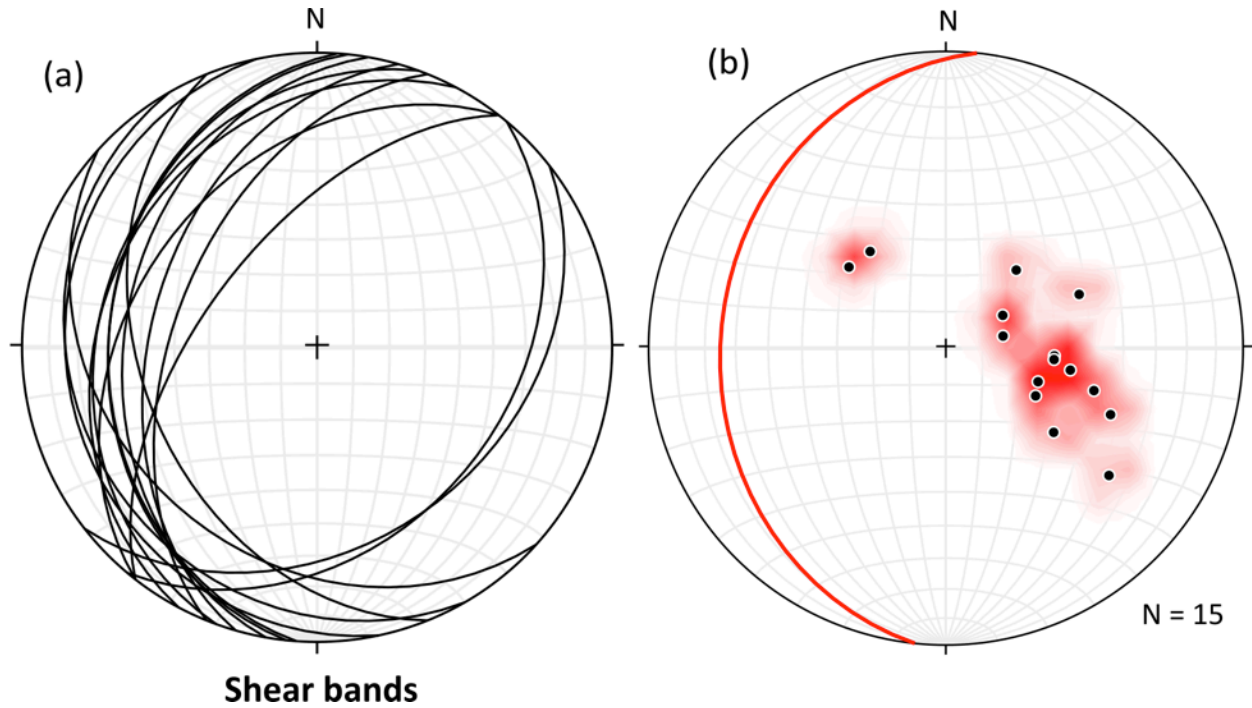


Fig. 4.14 – Stereoplot showing (a) the orientation of all shear bands within the study area, and (b) average orientation calculated from associated poles.

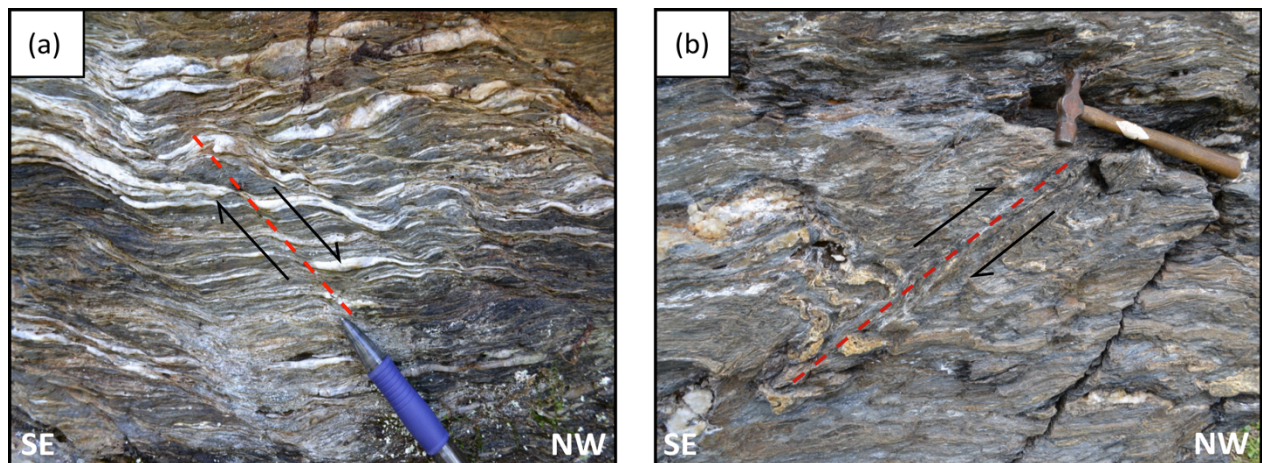


Fig. 4.15 – Photographs showing (a) normal shear bands and (b) reverse shear bands with top-to-the-NW sense of movement.

Semi-brittle to brittle structures

Faults

Semi-brittle to brittle faults tend to follow N-S striking fault zones. These fault zones are large-scale structures that are present throughout the study area. The observed faults represent normal faults with an average dip towards the W (Fig. 4.16; Fig. 4.17). The dip is moderate to steep, and surficial lineations with slickensides are present on the fault plane. These lineations are generally plunging towards the NNW indicating oblique sliding along the fault plane.

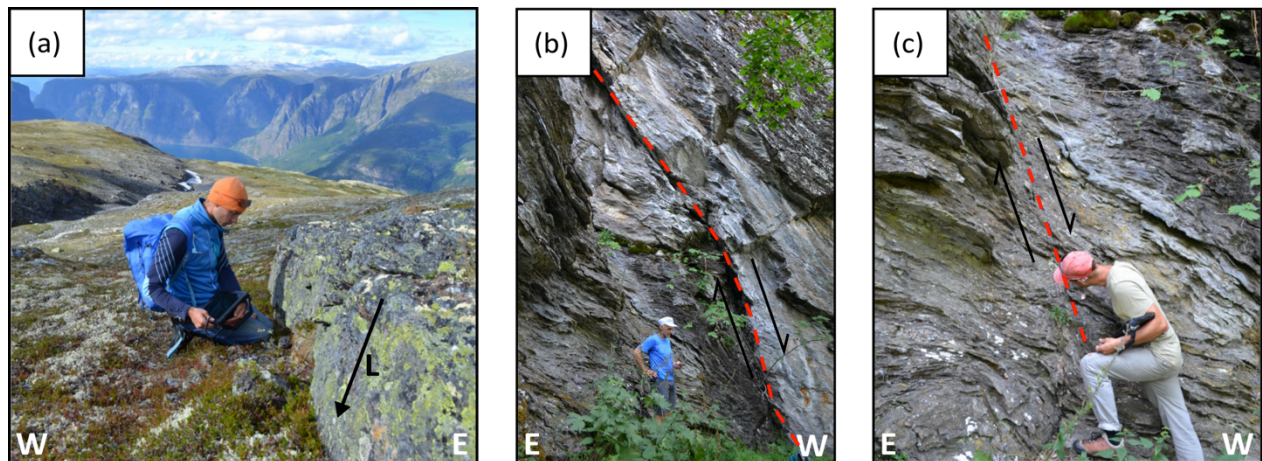


Fig. 4.16 – N-S striking brittle to semi-brittle faults that indicate top-to-the-W sense of movement.

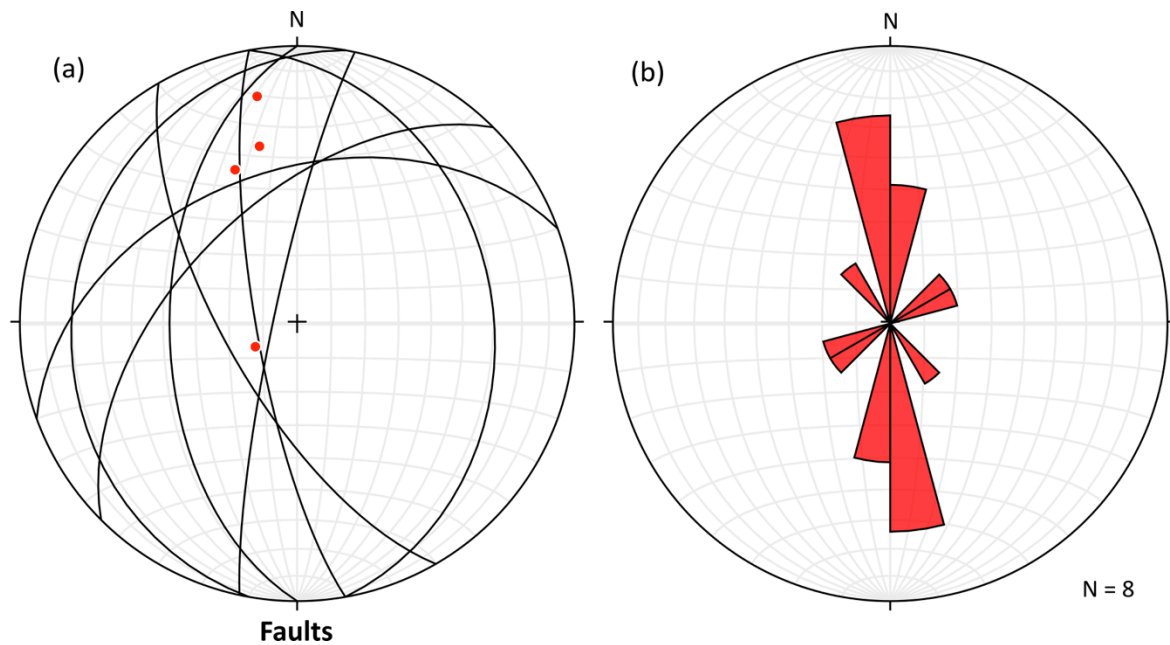


Fig. 4.17 – Stereoplot showing (a) the orientation of faults and surficial lineations (red dots) within the study area, and (b) a rose diagram that indicates a trend of N-S striking faults.

Joint sets

Three main brittle joint sets were observed within the study area, striking (1) NNE-SSW, (2) NE-SW and (3) WNW-ESE (Fig. 4.18; Fig. 4.19). The majority is striking NNE-SSW and defines large-scale structures such as open gravitational fractures in the back-bounding area of the unstable area(s) (Fig. 4.18). These joint sets are generally dipping steeply to sub-vertically towards the ESE (Fig. 4.19).

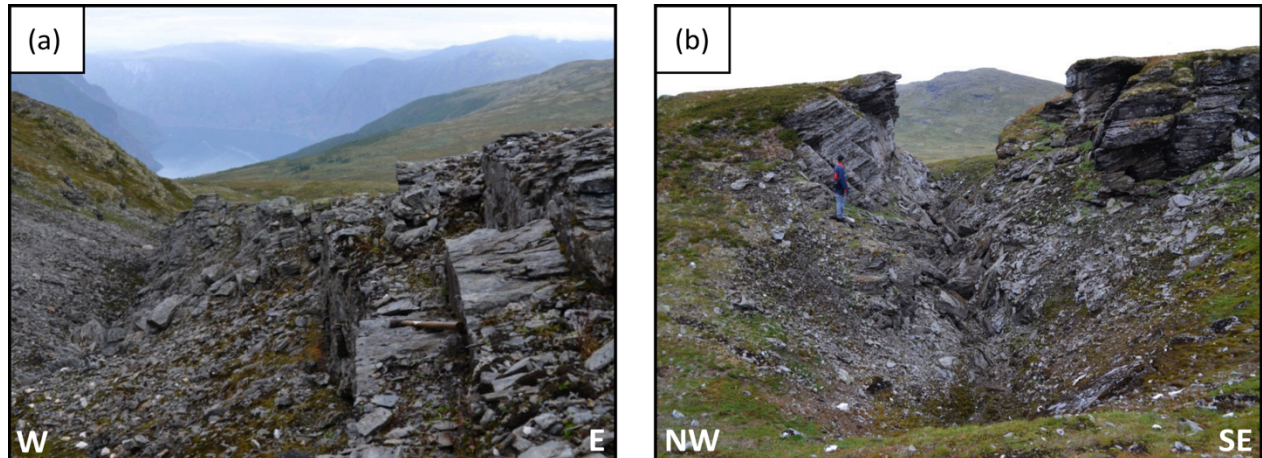


Fig. 4.18 – Photographs showing (a) a sub-vertical joint set that follows a large-scale fault zone striking N-S and (b) an open gravitational fracture striking NE-SW.

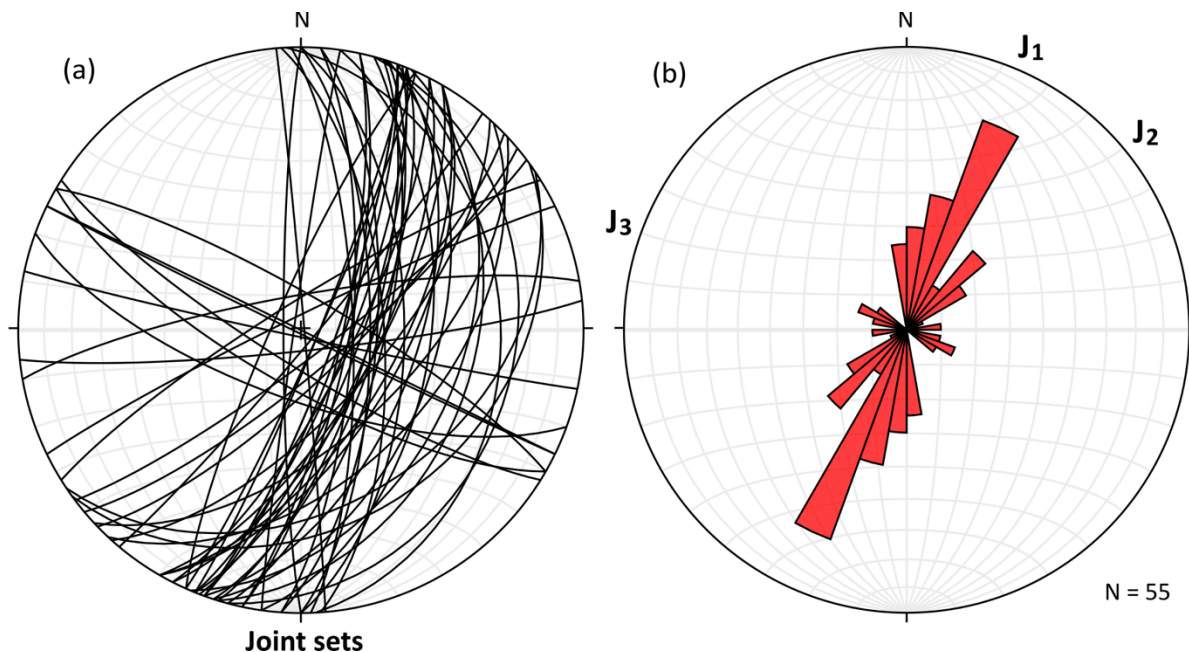


Fig. 4.19 – Stereoplot showing (a) the orientation of joint sets within the study area, and (b) a rose-diagram that represents statistical significant trends of three main joint sets, most of which are striking NNE-SSW.

Kinematic indicators

Table 5 provides an overview of meso- to macro-scale kinematic indicators identified during fieldwork. The majority of kinematic indicators point towards top-to-the-NW sense of movement, but some indicators of top-to-the-SE sense of movement were found in the Fortun-Vang nappe complex.

Table 5 – Overview of meso- to macro-scale kinematic indicators identified during fieldwork.

Unit	Rock type	Kinematic indicators	Sense of movement
Proterozoic basement	Migmatitic gneiss	- Stretching lineations - Shear bands	Top-to-the-NW
Fortun-Vang nappe complex	Phyllite and mica schist	- Stretching lineations - Shear bands - Asymmetric folds - Semi-brittle faults	Top-to-the-NW, Top-to-the-SE
Fortun-Vang nappe complex	Mylonitic lens	- Stretching lineations - Asymmetric folds	Top-to-the-NW, Top-to-the-SE
Jotun nappe complex	Mangeritic gneiss	- Stretching lineations - Shear bands	Top-to-the-NW

4.1.3 Geological profiles

Four geological profiles at various locations across the unstable mountain slope are presented in this study (Fig. 4.20; Fig. 4.21). These profiles are based on subjective interpretations and extrapolation of local structural measurements.

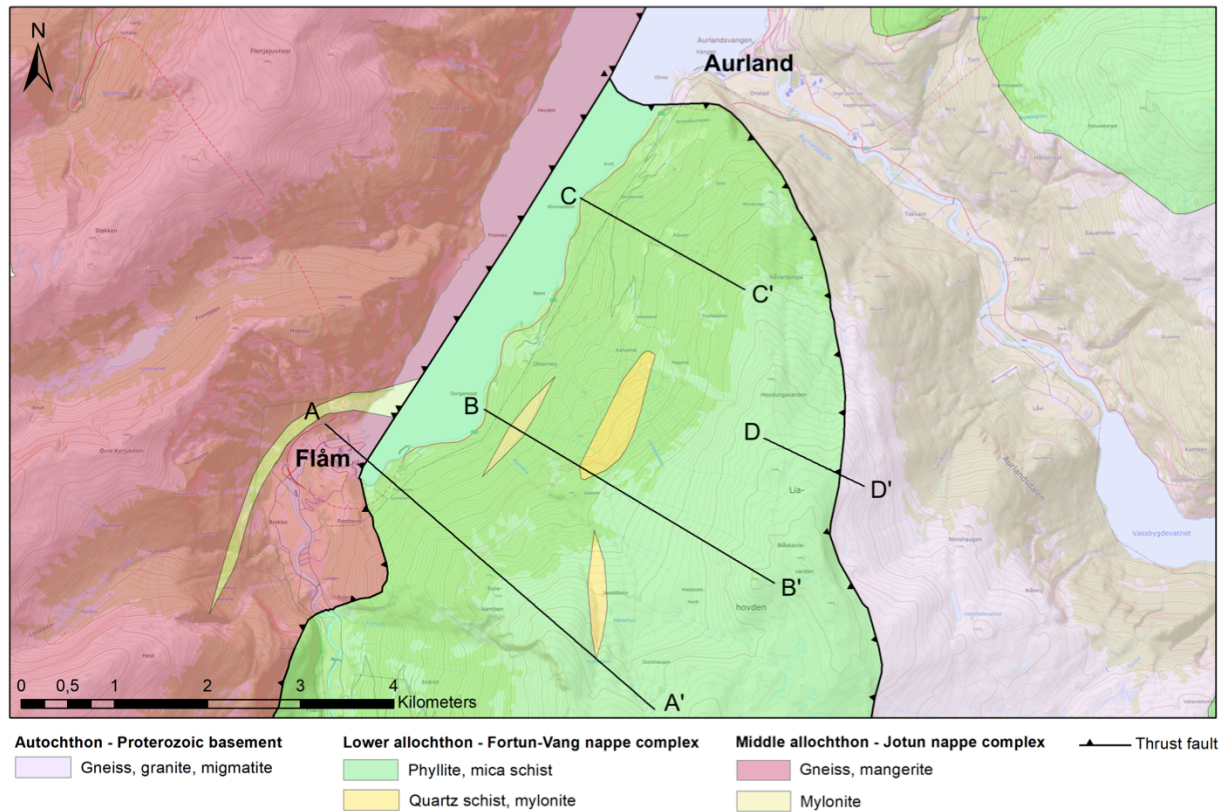


Fig. 4.20 – Bedrock geology map of the inner Aurlandsfjord showing the trace of the four geological cross-sections presented in this study (Fig. 4.21).

Ductile and semi-brittle structures are generally dipping towards the fjord (NW), whereas brittle structures are generally dipping in the opposite direction (towards the SE). This general trend is disturbed by large-scale folding patterns, which makes the situation more complex (Fig. 4.21).

The upper part of the mountain slope seems to be more heavily folded than the lower part of the mountain slope (Profile B-B'). This increase in folding intensity towards the top of the mountain slope is supported by own field observations. Looking at the varying large-scale folding patterns between the geological cross-sections, there is also an increase in folding intensity towards the north. Open folds dominate the southernmost profile (Profile A-A') while more closed folds dominate the northern part of the study area (Profile C-C'). The three mylonitic lenses observed within the phyllite can be traced and connected along with these folding patterns (Fig. 4.21).

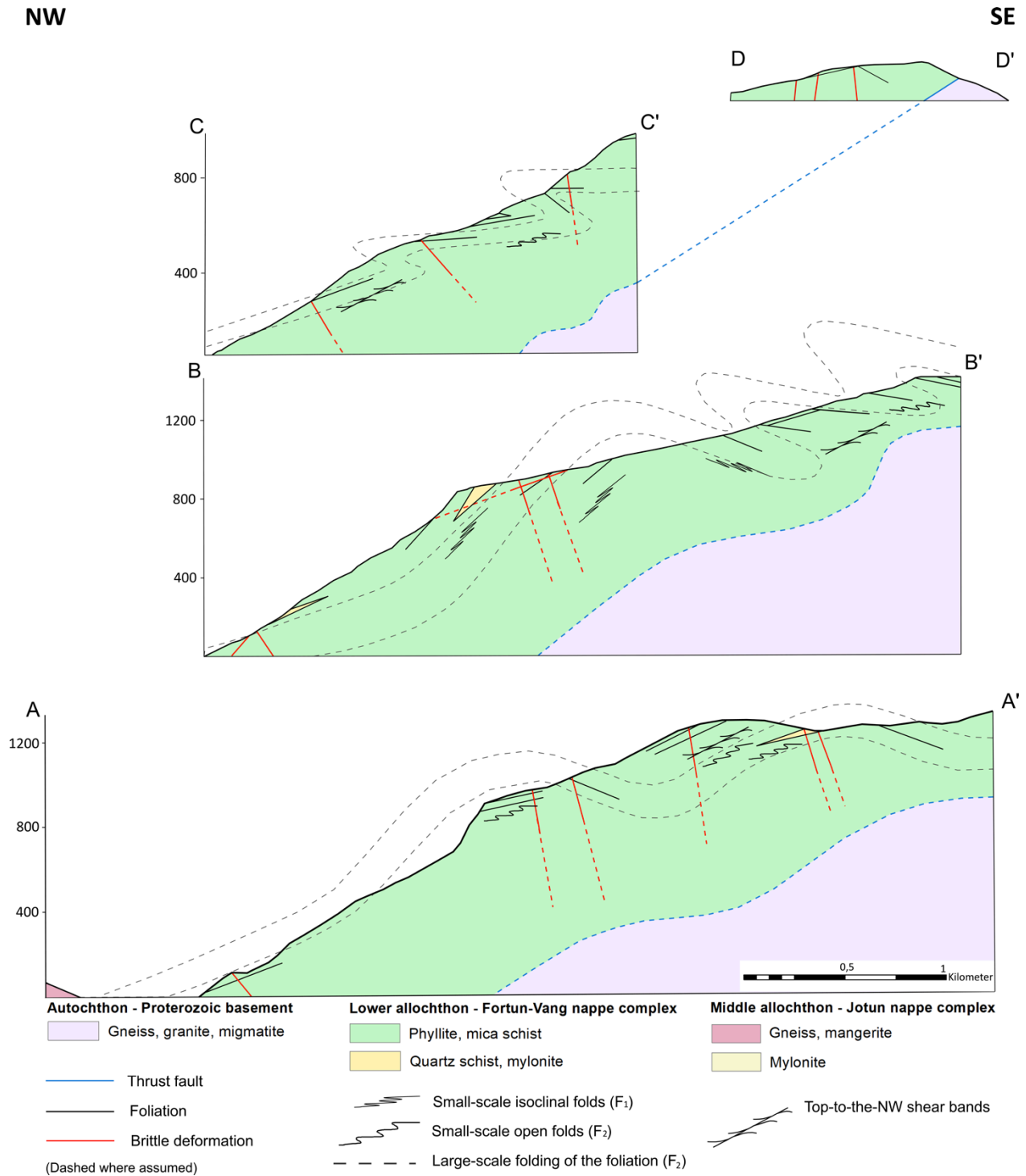


Fig. 4.21 – Schematic geological cross-sections showing the large-scale lithological and structural style of the Stampa-area.

4.2 Petrographic and kinematic analyses of thin sections

Ductile and brittle deformation features can also be observed at micro-scale. Ductile deformation is characterised by the formation of sub-grains, dislocations and twinning-structures (Fossen & Gabrielsen, 2005). These features represent irregularities or defects within the crystal structure, which increase the amount of free energy in the system. The crystal will try to ‘heal’ itself by getting rid of these defects in order to achieve a more stable state. This process is known as recrystallisation, and happens through reorganisation of atoms by diffusion or dislocation creep (Fossen & Gabrielsen, 2005). Recrystallisation often accommodates the formation of shape-preferred orientations, through rotation of sub-grains and formation of new grain boundaries (Vauchez, 1980). Brittle deformation can be identified through inter- and intragranular fractures (Fossen & Gabrielsen, 2005). Table 6 provides an overview of samples studied at micro-scale.

Table 6 – Overview of samples used for thin section analyses, with associated stretching lineations.

Sample no.	Unit	Rock type	Stretching lineation
038	Proterozoic basement	Migmatitic gneiss	290-30
033	Fortun-Vang nappe complex	Phyllite and mica schist	289-04
002	Fortun-Vang nappe complex	Mylonitic lens	280-19
063	Jotun nappe complex	Mangeritic gneiss	290-25

The Proterozoic basement

The sample collected from the Proterozoic basement is dominated by alternating layers of quartz and phyllosilicates (Fig. 4.22a). Muscovite appears to be the most common phyllosilicate within the sample, but some layers of biotite can also be identified. The quartz-rich layers consist nearly exclusively of recrystallised, elongated quartz grains with a ribbon texture (Fig. 4.22a). Ribbon grains are characterised by diffuse grain boundaries, and the formation of sub-grains and boundaries within the original quartz grain (Vauchez, 1980). These coarse-grained ribbons show a general trend in shape-preferred orientation towards the NW.

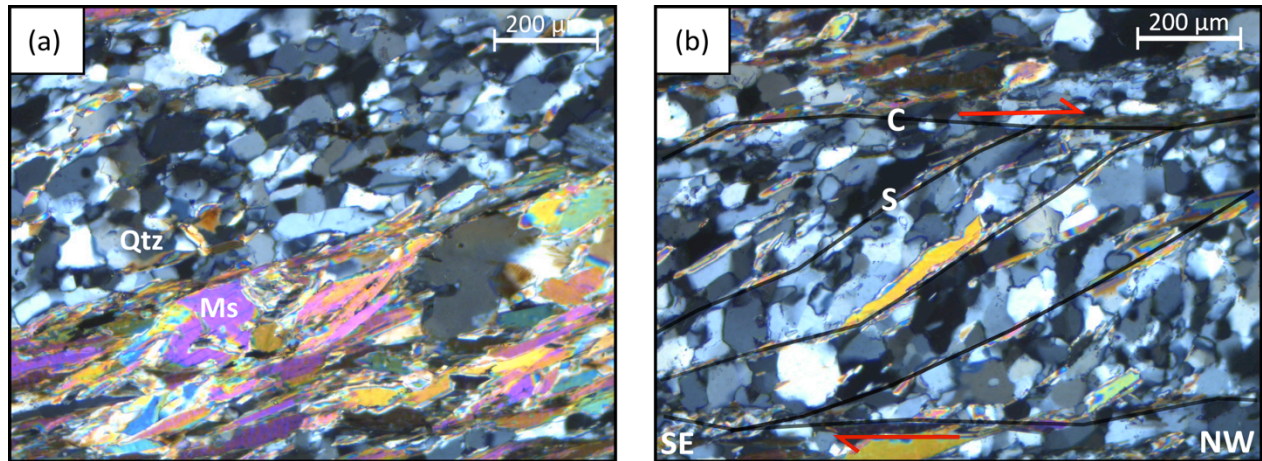


Fig. 4.22 – Thin section photographs of sample 038 in cross-polarised light showing (a) distinct layers of ribbon quartz and phyllosilicates, and (b) top-to-the-NW shear bands (S-C fabric).

The sample has a relatively distinct foliation, with elongated minerals oriented parallel or oblique to the main foliation. Top-to-the-NW shear bands represent this range in orientation (Fig. 4.22b). Asymmetric mica crystals within the layers of phyllosilicates also indicate top-to-the-NW sense of movement (Fig. 4.23a).

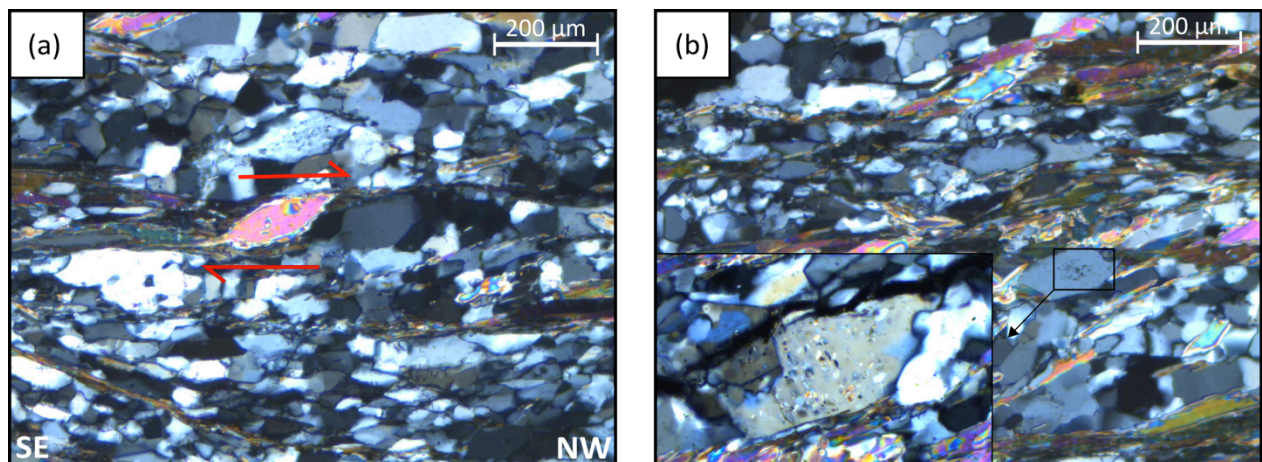


Fig. 4.23 – Thin section photographs of sample 038 in cross-polarised light showing (a) a mica fish with top-to-the-NW sense of movement, and (b) a feldspar crystal with fluid inclusions.

Some scattered, large feldspar crystals are present in the sample (Fig. 4.23b). These crystals are characterised by fluid inclusions, which can provide information of crystal-growth conditions and metamorphism of the host mineral (Crawford & Hollister, 1986). Intragranular fractures suggest that the feldspar crystals underwent more brittle deformation than the surrounding layers of quartz and phyllosilicates.

The Fortun-Vang nappe complex – Phyllite and mica schist

The sample collected from the phyllite is strongly foliated, with elongated and fine-grained minerals (Fig. 4.24a). The mineral composition is dominated by recrystallised ribbon quartz together with distinct layers of mica including muscovite and biotite. Aggregates of chlorite and possibly sericite are present in between the alternating layers (Fig. 4.24b), which may indicate retrograde metamorphism (Schwartz & Todd, 1941). The orientation of ribbon quartz compared to the main foliation indicates top-to-the-NW sense of movement (Fig. 4.25a). Some shear bands indicating top-to-the-SE sense of movement are present within the layers of phyllosilicates (Fig. 4.25b).

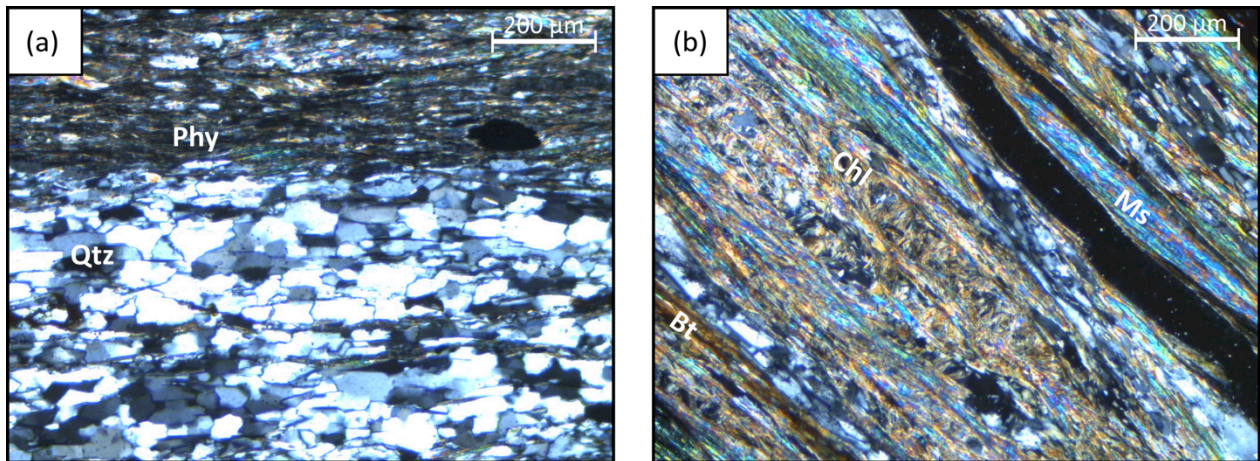


Fig. 4.24 – Thin section photographs of sample 033 in cross-polarised light showing (a) alternating layers of phyllosilicates and ribbon quartz. (b) Biotite, muscovite and chlorite are abundant phyllosilicates within the phyllite.

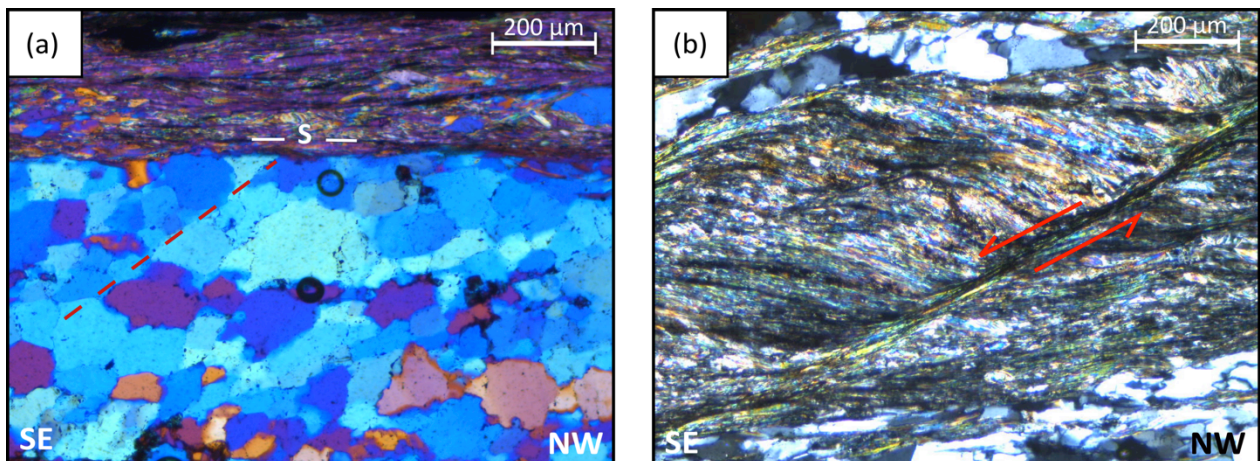


Fig. 4.25 – Thin section photographs of sample 033 in cross-polarised light (a) with an accessory plate of gypsum. The photographs are showing (a) the shape-preferred orientation in the ribbon quartz compared to the main foliation (indicating top-to-the-NW sense of movement), and (b) top-to-the-SE shear bands (S-C' fabric).

The Fortun-Vang nappe complex – Mylonitic lens

Large feldspar crystals are abundant within the mylonitic lens located at the lowest elevation (Fig. 4.1; Fig. 4.26a). These crystals correspond to plagioclase, due to the distinct twinning-structure observed at micro-scale (Fig. 4.26b). The matrix is further dominated by quartz, micas and some scattered carbonate grains. Both top-to-the-NW and top-to-the-SE kinematic indicators in the form of shear bands and feldspar crystals with associated pressure shadows are found within the sample. These pressure shadows are composed of different types of mica minerals. It seems like muscovite is related to top-to-the-NW sense of movement (Fig. 4.27a), whereas biotite is related to top-to-the-SE sense of movement (Fig. 4.27b).

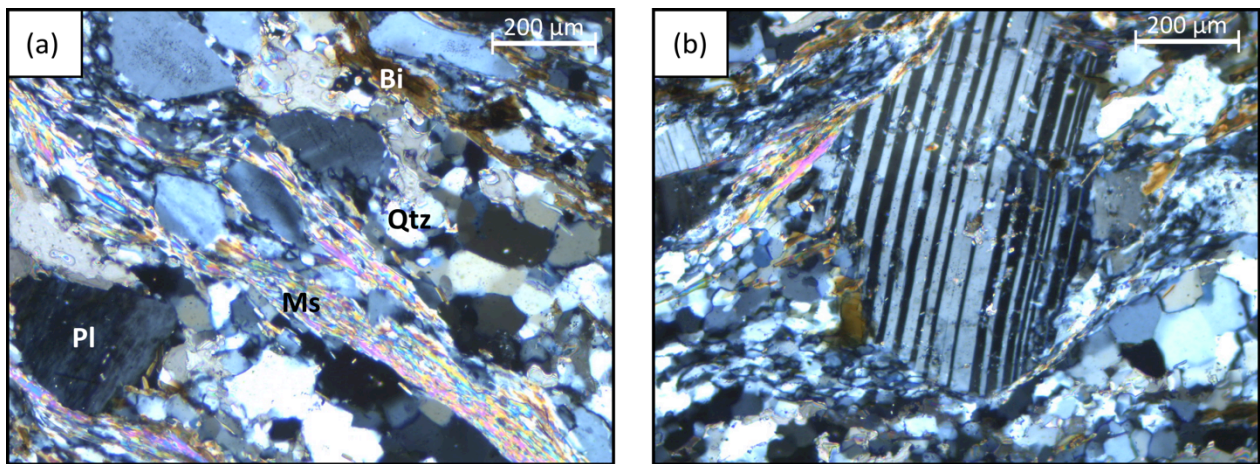


Fig. 4.26 – Thin sections photographs of sample 002 in cross-polarised light showing (a) the general mineral composition, and (b) distinct twinning structure in a plagioclase crystal.

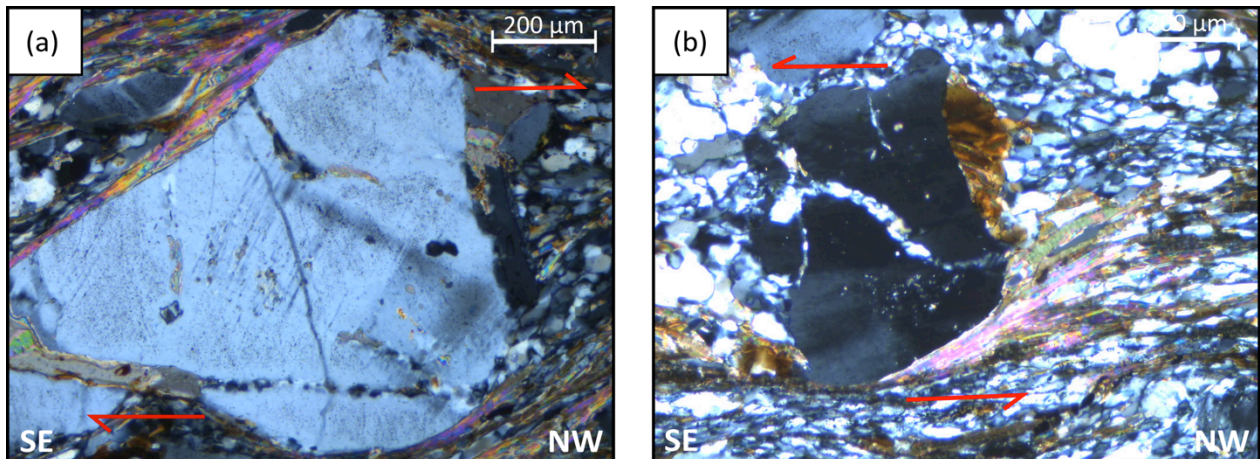


Fig. 4.27 – Two deformation stages can be identified within the mylonitic lens (sample 002): (a) Top-to-the-NW, with muscovite precipitated in the pressure shadow, and (b) top-to-the-SE with biotite precipitated in the pressure shadow.

The Jotun nappe complex

The sample collected from the Jotun nappe complex is dominated by a matrix of abundant epidote, zoisite and biotite (Fig. 4.28). Rounded to sub-rounded feldspar crystals with an altered appearance are present within this matrix. The large feldspar crystals consist mainly of plagioclase, with fluid inclusion trails and distinct twinning-structure (Fig. 4.29a). Asymmetric crystals with associated pressure shadows indicate top-to-the-NW sense of movement.

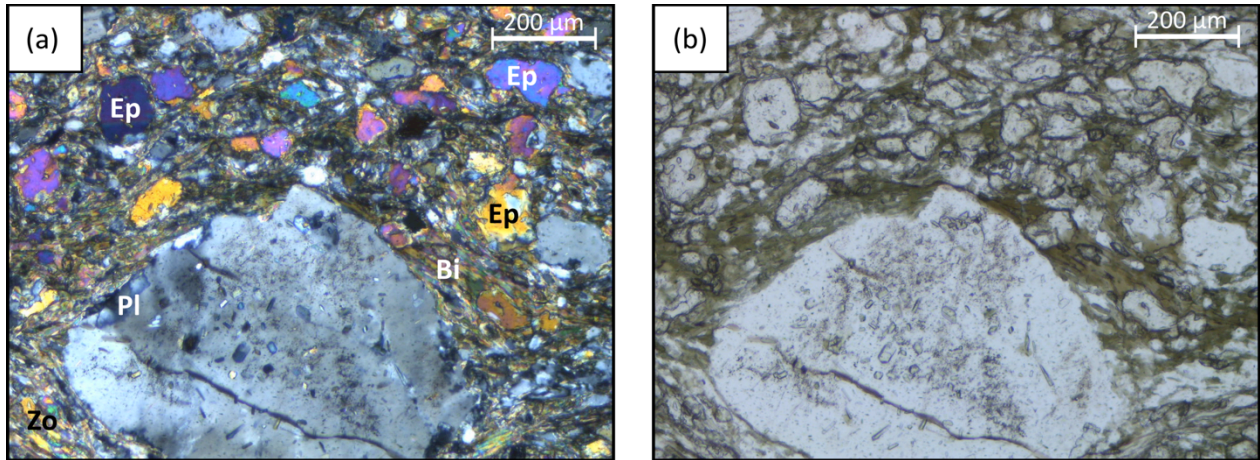


Fig. 4.28 – Thin section photographs of sample 063 showing the domain of epidote, zoisite and large feldspar crystals in (a) cross-polarised light and (b) plane-polarised light. (b) Biotite (green) is the dominant mica-mineral within the sample.

The sample has a less distinct foliation than the samples from the other units, with mineral accretion in irregular domains rather than layers. Another compositional domain consists of mainly recrystallised quartz and muscovite. Top-to-the-NW shear bands are present within this domain (Fig. 4.29b).

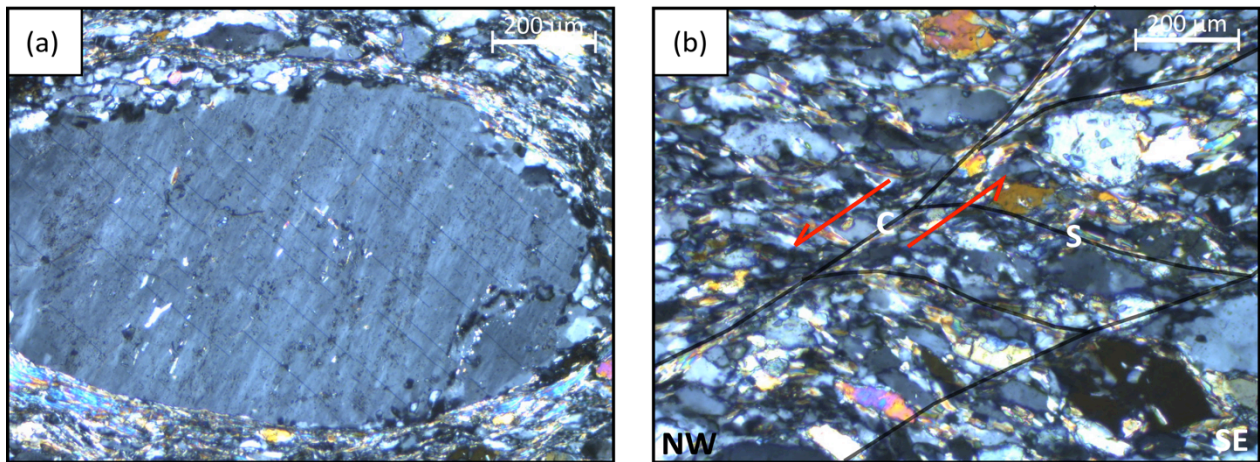


Fig. 4.29 – Thin sections photographs of sample 063 showing (a) a rounded crystal of plagioclase with twinning-structure and fluid inclusion trails, and (b) top-to-the-NW shear bands (S-C' fabric).

Kinematic indicators

Table 7 provides an overview of micro-scale kinematic indicators identified during thin section analyses. The majority of kinematic indicators point towards top-to-the-NW sense of movement, but some indicators of top-to-the-SE sense of movement were found within the Fortun-Vang nappe complex.

Table 7 – Overview of micro-scale kinematic indicators identified during thin section analyses.

Unit	Rock type	Kinematic indicators	Sense of movement
Proterozoic basement	Migmatitic gneiss	- Asymmetric crystals - Shear bands	Top-to-the-NW
Fortun-Vang nappe complex	Phyllite and mica schist	- Shape-preferred orientation of ribbons - Shear bands	Top-to-the-NW, Top-to-the-SE
Fortun-Vang nappe complex	Mylonitic lens	- Pressure shadows - Shear bands	Top-to-the-NW, Top-to-the-SE
Jotun nappe complex	Mangeritic gneiss	- Pressure shadows - Shear bands	Top-to-the-NW

4.3 Oxygen stable isotope ($\delta^{18}\text{O}$) analyses

Various generations of quartz veins were observed during fieldwork, with a relative chronological order of formation. The oldest generation I quartz veins are highly deformed and lie parallel to the main foliation in the phyllite (Fig. 4.30ab). Top-to-the-NW shear bands cut across these veins. Generation II quartz veins are generally less deformed though sub-parallel to the main foliation (Fig. 4.30cd).

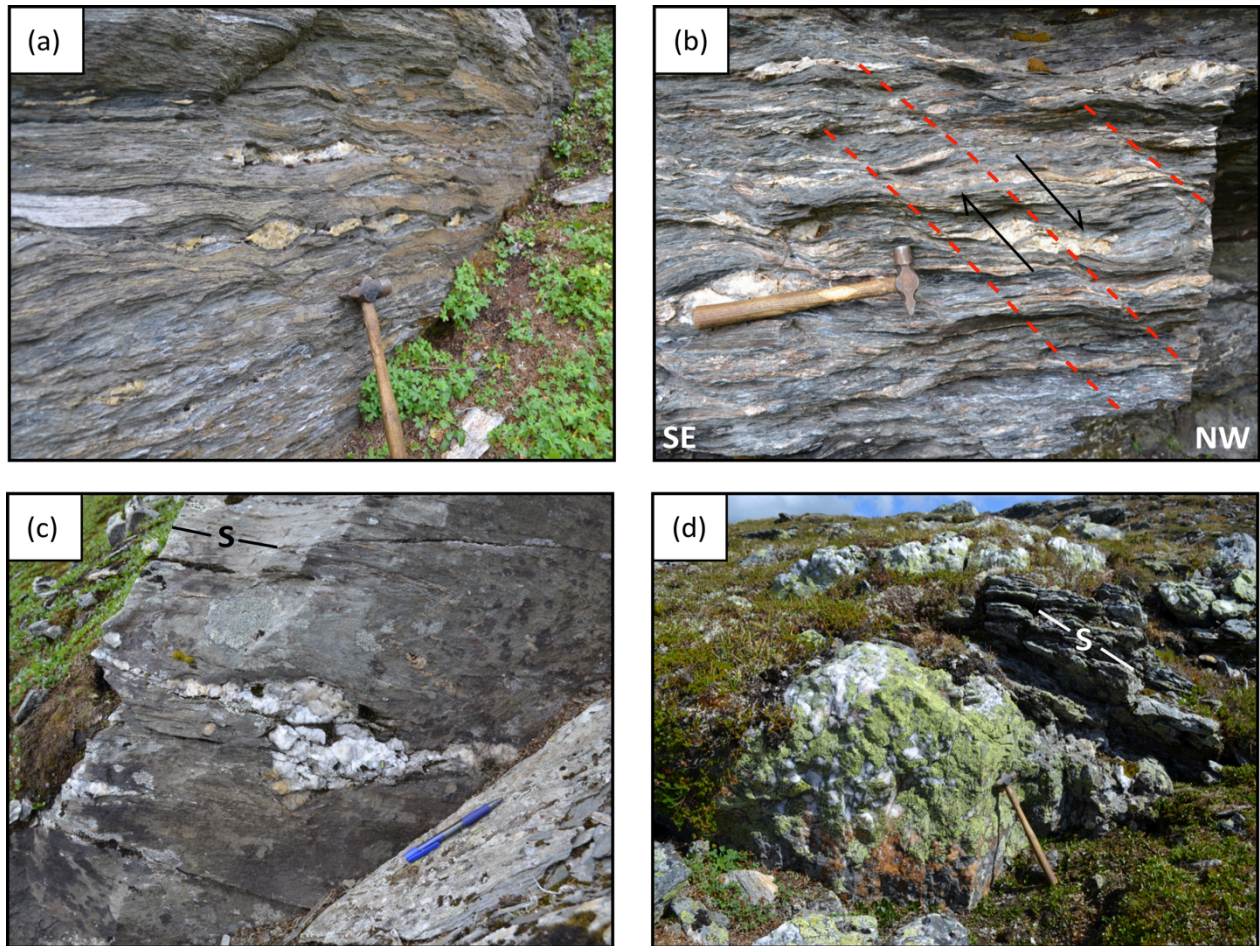


Fig. 4.30 – (a-b) Generation I quartz veins and (c-d) generation II quartz veins. Note that (a) generation I quartz veins are deformed parallel to the main foliation, with (b) top-to-the-NW shear bands cutting across these veins. (c) Generation II quartz veins are generally less deformed, though (d) sub-parallel to the main foliation (S).

Generation III quartz veins represent the youngest vein generation, and cut across ductile deformation features in the phyllite. These veins generally follow N-S striking brittle fault zones (Fig. 4.31).

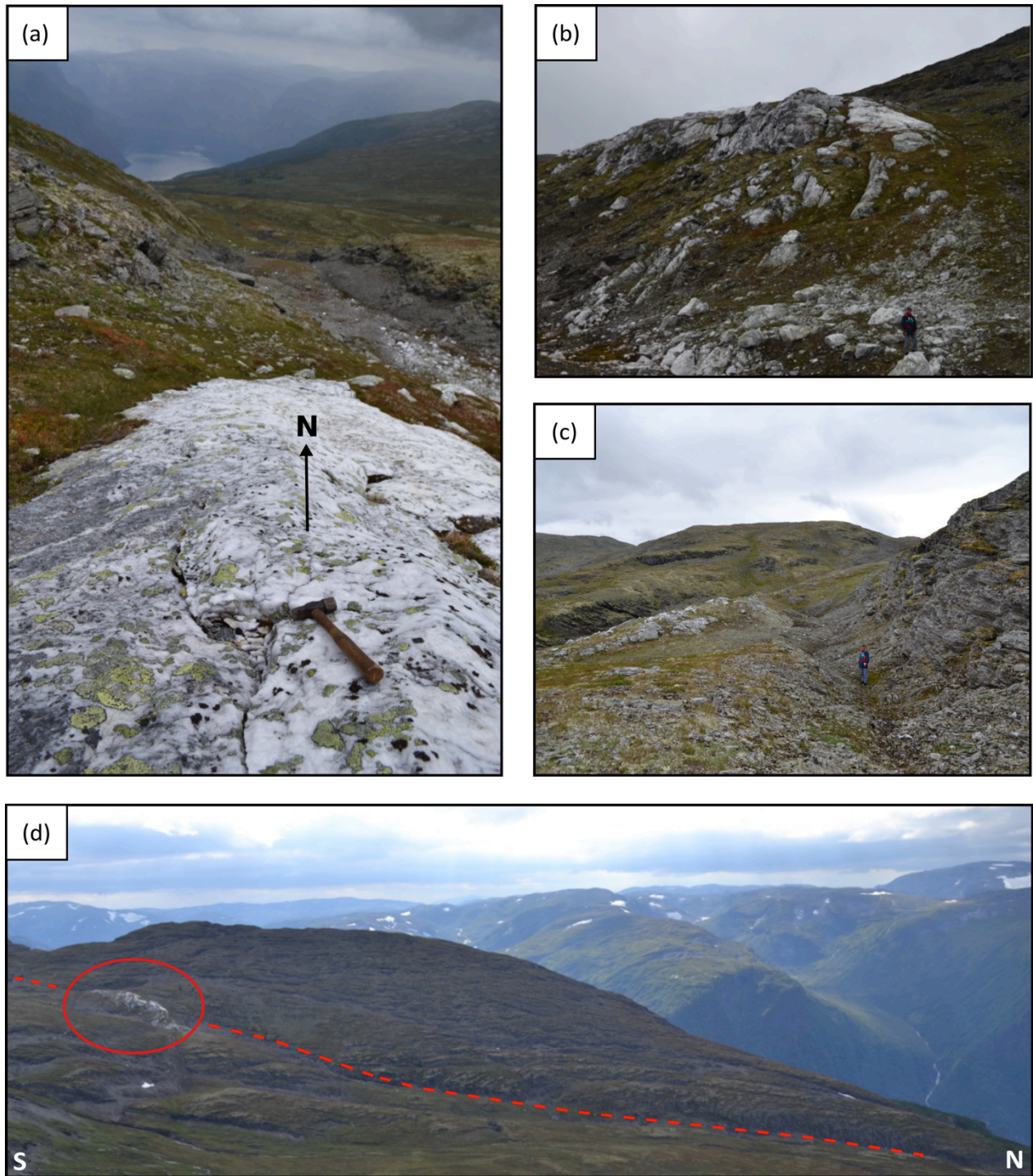


Fig. 4.31 – (a-d) Generation III quartz veins. All photographs are taken from the same approx. 20m wide and 100m long quartz vein that follows a brittle fault zone striking N-S.

Table 8 – $\delta^{18}\text{O}$ analyses of various generations of quartz veins within the Fortun-Vang nappe complex. The standard deviation of the values is 0.5‰

Sample no.	Generation	$\delta^{18}\text{O}$ (raw)	$\delta^{18}\text{O}$ (corrected)
049-1	I	16,017	16,3
049-2	I	16,506	16,8
035	II	15,701	16,0
037	II or III	15,943	16,2
020-1	III	16,102	16,4
020-2	III	16,226	16,5

$\delta^{18}\text{O}$ analyses of various quartz veins in the Fortun-Vang nappe complex (Fig. 3.1) indicate that there are no significant differences between the different generations (Tab. 8). The narrow range of $\delta^{18}\text{O}$ values may suggest that the quartz veins have been buffered by the phyllitic host rock (Mullis et al., 1994). In order to say something certain about this, one should also have $\delta^{18}\text{O}$ data from the host rock. Similar $\delta^{18}\text{O}$ values between the quartz veins and the host rock generally indicate that fluid/rock ratios were low, and that the quartz veins were precipitated by locally derived fluids in a lithostatic regime (Sharp et al., 2005). These metamorphic fluids may have derived from dehydration of underlying and surrounding meta-sediments (Mullis et al., 1994).

Mullis et al. (1994) suggests that retrograde metamorphism is characterised by decreasing contents of volatiles and increasing $\delta^{18}\text{O}$ values of quartz veins. Even though there are no significant differences between the different generations, a slight increase in $\delta^{18}\text{O}$ values can be observed between generation II and III quartz veins. Tectonic activity may involve episodic pressure drops, which promote fluid unmixing and channelised flows of supersaturated fluids (Sharp et al., 2005). Such channelised flows are typical under semi-brittle to brittle deformation conditions, and may lead to the formation of large-scale quartz veins (Fig. 4.31).

5 Discussion

In this chapter several aspects of the results will be discussed in terms of past and present deformation mechanisms. Firstly, observed micro- to macro-scale kinematic indicators will be related to different Caledonian deformation stages, and discussed with regards to the structural evolution of the area. Secondly, inferred cross-sections of the mountain slope will be further investigated, to identify pre-existing geological structures that may affect rock slope stability. Thirdly, the methodology will be discussed with regards to uncertainty in structural geology and geological modelling.

5.1 Structural evolution and relation to the Caledonian orogeny

Observed micro- to macro-scale kinematic indicators from this study and previous studies (Fossen & Hurich, 2005) mainly point towards top-to-the-NW sense of movement (Tab. 5; Tab. 7), which can be related to the Caledonian collapse and backsliding of the orogenic wedge. However, some kinematic indicators point towards top-to-the-SE sense of movement (Tab. 5; Tab. 7), which can be related to the Caledonian nappe-emplacement. Alternatively, the presence of top-to-the-SE kinematic indicators can be explained by a flattening component (pure shear) during the orogenic collapse, in addition to a simple shear component (Fossen & Gabrielsen, 2005). A relative chronological order of formation can be identified based on overprinting relationships of structures, and put into context with the three main Caledonian deformation stages described by Fossen and Hurich (2005):

(1) Ductile top-to-the-SE contractional deformation of the Caledonian nappe emplacement:

- Penetrative foliation, generation I quartz veins and top-to-the-SE kinematic indicators (Fig. 5.1a).

(2) Ductile to semi-brittle top-to-the-NW extensional deformation of the Caledonian collapse:

- Stretching lineations, isoclinal (F_1) folds and generation II quartz veins (Fig. 5.1b).

- Open (F_2) folds with crenulation and associated large-scale folding of the foliation (Fig. 5.1c₁).

- Ductile to semi-brittle normal and reverse shear bands (Fig. 5.1c₂).

- Semi-brittle to brittle normal faults and associated large-scale generation III quartz veins (Fig. 5.1d).

(3) Post-Caledonian brittle deformation concentrated along N-S striking faults:

- Brittle steep to sub-vertical joint sets reactivated during Permo-Triassic and late Jurassic rifting events (Torsvik et al., 1997; Valle et al., 2002) (Fig. 5.1e).

NW

SE

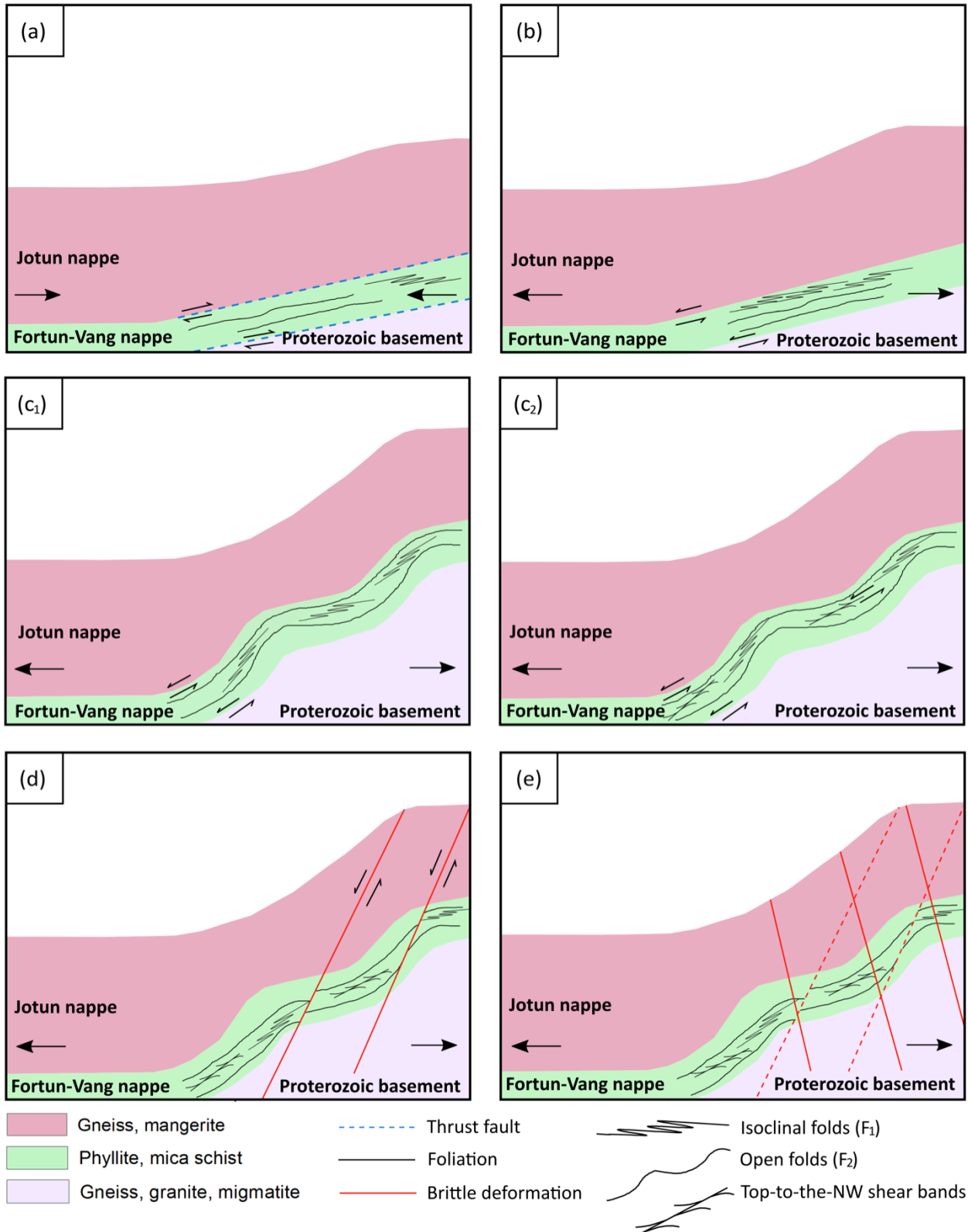


Fig 5.1 – Simplified schematic illustration showing the structural evolution of the Stampa-area with regards to Caledonian and post-Caledonian ductile, semi-brittle and brittle deformation features.

5.2 Implications for rock slope stability

Destabilisation of the mountain slope is closely linked to the abundance and orientation of pre-existing ductile, semi-brittle and brittle structures that characterise the bedrock of Western Norway (Saintot et al., 2011). The bedrock of Western Norway was exposed to large-scale tectonic weakening during several Caledonian and post-Caledonian deformation stages (Fossen & Hurich, 2005). Hence, ongoing destabilisation is concentrated along weak zones delimited by these inherited structures (Saintot et al., 2011). Structures inferred to delimit such weak zones include foliation, cleavage, folds, shear zones, faults, joint sets and lithological discontinuities (Prucha, 1992). The different structures relevant for the overall stability of the mountain slope and selected failure-scenarios (Fig. 5.2; Fig. 5.3) will be discussed in this chapter.

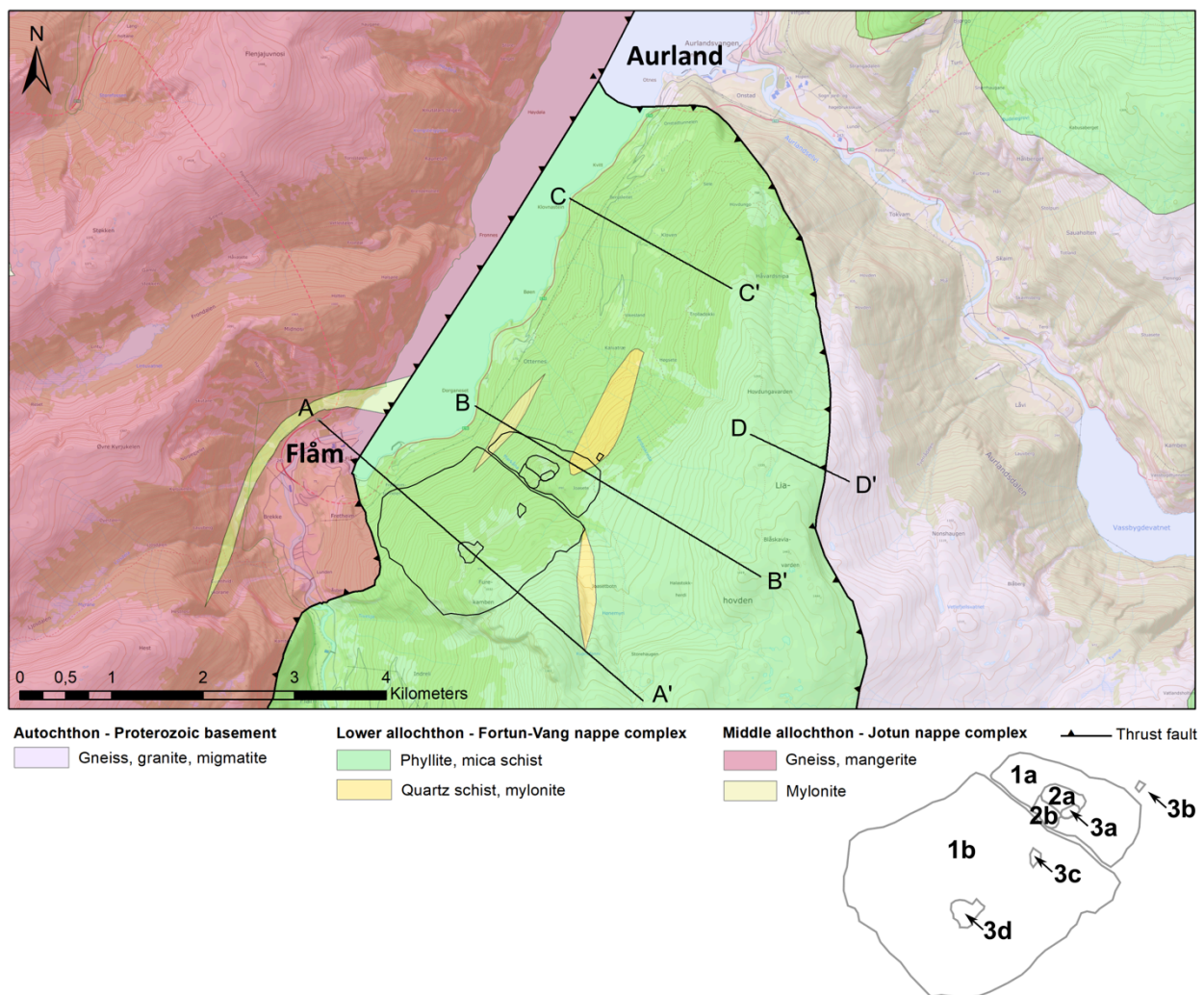


Fig. 5.2 – Bedrock geology map of the inner Aurlandsfjord showing the trace of geological cross-sections and the extent of potential failure-scenarios. This study focuses on the overall stability of the mountain slope, along with scenario 1a, 2a and 3a by Joasete. These scenarios falls within profile B-B', and represent the highest movement rates.

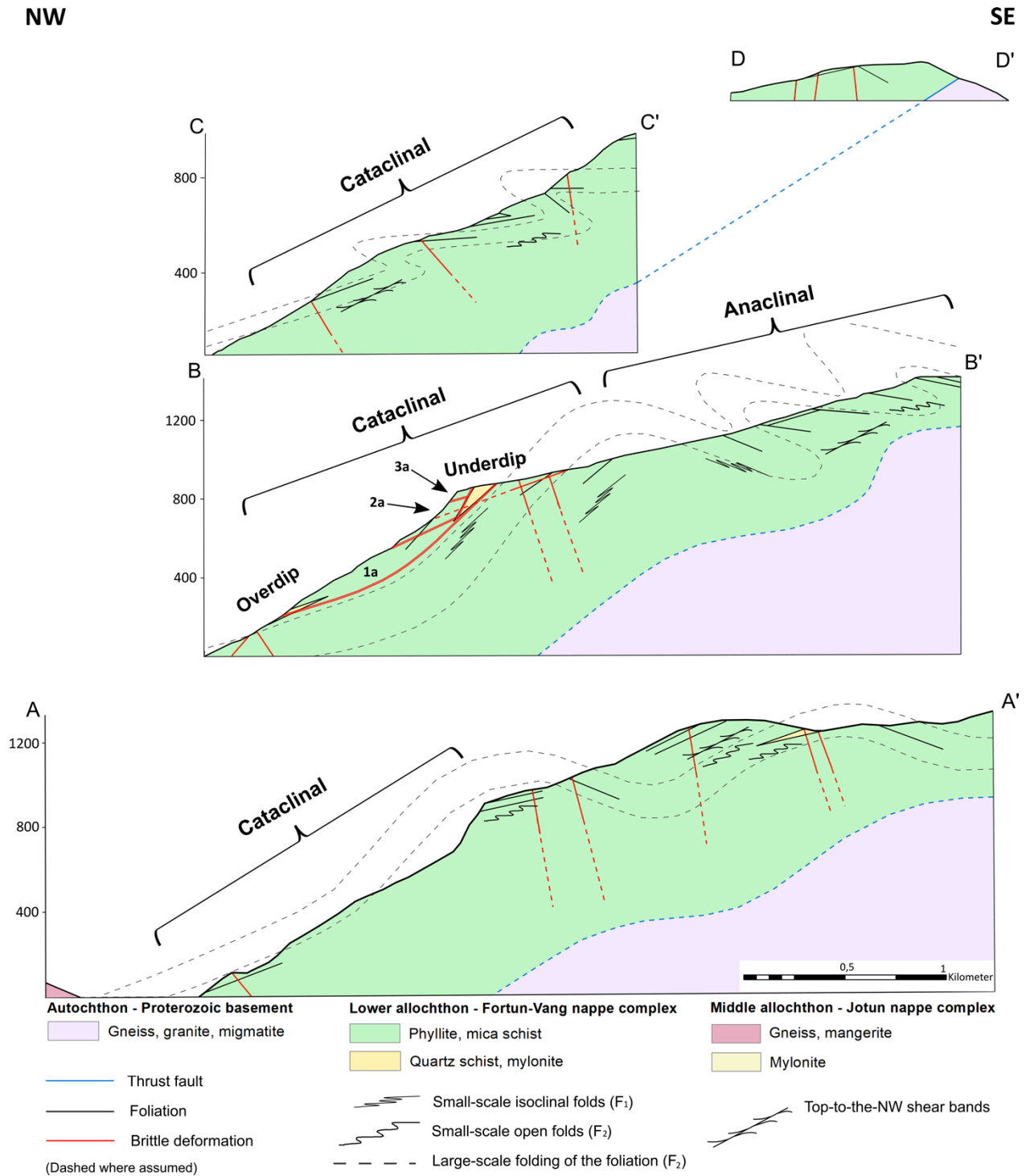


Fig 5.3 – Schematic geological cross-sections showing the large-scale lithological and structural style of the Stampa-area, together with the approximate location of selected failure-scenarios and rocks slope classifications.

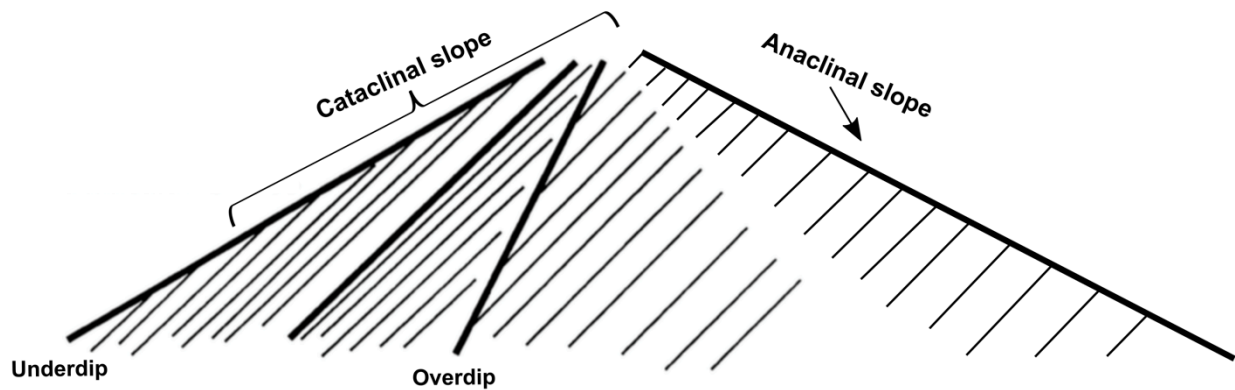


Fig 5.4 – Rock slope classifications from Cruden (2000), based on terminology originally introduced by Powell (1875). Thick lines represent the slope and thin lines represent the foliation.

Lithological control on rock slope stability

Deep-seated gravitational slope deformations (DGSDs) frequently occur in foliated metamorphic rocks such as schist, phyllite and paragneiss (Strauhal et al., 2017). DGSDs in incompetent, mica-rich rocks are characterised by continuous, low-velocity creep due to the inherent low shear strength (Saintot et al., 2011). Several case studies indicate that slope displacement is mainly localised at basal and internal shear zones, formed by ongoing strain localisation and cataclasis of the bedrock (Strauhal et al., 2017). According to Strauhal et al. (2017) these shear zones range from a few centimeters to several meters in thickness, and occur along inherited weak lithological or structural zones. In contrast, competent rocks are characterised by episodic, high-velocity brittle deformation (Prager et al., 2009).

Lithology is regarded an important factor affecting rock slope stability, and several studies point towards reactivation of sliding planes along lithological discontinuities. Saintot et al. (2011) present the lithological and structural framework of multiple rock slope instabilities across Western Norway. The unstable mountain slope by Vollan, Sunndalen Valley, has similar characteristics to the unstable mountain slope by Stampa. The unstable mountain slope is located within a unit of phyllite and mica schist, with slope displacement accommodated by low-velocity creep along the lithological contact to the underlying quartzite (Saintot et al., 2011).

Within the Fortun-Vang nappe complex by Stampa, mylonitic lenses developed in competent quartzitic schist are embedded in the less competent phyllite and mica schist (Fig. 5.3). Such competence contrasts may decrease rock slope stability through reactivation of sliding planes along lithological discontinuities. Semi-brittle creep may be ongoing in the less competent phyllite and mica schist, while brittle deformation may be dominating the more competent mylonitic lenses. Both deformation mechanisms may evolve into sudden failures including rock falls, rockslides and rock avalanches (Prager et al., 2009).

The largest mylonitic lens by Joasete (Fig. 5.3) extends into the area that is currently moving by approx. 10 mm/year. It is likely that the lithological discontinuity between this lens and the surrounding phyllite has implications for the size and movement of unstable blocks (scenario 3a) at the frontal cliff (Fig. 5.3). This lens seems to be the main back-bounding discontinuity that contributes to the detachment of scenario 2a (Fig. 5.3). The detachment of scenario 1a is largely controlled by back-bounding open fractures striking NNE-SSW (Blikra & Berg, 2013). Additionally, scenario 1a seems to be delimited by the two connected mylonitic lenses in profile B-B' (Fig. 5.3).

Implications of ductile structures on rock slope stability

In some areas of the unstable mountain slope by Stampa, ductile and semi-brittle structures are oriented favourable to promote DGSDs, which in turn may lead to sudden rock slope failures (Prager et al., 2009). The foliation within the lower, unstable part of the mountain slope is generally dipping towards the fjord (Fig. 5.3). Accordingly, this part of the slope is classified as a cataclinal slope with alternating overdip and underdip due to large-scale folding of the foliation (Fig. 5.3; Fig. 5.4). The upper, more stable part of the slope is classified as an anaclinal slope (Fig. 5.3; Fig. 5.4). Together with fjord-dipping ductile shear bands and semi-brittle faults, foliation planes are likely to be reactivated as sliding planes.

Large-scale folding of the foliation may increase the probability of pre-existing structures being reactivated as sliding planes due to gravitational forces. This happens through (1) weakening of minerals by stretching and flattening, (2) strain localisation along fold axes or axial planes and (3) favourable orientation of sliding planes with respect to the slope (Saintot et al., 2011). At the same time, large-scale folding of the foliation may decrease the probability of slope displacement, through unfavourable orientation of sliding planes. Additionally, rheological contrasts between folded and unfolded units may have similar effects on rock slope stability as lithological contrasts (Saintot et al., 2011).

The Stampa-area is characterised by polyphase folding with interferences of at least two main fold generations. Gentle to open (F_2) folds, which are commonly described throughout Sogn og Fjordane County (Saintot et al., 2011), are overprinting older isoclinal (F_1) folds. These small-scale isoclinal folds are fjord-dipping in the lower, unstable part of the mountain slope (Fig. 5.3), which may promote sliding along axial planes (Saintot et al., 2011). Large-scale open folds are generally not oriented favourable to promote sliding along fold axes or axial planes, at least not in the upper part of the mountain slope where fold axes show indistinct patterns and axial planes are dipping away from the fjord (Fig. 5.3). In the lower, unstable part of the mountain slope sliding planes may develop along fjord-dipping foliation planes in fold limbs (Fig. 5.3).

Implications of brittle structures on rock slope stability

Brittle structures that are oriented favourable to promote slope displacement in the Stampa-area include: (1) Fracture-surfaces developed parallel to the fjord-dipping foliation and (2) steep to sub-vertical joint sets developed perpendicular to the main foliation (Fig. 5.3). The relative orientation of these joint sets promotes cubic break-up of the rock mass and planar sliding of the cubes. The abundance of brittle faults and joint sets generally have a destabilising effect on the mountain slope, through increased mechanical and chemical weathering (Saintot et al., 2011). Field observations from this study and previous studies (Blikra & Berg, 2013; Böhme et al., 2013) indicate that these inherited discontinuities coincide with large-scale gravitational structures such as back-bounding surface depressions, graben structures and open fractures. It is especially regional faults and joint sets striking N-S to NNE-SSW throughout Sogn og Fjordane County (Saintot et al., 2011) that contribute to the detachment of large blocks (scenario 3a) and segments (scenario 2a and 1a) (Fig. 5.3).

To summarise, the susceptibility to future failures increase with the abundance and orientation of reactivated geological structures (Saintot et al., 2011). Table 9 summarises structural and lithological features inferred to delimit the unstable area(s) at Stampa (Fig. 5.3). One by one, these pre-existing structures decrease rock slope stability, and taken together they dramatically enhance destabilisation. The size and extent of future failures is largely dependent on the spacing between these structures (Saintot et al., 2011).

Table 9 – Observed structural and lithological features that control the characteristics of the unstable mountain slope by Stampa, Aurland.

Type	Description	Orientation (Dip-direction)
Foliation	- Variably dipping towards the fjord	WSW
Folds	- Axial planes of isoclinal (F_1) folds dipping towards the fjord - Rheological contrasts between folded and less folded units	NW
Shear bands	- Moderately dipping towards the fjord	NW
Faults	- Steeply dipping towards the fjord	W
Joint sets	- Steeply to sub-vertically dipping away from the fjord	ESE
Lithological discontinuities	- Competence contrasts within the Fortun-Vang nappe complex - Lithological contacts between the three main geological units	WSW

Failure mechanisms

Several structural and lithological features (Tab. 9) control the characteristics of the unstable mountain slope by Stampa with regards to geometry, failure mechanisms and run-out scenarios (Saintot et al., 2011). Ongoing deformation of the mountain slope and future failures may involve a planar, wedge, toppling, rotational or compound component (Stead & Wolter, 2015). Stampa is regarded a complex rock slope instability with multiple deep-seated failure mechanisms including (1) toppling, (2) subsiding bilinear wedge and (3) planar sliding along the foliation (Fig. 5.5).

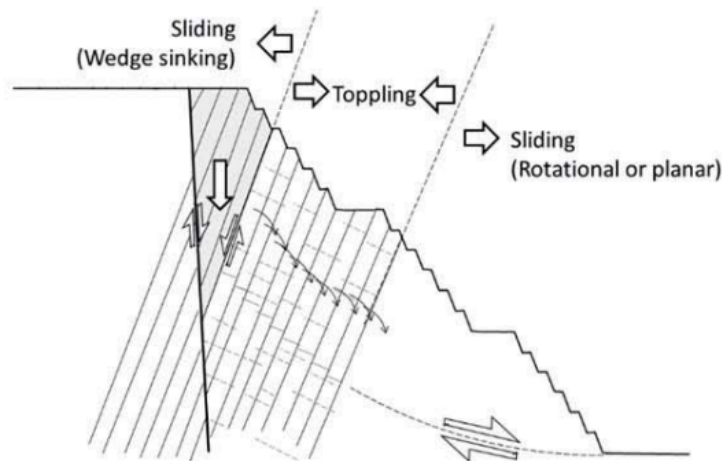


Fig 5.5 – Schematic illustration by Alejano (2018) showing the three main failure mechanisms at Stampa as suggested by Böhme et al. (2013).

Results from this study suggest a similar model, with three main failure mechanisms: (1) Toppling, (2) rotational sliding and (3) planar sliding along the foliation (Fig. 5.6). Toppling is likely to occur on underdip slopes at the edge of the frontal cliff (Fig. 5.6) and is largely controlled by the steepness of the slope and vertical to sub-vertical joint sets (Cruden & Hu, 1996). Planar sliding is likely to occur on overdip slopes at the toe of the mountain slope where the foliation is reactivated as a basal sliding plane and perpendicular joint sets contribute to the detachment of coherent rock masses (Fig. 5.6). Rotational sliding generally dominates deep-seated gravitational slope deformations (DGSDs) across the full extent of the unstable area(s) (Fig. 5.6). Large-scale folding of the foliation together with lithological discontinuities add complexity to the structural style of the mountain slope and suggested failure mechanisms (Saintot et al., 2011). The combination of these failure mechanisms classifies the unstable mountain slope by Stampa as a complex field with listric geometry (Braathen et al., 2004).

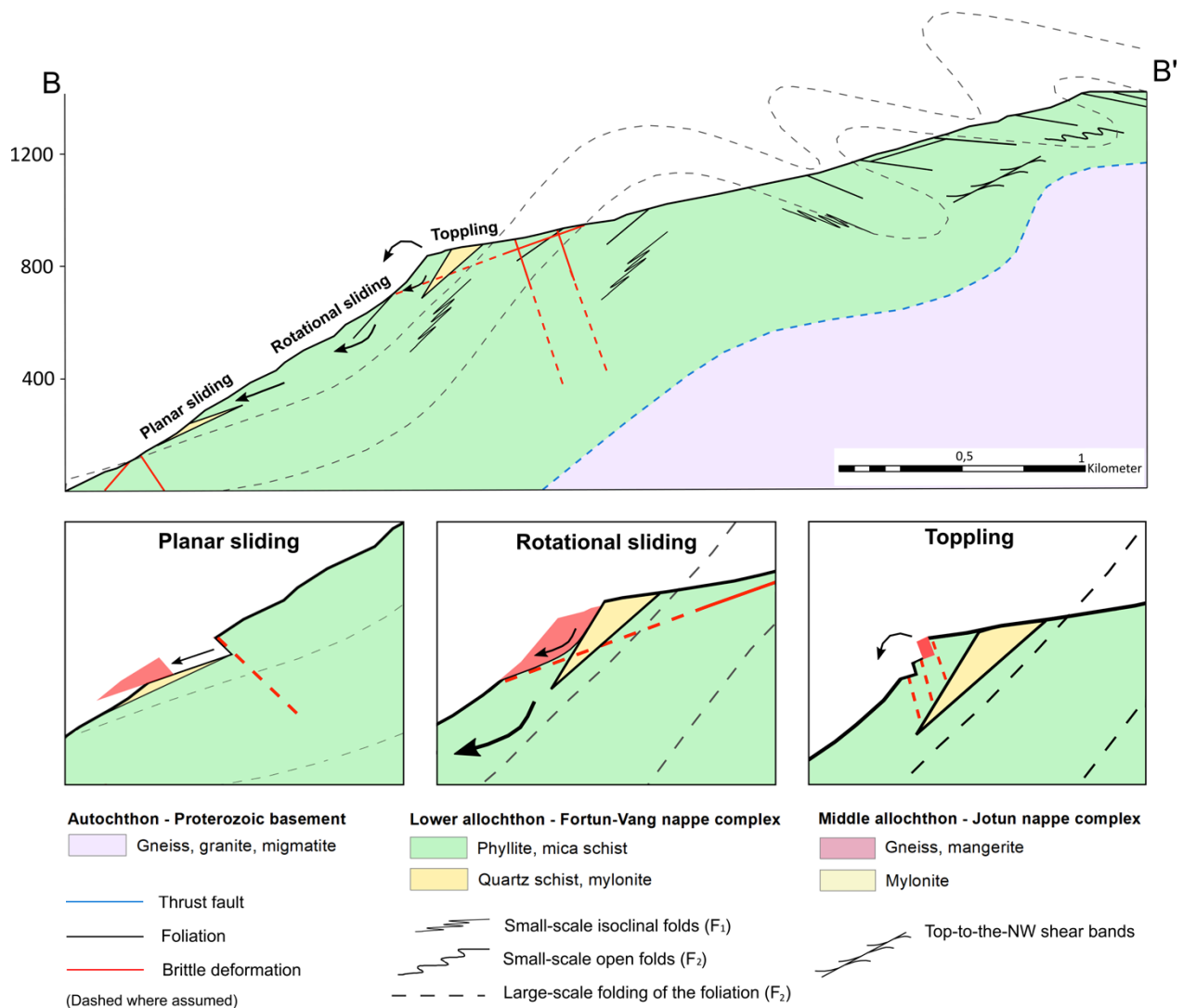


Fig 5.6 – Schematic illustration showing the three main failure mechanisms at Stampa suggested in this study.

5.3 Uncertainty in structural geology and geological modelling ¹

A geological model, or a geological profile, is a representation of the subsurface made with limited resolution and spatial distribution of field data. Geological models can only be constructed with the help of structural geology, and can be used as a tool to assess rock slope instabilities. The construction of a model is based on interpretations of geological outcrops, which may be sparse in the investigation area. Borehole- or geophysical data may be used to supplement field observations, but there will still be an inherent uncertainty connected to the interpretation process (NGU, 2017).

¹ This section (Ch. 5.3) is taken from an essay I wrote during a previous course at the Western Norway University of Applied Sciences, and is included in the discussion because it is important to be aware of uncertainties related to own field investigations.

Geological research follows established geological methods and natural laws, and uncertainty is mainly associated with objective errors connected to inaccurate measurements or unreliable methods (Bond, 2015). These errors are negligible and can be carefully ignored given a big enough sample (Bond et al., 2011). Objective uncertainty can be reduced 'easily' with the use of error bounds, technological improvements and further obtained knowledge (Bond, 2015).

Subjective uncertainty, or interpretation uncertainty, can be described as uncertainty connected to 'intuitive' interpretations of geological data. Reducing subjective uncertainty is considered to be a more complicated task. An underlying reason for this may be that subjective interpretations of data are an inherent part of the field, and considered the core strength of an experienced geoscientist (Bond, 2015). Geological questions will not always have a straightforward 'right' answer, and geoscientists need to use both their knowledge and intuition to assess such questions. A limitation of this skill is that human biases can affect the interpretation process (Bond et al., 2011). Early work on human biases by Chadwick (1975) suggests that geoscientists tend to see what they are expecting to see instead of what they actually see.

Results from different studies show that geological reasoning and rules may reduce subjective uncertainty (Bond, 2015). With regards to geology, Frodeman (1995) recognises that (1) uncertainty is the norm rather than a special case, and (2) geological reasoning is seen as a unique and desirable skill that will aid solutions to 21st century problems. By recognising this inherent uncertainty and adopting interpretation skills from experienced geoscientists, human biases can be minimised and a higher degree of accuracy achieved (Bond et al., 2007).

It is important to shed light on both objective and subjective uncertainty when conducting a study fully based on fieldwork and subsequent data analyses. It is apparent that geological research involves different types of uncertainty at different stages of the research process. This is called cumulative uncertainty, and involves uncertainty from the original fieldwork and data collection process through to the following interpretation process and construction of a geological model (Bond, 2015). Accordingly, this study may be affected by minor inaccuracies and uncertainties, as the results are based on my own subjective interpretations of collected field data.

6 Conclusion

In this study the regional structural geological framework of the unstable mountain slope by Stampa, Aurland has been investigated. Field observations and associated kinematic analyses indicate that most ductile and semi-brittle deformation features can be related to top-to-the-NW extensional deformation of the Caledonian collapse and backsliding of the orogenic wedge. However, some deformation features can be related to top-to-the-SE contractional deformation of the Caledonian nappe-emplacment. $\delta^{18}\text{O}$ analyses indicate that various generations of quartz veins within the Fortun-Vang nappe complex were precipitated by locally derived fluids in a lithostatic regime.

The Stampa-area is characterised by the abundance of ductile, semi-brittle and brittle deformation features, which define the large-scale structural style of the area. Field observations and associated structural analyses indicate that several lithological and structural features affect the overall stability of the mountain slope: (1) Fjord-dipping ductile and semi-brittle structures, (2) folds and interference folds, (3) regional brittle faults and joint sets and (4) lithological discontinuities. These features delimit the unstable area(s) at Stampa and may directly be reactivated as sliding planes or backscarps. Accordingly, the abundance and orientation of pre-existing geological structures increase the susceptibility to future failures. The unstable part of the mountain slope can be classified as a cataclinal slope with three main failure mechanisms: (1) Toppling, (2) rotational sliding and (3) planar sliding along the foliation. Toppling of unstable blocks is likely to occur on underdip slopes at the edge of the frontal cliff, whereas planar sliding along the foliation is likely to occur on overdip slopes at the toe of the mountain slope. Rotational sliding generally dominates deep-seated gravitational slope deformations (DGSDs) across the full extent of the unstable area(s).

This study emphasises the importance of structural geology with regards to assessments of rock slope instabilities. Structural mapping is important because every rock slope has its unique structural framework with different lithological and structural features affecting rock slope stability. Complete and thorough assessments of rock slope instabilities may lead to the installation of early warning systems at susceptible sites and thereby decrease the risk of damage on human lives, properties and infrastructure. This study makes a small contribution to face one of the major environmental challenges of our times. Field data and results from this study may be used for further slope stability analyses. Such analyses become increasingly important with projections of increased rockslide activity due to climatic changes.

7 References

- Alejano, L. (2018). *Complex rock slope failure mechanisms involving toppling*. Paper presented at the Slope Stability Symposium 2018, Seville, Spain.
- Andersen, T. B., Torsvik, T. H., Eide, E. A., Osmundsen, P. T., & Faleide, J. I. (1999). Permian and Mesozoic extensional faulting within the Caledonides of central south Norway. *Journal of the Geological Society*, *156*(6), 1073-1080.
- Blikra, L. H., & Berg, H. (2013). De ustabile fjellsidene i Stampa - Flåm, Aurland kommune: Sammenstilling, scenario, risiko og anbefalinger. *NVE Rapport nr. 30 - 2013*.
- Blikra, L. H., Longva, O., Braathen, A., Dehls, J. F., Stalsberg, K., & Anda, E. (2006). Rock slope failures in norwegian fjord areas: Examples, spatial distribution and temporal pattern. *Landslides*, *49*, 475-496.
- Bond, C. E. (2015). Uncertainty in structural interpretation: Lessons to be learnt. *Journal of Structural Geology*, *74*, 185-200.
- Bond, C. E., Gibbs, A. D., Shipton, Z. K., & Jones, S. (2007). What do you think this is? "Conceptual uncertainty" in geoscience interpretation. *GSA today*, *17*(11), 4-10.
- Bond, C. E., Philo, C., & Shipton, Z. K. (2011). When There Isn't a Right Answer: Interpretation and Reasoning, Key Skills for Twenty-First Century Geoscience. *International Journal of Science Education*, *33*(5), 629-652.
- Borgatti, L., & Soldati, M. (2010). Landslides as a geomorphological proxy for climate change: A record from the Dolomites (northern Italy). *Geomorphology*, *120*(1), 56-64.
- Bryhni, I. (Cartographer). (1977). 1:50 000 bedrock geology map sheet, Aurland.
- Bryhni, I., Brastad, K., & Jacobsen, V. (1983). Subdivision of the Jotun nappe complex between Aurlandsfjorden and Nærøyfjorden, south Norway. *Norges geologiske undersøkelse*, *380*, 23-33.
- Braathen, A., Blikra, L. H., Berg, S. S., & Karlsen, F. (2004). Rock-slope failures in Norway; type, geometry, deformation mechanisms and stability. *Norsk geologisk tidsskrift*, *84*(1), 67-88.
- Böhme, M., Hermanns, R. L., Oppikofer, T., Fischer, L., Bunkholt, H. S. S., Eiken, T., . . . Nilsen, B. (2013). Analyzing complex rock slope deformation at Stampa, western Norway, by integrating geomorphology, kinematics and numerical modeling. *Engineering Geology*, *154*, 116-130.
- Chadwick, P. (1975). A psychological analysis of observation in geology. *Nature*, *256*, 570-573.
- Clayton, R. N., & Mayeda, T. K. (1963). The use of bromine pentafluoride in the extraction of oxygen from oxides and silicates for isotopic analysis. *Geochimica et cosmochimica Acta*, *27*(1), 43-52.
- Crawford, M., & Hollister, L. (1986). Metamorphic fluids: The evidence from fluid inclusions. In J. Walther & B. Wood (Eds.), *Fluid—Rock interactions during metamorphism* (Vol. 5, pp. 1-35). New York: Springer.
- Cruden, D., & Hu, X. (1996). Hazardous modes of rock slope movement in the Canadian Rockies. *Environmental & Engineering Geoscience*, *2*(4), 507-516.
- Cruden, D. M. (2000). Some forms of mountain peaks in the Canadian Rockies controlled by their rock structure. *Quaternary International*, *68-71*, 59-65.
- Cruden, D. M., & Varnes, D. J. (1996). Landslide types and processes. In A. K. Turner & R. L. Schuster (Eds.), *Landslides: Investigation and Mitigation* (Vol. 247, pp. 36-75). Washington D.C: National Research Council, Special Report.
- Domaas, U., & Glimsdal, S. (2009). Beregning og flodbølger for tre potensielle fjellskred fra Stampa. *Norwegian Geotechnical Institute*, 1-49.
- Fischer, L., Amann, F., Moore, J. R., & Huggel, C. (2010). Assessment of periglacial slope stability for the 1988 Tschierwa rock avalanche (Piz Morteratsch, Switzerland). *Engineering Geology*, *116*(1), 32-43.

- Fossen, H., & Dunlap, W. J. (1998). Timing and kinematics of Caledonian thrusting and extensional collapse, southern Norway: evidence from 40Ar/ 39Ar thermochronology. *Journal of Structural Geology*, 20(6), 765-781.
- Fossen, H., & Gabrielsen, R. H. (2005). *Strukturgeologi*. Bergen: Fagbokforlaget.
- Fossen, H., Gabrielsen, R. H., Faleide, J. I., & Hurich, C. A. (2014). Crustal stretching in the Scandinavian Caledonides as revealed by deep seismic data. *Geology*, 42(9), 791-794.
- Fossen, H., & Hurich, C. (2005). The Hardangerfjord Shear Zone in SW Norway and the North Sea: a large-scale low-angle shear zone in the Caledonian crust. *Journal of the Geological Society*, 162(4), 675-687.
- Frodeman, R. (1995). Geological reasoning: Geology as an interpretive and historical science. *Geological Society of America Bulletin*, 107(8), 960-968.
- Gee, D. G. (1975). A tectonic model for the central part of the Scandinavian Caledonides. *American Journal of Science*, 275, 468-515.
- Gee, D. G., Fossen, H., Henriksen, N., & Higgins, A. K. (2008). From the Early Paleozoic Platforms of Baltica and Laurentia to the Caledonide Orogen of Scandinavia and Greenland. *Episodes*, 31(1), 44-51.
- Glade, T., & Crozier, M. J. (2005). The nature of landslide hazard impact. In T. Glade, M. G. Anderson, & M. J. Crozier (Eds.), *Landslide Hazard and Risk* (pp. 43-74). Chichester: John Wiley & Sons Ltd.
- Guddal, S., & Løset, O. (2017). I år slo dei fire år gamal besøksrekord. *NRK Sogn og Fjordane*.
- Henriksen, H., & Dale, T. (2018). Groundwater discharge from a rock-slope failure system in phyllitic rocks influencing fjord basin hydrodynamics, Stampa in Aurland, western Norway. *The Norwegian Journal of Geology*, 98(1), 55-77.
- Hermanns, R. L., Schleier, M., Böhme, M., Blikra, L. H., Gosse, J., Ivy-Ochs, S., & Hilger, P. (2017). *Rock-avalanche activity in w and s Norway peaks after the retreat of the scandinavian ice sheet*. Paper presented at the 4th World Landslide Forum, Ljubljana, Slovenia.
- Huggel, C., Clague, J. J., & Korup, O. (2012). Is climate change responsible for changing landslide activity in high mountains? *Earth Surface Processes and Landforms*, 37(1), 77-91.
- Ivy-Ochs, S., Poschinger, A. V., Synal, H. A., & Maisch, M. (2009). Surface exposure dating of the Flims landslide, Graubünden, Switzerland. *Geomorphology*, 103(1), 104-112.
- Jaedicke, C., Solheim, A., Blikra, L. H., Stalsberg, K., Sorteberg, A., Aaheim, A., . . . Mestl, H. (2008). Spatial and temporal variations of Norwegian geohazards in a changing climate, the GeoExtreme Project. *Natural Hazards and Earth System Sciences*, 8(4), 893-904.
- Kristensen, L., & Anda, E. (2016). Bakkebaserte radarmålinger på Børa i Romsdalen og Stampa ved Flåm. *NVE Rapport nr. 84 - 2016*.
- Kristensen, L., & Bergeng, T. (2018). Overvåking av Joasetbergi. *NVE Rapport nr. 48 - 2018*.
- Le Roux, O., Schwartz, S., Gamond, J. F., Jongmans, D., Bourles, D., Braucher, R., . . . Leanni, L. (2009). CRE dating on the head scarp of a major landslide (Séchilienne, French Alps), age constraints on Holocene kinematics. *Earth and Planetary Science Letters*, 280(1), 236-245.
- Mangerud, J., Gyllencreutz, R., Lohne, Ø., & Svendsen, J. I. (2011). Glacial history of Norway. In J. Ehlers, P. L. Gibbard, & P. D. Hughes (Eds.), *Quaternary glaciations: extent and chronology: a closer look* (Vol. 15, pp. 279-298). Amsterdam: Elsevier.
- McCull, S. T. (2012). Paraglacial rock-slope stability. *Geomorphology*, 153-154, 1-16.
- Milnes, A., Wennberg, O., Skår, Ø., & Koestler, A. (1997). Contraction, extension and timing in the South Norwegian Caledonides: the Sognefjord transect. In J. Burg & M. Ford (Eds.), *Orogeny through time* (Vol. 121, pp. 123-148). London: Geological Society, Special Publications.
- Mullis, J., Dubessy, J., Poty, B., & O'Neil, J. (1994). Fluid regimes during late stages of a continental collision: Physical, chemical, and stable isotope measurements of fluid inclusions in fissure quartz from a geotraverse through the Central Alps, Switzerland. *Geochimica et cosmochimica Acta*, 58(10), 2239-2267.


- NGU. (2017). Structural geology Retrieved from www.ngu.no/en/topic/structural-geology
- Norsk klimaservicesenter. (2016). Klimaprofil Sogn og Fjordane - Et kunnskapsgrunnlag for klimatilpasning.
- Powell, J. W. (1875). *Exploration of the Colorado River of the West and its Tributaries*. Washington: Government Printing Office.
- Prager, C., Zangerl, C., & Nagler, T. (2009). Geological controls on slope deformations in the Köfels rockslide area (Tyrol, Austria). *Austrian Journal of Earth Sciences*, 102(2), 4-19.
- Prucha, J. J. (1992). Zone of weakness concept: A review and evaluation. In M. J. Bartholomew, D. W. Hyndman, D. W. Mogk, & R. Mason (Eds.), *Basement Tectonics 8: Characterization and Comparison of Ancient and Mesozoic Continental Margins* (pp. 83-92). Dordrecht: Springer Netherlands.
- Ramberg, I. B., Solli, A., Nordgulen, Ø., Binns, R., & Grogan, P. (2008). *The Making of a land - Geology of Norway*. Trondheim: The Norwegian Geological Association.
- Ravanel, L., & Deline, P. (2011). Climate influence on rockfalls in high-Alpine steep rockwalls: The north side of the Aiguilles de Chamonix (Mont Blanc massif) since the end of the 'Little Ice Age'. *The Holocene*, 21(2), 357-365.
- Roberts, D. (2003). The Scandinavian Caledonides: event chronology, palaeogeographic settings and likely modern analogues. *Tectonophysics*, 365(1), 283-299.
- Saintot, A., Henderson, I., & Derron, M. (2011). Inheritance of ductile and brittle structures in the development of large rock slope instabilities: examples from western Norway. *Geological Society, London, Special Publications*, 351(1), 27-78.
- Sanchez, G., Rolland, Y., Corsini, M., Braucher, R., Bourlès, D., Arnold, M., & Aumaître, G. (2010). Relationships between tectonics, slope instability and climate change: Cosmic ray exposure dating of active faults, landslides and glacial surfaces in the SW Alps. *Geomorphology*, 117(1-2), 1-13.
- Schwartz, G. M., & Todd, J. H. (1941). Comments on retrograde metamorphism. *The Journal of Geology*, 49(2), 177-189.
- Sharp, Z., Masson, H., & Lucchini, R. (2005). Stable isotope geochemistry and formation mechanisms of quartz veins; extreme paleoaltitudes of the Central Alps in the Neogene. *American Journal of Science*, 305(3), 187-219.
- Soldati, M., Corsini, A., & Pasuto, A. (2004). Landslides and climate change in the Italian Dolomites since the Late glacial. *Catena*, 55(2), 141-161.
- Stead, D., & Wolter, A. (2015). A critical review of rock slope failure mechanisms: the importance of structural geology. *Journal of Structural Geology*, 74, 1-23.
- Stoffel, M., & Huggel, C. (2012). Effects of climate change on mass movements in mountain environments. *Progress in Physical Geography*, 36(3), 421-439.
- Strauhal, T., Zangerl, C., Fellin, W., Holzmann, M., Engl, D. A., Brandner, R., . . . Tessadri, R. (2017). Structure, mineralogy and geomechanical properties of shear zones of deep-seated rockslides in metamorphic rocks (Tyrol, Austria). *Rock Mechanics and Rock Engineering*, 50(2), 419-438.
- Torsvik, T. H., Andersen, T. B., Eide, E. A., & Walderhaug, H. J. (1997). The age and tectonic significance of dolerite dykes in western Norway. *Journal of the Geological Society*, 154(6), 961-973.
- Torsvik, T. H., Smethurst, M. A., Meert, J. G., Van Der Voo, R., McKerrow, W. S., Brasier, M. D., . . . Walderhaug, H. J. (1996). Continental break-up and collision in the Neoproterozoic and Palaeozoic — A tale of Baltica and Laurentia. *Earth Science Reviews*, 40(3), 229-258.
- Valle, P., Færseth, R. B., & Fossen, H. (2002). Devonian-Triassic brittle deformation based on dyke geometry and fault kinematics in the Sunnhordland region, SW Norway. *Norwegian Journal of Geology*, 82(1), 3-17.
- Vauchez, A. (1980). Ribbon texture and deformation mechanisms of quartz in a mylonitized granite of Great Kabylia (Algeria). *Tectonophysics*, 67(1-2), 1-12.

8 Appendix

Six structural maps are presented in the appendix. These maps are based on field observations of different lithological units and geological structures, and show representative measurements of ductile, semi-brittle, and brittle deformation features. The legend below applies to all maps listed in table 10, as well as the rest of the study. Additionally, all structural measurements collected during (1) this study and (2) a previous study by Helge Henriksen are provided in table 11.

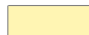
Lithological units

Autochthon - Proterozoic basement


 Gneiss, granite, migmatite

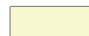
Lower allochthon - Fortun-Vang nappe complex


 Phyllite, mica schist

 Quartz schist, mylonite


Middle allochthon - Jotun nappe complex


 Gneiss, mangerite

 Mylonite

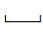
 Thrust fault


Geological structures


 Foliation

 Stretching lineation

 Fold axis

 Axial plane

 Shear band

 Fault

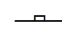
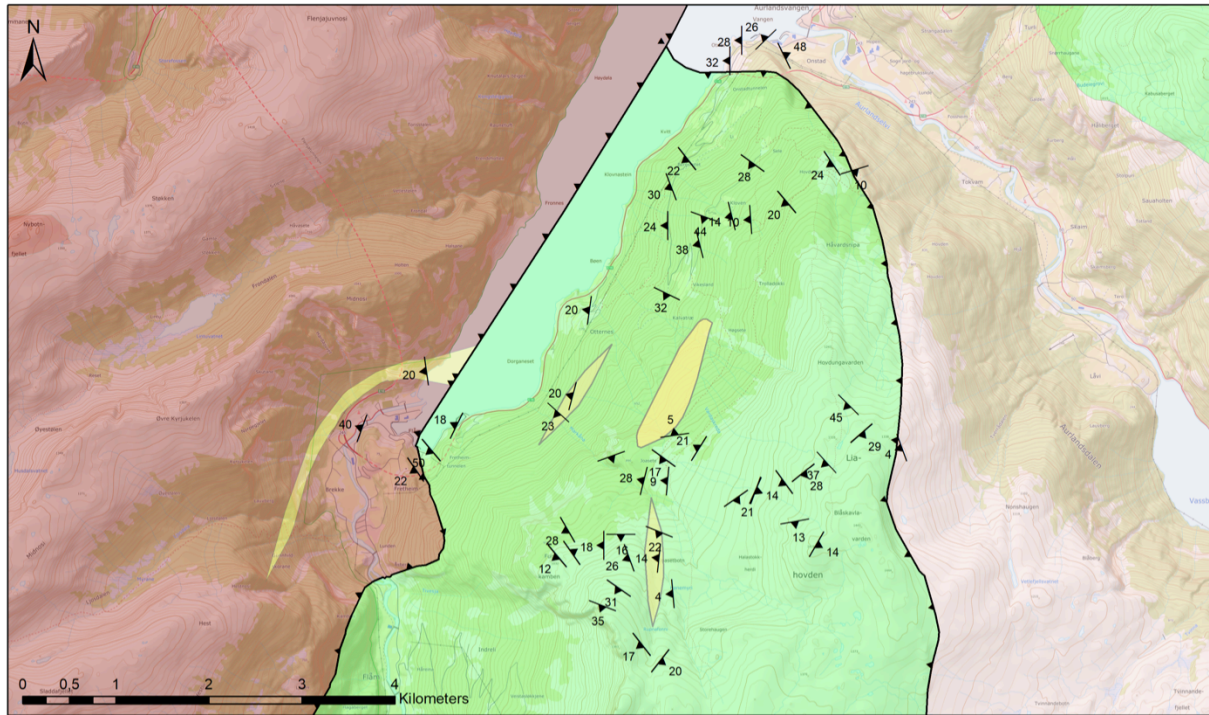
 Joint set

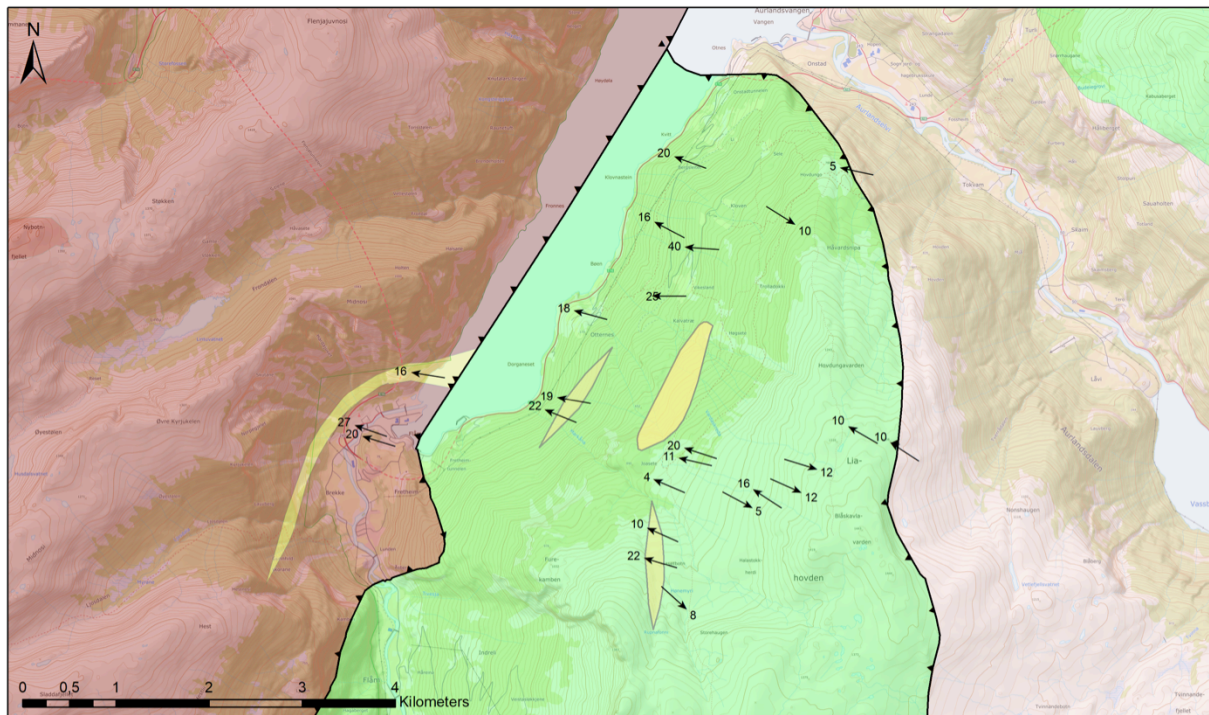
Table 10 – Overview of structural maps presented in the appendix.

No.	Structural map
1	Foliation
2	Stretching lineations
3	Fold axes
4	Axial planes
5	Shear bands
6	Faults and joint sets

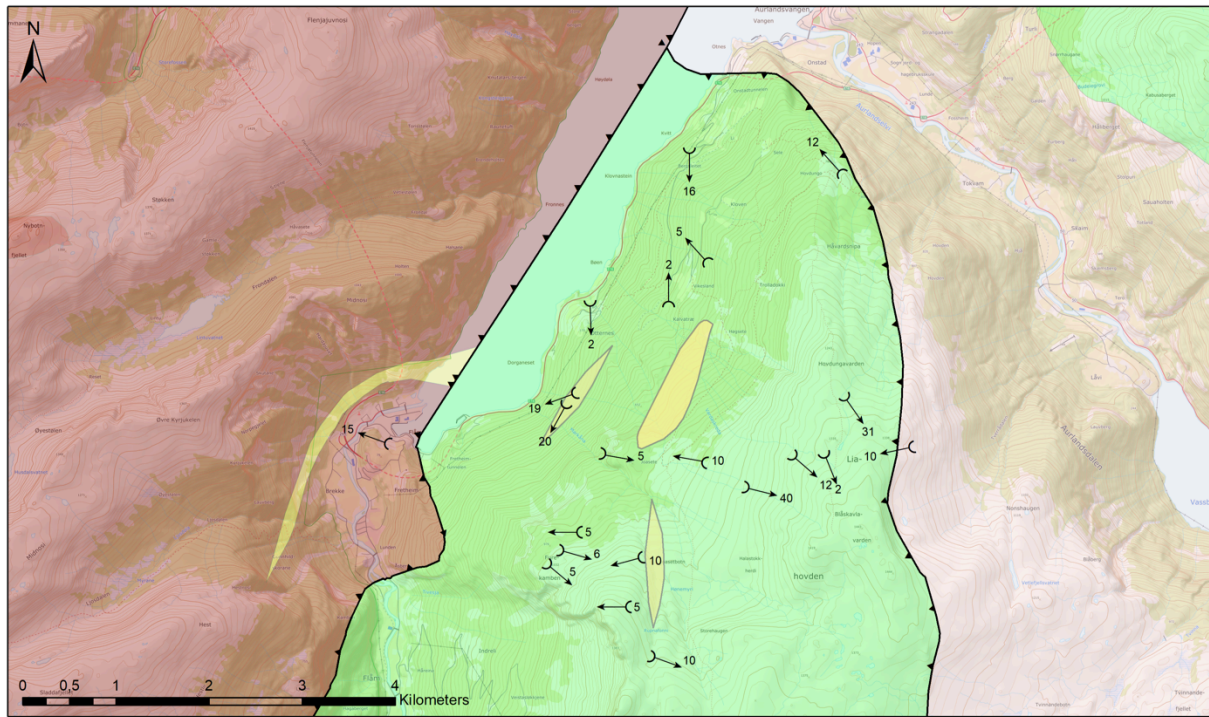
Map 1 – Foliation



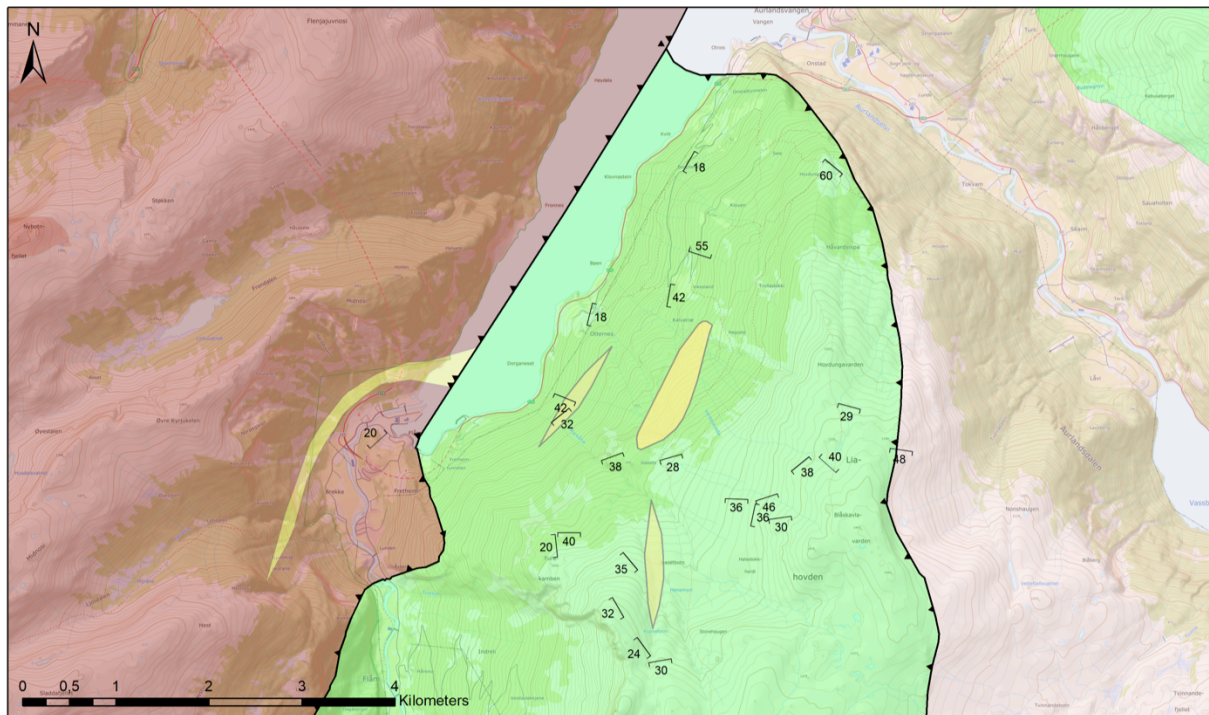
Map 2 – Stretching lineations



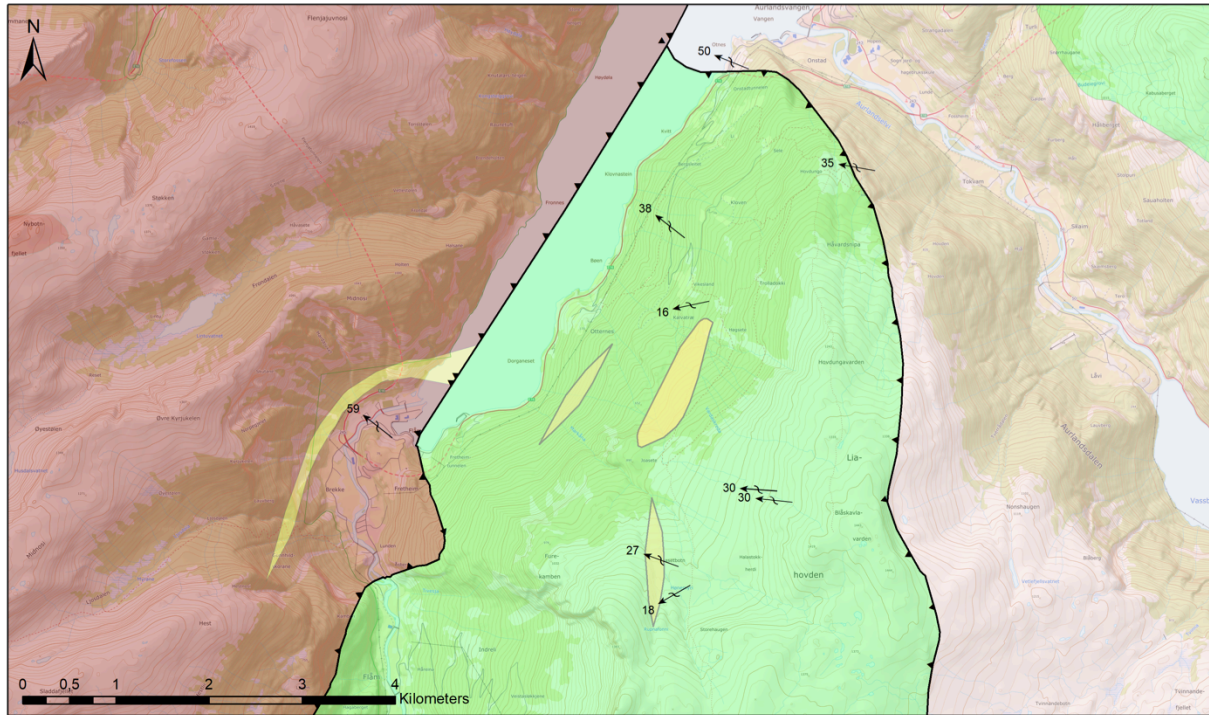
Map 3 – Fold axes



Map 4 – Axial planes



Map 5 – Shear bands



Map 6 – Faults and joint sets

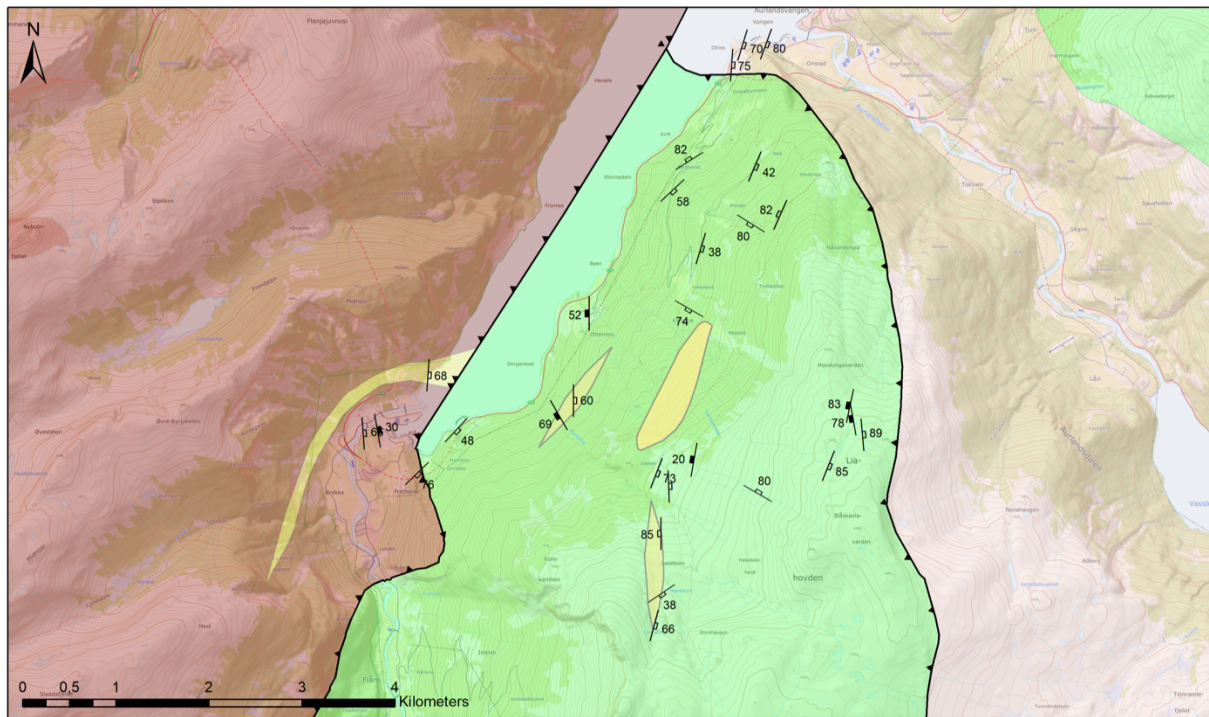


TABLE 11 - STRUCTURAL MEASUREMENTS - (1) TONJE KARIN RIO (2) HELGE HENRIKSEN

(1) FOLIATION				(2) FOLIATION							
Latitude	Longitude	Dip azimuth	Dip	Latitude	Longitude	Dip azimuth	Dip				
60,865653	7,14685396	222	23	60,861542	7,19277799	234	8	60,892423	7,19907104	163	10
60,867273	7,14904298	285	20	60,862936	7,19606898	141	28	60,892553	7,19470700	236	24
60,867358	7,14744204	172	41	60,863780	7,19505301	144	15	60,892553	7,19470700	42	54
60,862808	7,17423404	325	22	60,861905	7,19235001	182	2	60,888361	7,18671201	230	20
60,863666	7,17506602	302	21	60,861905	7,19235001	193	10	60,887264	7,18537199	168	50
60,859659	7,18348003	145	21	60,861281	7,16707204	321	13	60,886203	7,17991102	120	5
60,860613	7,18690203	110	14	60,861281	7,16707204	293	20	60,886203	7,17991102	266	10
60,860613	7,18690203	114	20	60,860217	7,16969901	275	9	60,886237	7,17830999	188	30
60,860577	7,18729304	170	8	60,860217	7,16969901	270	15	60,886316	7,17613497	256	14
60,860483	7,18728902	182	6	60,863842	7,19917003	101	10	60,887750	7,17323701	196	17
60,860467	7,18804599	221	24	60,863955	7,20049404	228	37	60,887750	7,17323701	200	10
60,860148	7,18923898	208	24	60,863955	7,20049404	240	86	60,886120	7,17087801	200	44
60,859736	7,19061898	284	16	60,863955	7,20049404	181	24	60,862218	7,11117103	273	20
60,858839	7,19192899	242	4	60,867357	7,20648902	139	29	60,862031	7,10985901	322	30
60,858335	7,19242402	210	22	60,866172	7,21498098	250	4	60,861721	7,10851497	290	40
60,858057	7,19563999	170	13	60,866221	7,21455996	255	28	60,861084	7,11184200	348	40
60,856801	7,19854399	166	12	60,869779	7,20343298	225	45	60,863090	7,12687704	296	18
60,856190	7,20022297	120	14	60,883301	7,17049303	256	38	60,863090	7,12687704	312	14
60,849534	7,17342602	265	4	60,883301	7,17049303	259	37	60,860576	7,12291701	230	50
60,849534	7,17342602	194	20	60,878332	7,16524101	330	5	60,858514	7,12018702	236	22
60,844445	7,16873500	232	17	60,878332	7,16524101	206	32	60,858624	7,11866504	194	16
60,845961	7,17085797	36	20	60,884675	7,16379798	246	21	60,902438	7,18217497	64	48
60,845961	7,17085797	312	18	60,884675	7,16379798	270	24	60,903576	7,17840504	316	26
60,849427	7,17080198	288	36	60,888476	7,16361903	249	30	60,903200	7,17393296	270	28
60,849923	7,17092796	322	22	60,891386	7,16615899	232	22	60,903200	7,17393296	260	40
60,849923	7,17092796	312	10	60,901117	7,17210202	270	32	60,902613	7,17484198	278	38
60,852716	7,16989900	276	14	60,901117	7,17210202	280	24	60,902613	7,17484198	272	30
60,855477	7,16953699	202	22	60,875627	7,15027504	278	20	60,902327	7,17296996	285	38
60,858312	7,18694502	274	82	60,868017	7,11985904	262	20	60,902327	7,17296996	266	34
60,858312	7,18694502	92	23	60,891737	7,17910904	216	28				
				60,892423	7,19907104	208	14				

STRETCHING LINEATIONS				CRENULATIONS				AXIAL PLANES			
Latitude	Longitude	Trend	Plunge	Latitude	Longitude	Trend	Plunge	Latitude	Longitude	Dip azimuth	Dip
60,865653	7,14685396	292	22	60,860613	7,18690203	104	40	60,863955	7,20049404	140	2
60,867273	7,14904298	280	19	60,860148	7,18923898	181	18	60,863955	7,20049404	158	2
60,862808	7,17423404	283	11	60,858312	7,18694502	194	2	60,866221	7,21455996	258	10
60,863666	7,17506602	288	20	60,883301	7,17049303	310	15	60,869779	7,20343298	145	31
60,859659	7,18348003	118	5	60,882558	7,17036897	318	5	60,883301	7,17049303	311	10
60,860148	7,18923898	303	16	60,875627	7,15027504	196	14	60,882558	7,17036897	310	12
60,849534	7,17342602	132	8					60,882558	7,17036897	305	12
60,852716	7,16989900	287	22	FOLD AXES				60,878332	7,16524101	360	2
60,855477	7,16953699	294	10	Latitude	Longitude	Trend	Plunge	60,878332	7,16524101	180	16
60,861542	7,19277799	114	12	60,865653	7,14685396	209	20	60,875627	7,15027504	196	14
60,863780	7,19505301	107	12	60,867358	7,14744204	250	19	60,875627	7,15027504	178	2
60,860217	7,16969901	289	4	60,859659	7,18348003	110	4	60,892553	7,19470700	318	12
60,860217	7,16969901	293	4	60,859659	7,18348003	271	20	60,861084	7,11184200	290	15
60,863842	7,19917003	111	10	60,859659	7,18348003	128	30				
60,863955	7,20049404	264	12	60,859659	7,18348003	252	12	AXIAL PLANES			
60,867357	7,20648902	300	10	60,860613	7,18690203	165	15	Latitude	Longitude	Dip azimuth	Dip
60,866172	7,21498098	303	10	60,860613	7,18690203	212	24	60,865653	7,14685396	141	32
60,866221	7,21455996	310	4	60,860613	7,18690203	220	13	60,867358	7,14744204	202	42
60,883301	7,17049303	274	40	60,860148	7,18923898	216	10	60,859659	7,18348003	185	45
60,878332	7,16524101	270	25	60,860148	7,18923898	232	10	60,859659	7,18348003	182	36
60,884675	7,16379798	298	16	60,860148	7,18923898	312	21	60,859659	7,18348003	179	30
60,891386	7,16615899	290	20	60,858335	7,19242402	85	30	60,860613	7,18690203	146	25
60,875627	7,15027504	285	18	60,858335	7,19242402	120	20	60,860148	7,18923898	162	46
60,868017	7,11985904	279	16	60,844445	7,16873500	290	2	60,858335	7,19242402	172	30
60,892423	7,19907104	282	5	60,858312	7,18694502	190	3	60,858335	7,19242402	125	22
60,887264	7,18537199	122	10	60,858312	7,18694502	21	8	60,844445	7,16873500	234	24
60,862031	7,10985901	289	27	60,858312	7,18694502	187	10	60,858312	7,18694502	100	42
60,861084	7,11184200	287	20	60,863780	7,19505301	131	12	60,858312	7,18694502	102	36
				60,863955	7,20049404	171	8	60,863780	7,19505301	141	38
								60,863955	7,20049404	172	6

TABLE 11 - STRUCTURAL MEASUREMENTS - (1) TONJE KARIN RIO (2) HELGE HENRIKSEN

				FAULTS							
Latitude	Longitude	Dip azimuth	Dip	Latitude	Longitude	Dip azimuth	Dip	Latitude	Longitude	Dip azimuth	Dip
60,863955	7,20049404	42	40					60,860217	7,16969901	88	75
60,863955	7,20049404	70	43					60,860217	7,16969901	278	88
60,866221	7,21455996	188	48	60,865653	7,14685396	240	69	60,877346	7,16977000	210	74
60,869779	7,20343298	195	29	60,862808	7,17423404	280	20	60,863955	7,20049404	112	85
60,883301	7,17049303	27	24	60,868599	7,20452699	260	78	60,867357	7,20648902	85	89
60,882558	7,17036897	18	55	60,869779	7,20343298	282	83	60,883301	7,17049303	350	80
60,882558	7,17036897	20	35	60,875627	7,15027504	270	52	60,883301	7,17049303	87	30
60,878332	7,16524101	86	45	60,875627	7,15027504	315	55	60,883301	7,17049303	105	25
60,878332	7,16524101	100	42	60,875627	7,15027504	340	44	60,883301	7,17049303	107	38
60,891386	7,16615899	120	18	60,862218	7,11117103	80	30	60,888476	7,16361903	137	58
60,875627	7,15027504	104	18	SURFICIAL LINEATIONS				60,888476	7,16361903	120	60
60,875627	7,15027504	206	10	Latitude	Longitude	Trend	Plunge	60,891386	7,16615899	328	82
60,892553	7,19470700	220	60	60,868599	7,20452699	241	76	60,891386	7,16615899	334	86
60,861084	7,11184200	318	20	60,875627	7,15027504	350	18	60,901117	7,17210202	94	75
SHEAR BANDS				60,875627	7,15027504	348	35	60,901117	7,17210202	102	76
Latitude	Longitude	Dip azimuth	Dip	60,875627	7,15027504	338	40	60,868017	7,11985904	94	68
60,860613	7,18690203	142	34	JOINT SETS				60,868017	7,11985904	102	78
60,860613	7,18690203	130	35	Latitude	Longitude	Dip azimuth	Dip	60,891737	7,17910904	113	42
60,860577	7,18729304	222	29	60,867273	7,14904298	90	60	60,887264	7,18537199	294	82
60,860577	7,18729304	274	30	60,862808	7,17423404	120	68	60,886203	7,17991102	206	89
60,859736	7,19061898	276	30	60,860483	7,18728902	26	90	60,886203	7,17991102	212	80
60,849534	7,17342602	240	18	60,860483	7,18728902	30	80	60,886316	7,17613497	192	88
60,849534	7,17342602	248	40	60,845961	7,17085797	117	68	60,862218	7,11117103	110	80
60,852716	7,16989900	290	27	60,845961	7,17085797	120	62	60,862218	7,11117103	130	86
60,877346	7,16977000	258	16	60,846738	7,17020301	108	68	60,862218	7,11117103	143	82
60,884675	7,16379798	308	38	60,846738	7,17020301	105	66	60,862031	7,10985901	114	85
60,884675	7,16379798	298	28	60,849923	7,17092796	146	38	60,862031	7,10985901	132	67
60,901117	7,17210202	292	50	60,849923	7,17092796	144	32	60,861721	7,10851497	86	66
60,892423	7,19907104	280	35	60,855477	7,16953699	270	85	60,863090	7,12687704	133	48
60,892423	7,19907104	286	43	60,861281	7,16707204	111	73	60,863090	7,12687704	108	50
60,862218	7,11117103	308	59	60,861281	7,16707204	117	75	60,858514	7,12018702	136	76
60,903576	7,17840504	110	80	400171	6748793	202	56	399968	6747858	190	22
60,903200	7,17393296	107	70	400346	6748868	211	15	399835	6747791	310	5
60,903200	7,17393296	112	76	400526	6748864	216	17	399564	6747717	190	22
60,902613	7,17484198	110	78	400526	6748864	273	14	399564	6747717	206	12
60,902613	7,17484198	112	70	400578	6748901	175	40	399457	6747561	120	15
60,902327	7,17296996	110	56	400578	6748901	174	40	399457	6747561	130	18
60,902327	7,17296996	98	52	400835	6748885	203	15	399492	6747706	230	12
60,902327	7,17296996	200	70	400835	6748885	266	15	399447	6747844	33	4
60,902327	7,17296996	174	84	400750	6749089	310	8	399571	6747997	240	28
(2) FOLIATION				400750	6749089	315	25	399600	6747767	55	23
UTM EW	UTM NS	Dip azimuth	Dip	400750	6749089	355	20	400298	6745360	172	30
400464	6748801	266	18	400686	6749077	330	25	400667	6746716	128	20
400464	6748801	300	27	400656	6749077	345	14	400721	6747398	190	22
400464	6748801	252	20	400609	6749057	260	22	400591	6748604	290	28
400464	6748801	290	14	400609	6749057	308	19	400591	6748604	190	35
400464	6748801	286	12	399950	6748851	148	52	400450	6748800	260	30
400464	6748801	240	25	399950	6748851	160	42	400450	6748800	298	22
400454	6748653	257	21	399950	6748851	170	21	400615	6749189	110	10
400454	6748653	268	16	400017	6747235	201	35	400585	6749108	352	5
400422	6748606	268	35	400168	6747244	251	35	FOLD AXES			
400422	6748606	271	31	400168	6747244	260	37	UTM EW	UTM NS	Trend	Plunge
400422	6748606	232	49	400179	6747429	215	31	400464	6748801	230	15
400366	6748548	295	38	400179	6747429	190	5	400464	6748801	228	19
400366	6748548	274	32	400161	6747549	240	15	400578	6748901	100	3
400366	6748548	260	42	400140	6747765	235	10	400835	6748885	280	10
400346	6748514	277	26	400140	6747765	246	20	399950	6748851	100	5
400324	6748585	284	28	400140	6747765	220	28	400168	6747244	270	5
400262	6748713	200	20	400257	6747754	230	25	400257	6747754	255	10
400262	6748713	195	32	400257	6747754	250	26	399457	6747561	130	5
400262	6748713	230	16	400257	6747754	261	32	399447	6747844	296	2

TABLE 11 - STRUCTURAL MEASUREMENTS - (1) TONJE KARIN RIO (2) HELGE HENRIKSEN

399571	6747997	270	5	400464	6748801	224	79	400346	6748514	147	80	
399600	6747767	106	6	400464	6748801	214	88	400346	6748514	220	80	
399600	6747767	100	8	400464	6748801	92	82	400346	6748514	30	72	
400667	6746716	110	10	400464	6748801	147	64	400324	6748585	110	54	
AXIAL PLANES				400464	6748801	77	79	400324	6748585	125	70	
UTM EW	UTM NS	Dip	azimuth	Dip	400454	6748653	87	68	400324	6748585	13	80
400464	6748801	224	35	400454	6748653	205	37	400288	6748711	275	82	
400464	6748801	207	20	400454	6748653	207	80	400262	6748713	285	87	
400526	6748864	145	40	400454	6748653	100	65	400262	6748713	244	62	
400526	6748864	166	32	400454	6748653	100	65	400262	6748713	60	56	
400578	6748901	164	28	400422	6748606	96	35	400262	6748713	63	72	
400578	6748901	180	45	400422	6748606	354	69	400262	6748713	147	79	
400578	6748901	210	25	400422	6748606	89	40	400262	6748713	104	90	
399950	6748851	160	38	400422	6748606	98	70	400171	6748793	134	90	
400168	6747244	240	32	400422	6748606	155	20	400171	6748793	308	178	
400257	6747754	230	35	400366	6748548	106	165	400346	6748868	98	80	
399447	6747844	264	20	400366	6748548	148	58	400526	6748864	264	85	
399571	6747997	180	40	400366	6748548	150	70	400526	6748864	180	77	
399571	6747997	175	22	400366	6748548	46	77	400578	6748901	24	84	
400667	6746716	170	30	400366	6748548	106	68	400578	6748901	74	76	
JOINT SETS				400366	6748548	189	63	400578	6748901	78	75	
UTM EW	UTM NS	Dip	azimuth	Dip	400366	6748548	210	87	400578	6748901	259	81
400464	6748801	80	85	400366	6748548	142	65	400835	6748885	115	50	
400464	6748801	10	49	400366	6748548	200	40	400835	6748885	200	66	
400464	6748801	17	80	400366	6748548	156	86	400835	6748885	229	65	
400464	6748801	89	79	400366	6748548	200	40	400835	6748885	200	70	
400464	6748801	31	90	400366	6748548	108	68	400835	6748885	127	67	
400464	6748801	16	87	400366	6748548	78	80	400835	6748885	201	85	
400464	6748801	207	83	400366	6748548	163	85	400835	6748885	114	88	
400464	6748801	80	74	400366	6748548	106	62	400835	6748885	120	72	
400464	6748801	213	72	400346	6748514	151	87	400758	6748989	78	75	
400464	6748801	76	77	400346	6748514	121	65	400750	6749089	192	68	
400750	6749089	119	70	400140	6747765	110	75	399515	6747691	60	80	
400750	6749089	118	28	400140	6747765	114	74	399457	6747561	130	60	
400686	6749077	272	77	400140	6747765	270	90	399457	6747561	295	85	
400686	6749077	190	50	400140	6747765	208	60	399457	6747561	114	75	
400656	6749077	205	82	400140	6747765	60	80	399457	6747561	293	86	
400656	6749077	60	85	400140	6747765	175	65	399457	6747561	30	80	
400656	6749077	92	43	400140	6747765	50	80	399457	6747561	296	81	
400609	6749057	105	68	400257	6747754	80	82	399457	6747561	300	88	
400609	6749057	76	77	400257	6747754	115	62	399492	6747706	60	82	
400609	6749057	28	78	400257	6747754	108	72	399492	6747706	30	90	
400609	6749057	103	61	400257	6747754	138	80	399492	6747706	120	86	
399950	6748851	94	88	400257	6747754	248	82	399492	6747706	30	75	
399950	6748851	120	84	400139	6748017	120	73	399492	6747706	120	80	
399950	6748851	80	78	400139	6748017	232	62	399492	6747706	300	62	
399950	6748851	261	80	400139	6748017	115	71	399492	6747706	300	70	
399950	6748851	110	90	400139	6748017	265	90	399393	6747733	120	75	
399950	6748851	112	70	400139	6748017	180	58	399393	6747733	20	80	
399950	6748851	90	90	399968	6747858	28	78	399393	6747733	80	90	
400017	6747235	70	78	399968	6747858	160	70	399393	6747733	150	55	
400017	6747235	61	75	399968	6747858	128	40	399447	6747844	125	82	
400017	6747235	310	78	399968	6747858	175	60	399447	6747844	60	87	
400017	6747235	70	72	399968	6747858	50	75	399447	6747844	162	52	
400168	6747244	110	79	399968	6747858	200	60	399447	6747844	99	88	
400168	6747244	116	83	399835	6747791	142	65	399571	6747997	110	78	
400168	6747244	55	72	399835	6747791	120	90	399571	6747997	110	80	
400168	6747244	112	88	399835	6747791	125	85	399571	6747997	340	70	
400179	6747429	100	40	399835	6747791	125	76	399571	6747997	50	72	
400179	6747429	106	80	399835	6747791	260	5	399600	6747767	355	65	
400179	6747429	55	72	399564	6747717	310	80	399600	6747767	65	80	
400179	6747429	110	48	399564	6747717	120	90	399600	6747767	40	71	